

ALMA MATER STUDIORUM · UNIVERSITÀ DI BOLOGNA

Scuola di Scienze
Corso di Laurea Magistrale in Fisica della Materia

Quantum Magnetism in Relativistic Osmates from First Principles

Relatore:
Prof. Federico Boscherini

Presentata da:
Dario Fiore Mosca

Correlatore:
Prof. Cesare Franchini

Sessione III
Anno Accademico 2018/2019

Contents

Contents	3
List of Figures	6
List of Tables	7
1 Introduction	10
2 Theory and Methods	12
2.1 Magnetism as a quantum effect	12
2.2 Magnetism in Transition Metal Oxides	14
2.2.1 Coulomb exchange	15
2.2.2 Simple model for direct exchange	16
2.2.3 Superexchange	18
2.2.4 Hubbard Model	21
2.2.5 Crystal Field	23
2.2.6 Spin-Orbit Coupling	24
2.2.7 Jahn-Teller effect	28
2.3 Density Functional Theory	29
2.3.1 Hohenberg-Kohn theorems	30
2.3.2 Kohn-Sham equations	32
2.3.3 Functionals for Exchange and Correlation	36
2.3.4 The Mott Insulator problem (DFT + U)	37
2.3.5 Spin Density Functional Theory	38
2.4 Practical implementations of DFT	41
2.4.1 Plane Waves	41
2.4.2 The projector augmented-wave method (PAW)	41
2.4.3 Sampling the Brillouin Zone	44
2.4.4 Collinear vs Non Collinear systems	45

3	Double perovskites $\text{Ba}_2\text{NaOsO}_6$ and $\text{Ba}_2\text{CaOsO}_6$	47
3.1	Physical properties of BNOO	48
3.1.1	Magnetic properties	49
3.1.2	Local symmetry breaking and canted ferromagnetism	51
3.2	Physical properties of BCOO	55
3.2.1	Magnetic properties	56
4	Results	58
4.1	Distortions in BNOO	59
4.2	Bandstructure, DOS and effective U for BNOO	62
4.3	Magnetic ground state of BNOO	66
4.4	Origin of canted magnetism	71
4.5	Preliminary results on BCOO	82
4.6	Frustration without ionic relaxation	85
4.7	Frustration with ionic relaxation	85
4.8	Electronic Bandstructure	88
4.9	Canting angles in BCOO	91
5	Conclusions	93
A	VASP files	96
A.1	Bondlength Relaxation	96
A.2	Energy curve as a function of the canting angle	99
B	Spin	102
B.1	Algebra of Spins	102
B.2	Coupling of two spins	103
C	Additional results for BNOO	104
C.1	Bondlengths and DOS	104
C.2	Phase Diagram	107
D	Other results for BCOO	108
	Bibliography	110

List of Figures

2.1	Magnetic phases for MnO	19
2.2	Exchange paths and Goodenough-Kanamori rules	20
2.3	Energy splitting of d orbitals in an octahedral environment.	24
2.4	Evolution of the d orbitals under CFE and SOC.	25
2.5	Jahn-Teller effect on t_{2g} states.	28
2.6	DFT self consistent cycle	35
2.7	E_{cutoff} and k-mesh test for Ba_2NaOsO_6	43
3.1	Crystallographic structure of BNOO and BCOO	48
3.2	Mean field phase diagram for BNOO in cubic symmetry at T=0	50
3.3	Sketch of the phase diagram of BNOO from NMR measurements	52
3.4	Canting angles between spins in the two sublattice magnetic order of BNOO	53
3.5	Suggested distortions of the Na octahedra in BNOO	54
3.6	Magnetic phase diagrams of BCOO	56
4.1	Energy dependence of BNOO on Na-O c bondlength	60
4.2	Energy dependence of BNOO on θ tilting angle	61
4.3	Dependence of the energy gap from U (BNOO)	63
4.4	Bandstructure of BNOO with LDA and LDA + U.	64
4.5	Bandstructure of BNOO with LDA + U + SOC	65
4.6	Energy as a function of ϕ for BNOO	67
4.7	Energy as a function of ϕ with distortions for BNOO	68
4.8	Energy as a function of θ_c with different U_{eff} for BNOO	70
4.9	New reference frame for the Pseudo Spins	73
4.10	Fit of the energy curve as a function of the canting angle ϕ for U-J = 3.4 eV.	77
4.11	Plot of the asymmetric contributions with respect to $\phi = 45^\circ$	78
4.12	(a) It is the plot of the dependence of the asymmetric fitting terms on U_{eff} , wher A_1 is Ex + OCP, A_3 is OCP and B_2 is OCP. (b) It is the plot of the dependence of the symmetric contributions on U_{eff} . The parameter B_1^* is $B_1 - 6$ meV and is the An + OCP, while A_2 is the QP + OCP.	79

4.13	Fitting curve (Left Figure) and asymmetric contributions (Right Figure) for energy curve as function of the canting angle ϕ with $U-J = 2.4$ eV. . .	80
4.14	Fitting curve (Left Figure) and asymmetric contributions (Right Figure) for energy curve as function of the canting angle ϕ with $U-J = 3.2$ eV. . .	81
4.15	Some of the magnetic phases probed via ab initio calculations for BCOO	84
4.16	Local distortions for the AFM 110 in plane magnetic configuration of BCOO	86
4.17	Bandstructure of BCOO with LDA and LDA + U.	89
4.18	Bandstructure of BCOO with LDA + U + SOC.	90
4.19	Energy as a function of ϕ with different U_{eff} for BCOO	92
C.1	Bondlengths dependence for BNOO	105
C.2	DOS of BNOO with LDA	105
C.3	DOS of BNOO with LDA + U and LDA + U +SOC	106
C.4	Phase diagram of BNOO	107
D.1	DOS of BCOO with LDA	108
D.2	DOS of BCOO with LDA + U and LDA + U +SOC	109

List of Tables

3.1	Crystallographic positions of atoms in BNOO as obtained via X-ray powder diffraction at room temperature [76].	48
3.2	Crystallographic positions of atoms in BCOO as obtained via X-ray powder diffraction at 280 K, together with the refinements obtained from neutrons only at 3.5 K, reported in square brackets [84].	55
4.1	Bondlengths distortions of BNOO 2	60
4.2	Bondlengths distortions of BNOO 2	61
4.3	Energy of FM 110 and AFM 110 configurations for BNOO	66
4.4	Magnetization and Os magnetic moment in BNOO with $U_{eff} = 3.0$ eV	68
4.5	Magnetization of BNOO with $U = 3.0$ eV	69
4.6	Energy difference between minima for different U_{eff}	71
4.7	Multipolar tensor operators for a cubic magnetic environment.	74
4.8	Values of the fitting parameters for BNOO.	77
4.9	Energy for different magnetic configurations for BCOO without ionic relaxation	85
4.10	Relative displacements of the Ca-O bondlengths in BCOO for different magnetic configurations	87
4.11	Energy for different magnetic configurations for BCOO with ionic relaxation	87

Abstract

The interplay between electron correlation, local distortions and Spin Orbit Coupling is one of the most attractive phenomena in condensed matter Physics and have stimulated much attention in the last decade. In Osmates double perovskites the coupling between electronic, structural and orbital degrees of freedom leads to the formation of an unconventional magnetic phase, whose precise origin and characteristics are still not understood. In particular strong Spin Orbit Coupling effect is believed to occur and have a crucial role in enhancing multipolar exchange interactions in a fashion similar to the more studied 4f electron systems. In this thesis, by means of first principles calculations, we study the structural, electronic and magnetic proprieties of the Mott insulating $\text{Ba}_2\text{NaOsO}_6$ with Osmium in $5d^1$ electron configuration within the fully relativistic Density Functional Theory plus on site Hubbard U (DFT + U) scheme. We find that the system is subjected to local symmetry breaking and that the magnetic ground state is strongly dependent on the on site Coulomb interaction. Furthermore, by mapping the energy onto a Pseudospin Hamiltonian, we are capable to prove that quadrupolar and octupolar exchanges play a significant role. We repeated the study for $\text{Ba}_2\text{CaOsO}_6$ with Os in $5d^2$ electronic configuration as a preliminary step for understanding if phase transitions are possible when $\text{Ba}_2\text{NaOsO}_6$ is doped.

Abstract (Italiano)

Nelle doppie perovskiti contenenti Osmio, come e' il caso del $\text{Ba}_2\text{NaOsO}_6$, e' previsto esserci una forte competizione tra effetti diversi quali correlazione elettronica, distorsioni che portano a ridotte simmetrie locali e forte interazione di Spin Orbita. Gli effetti che questi hanno sulle proprieta' elettroniche e magnetiche non sono ancora comprese a fondo e c'e' grande interesse al riguardo per via delle proprieta' magnetiche osservate sperimentalmente che sono assolutamente non convenzionali. In particolare, lo Spin Orbit Coupling si prevede abbia un ruolo cruciale nello stabilizzare una data configurazione magnetica attraverso interazioni di scambio che non sono solo di dipolo, ma anche di ordini maggiori quali quadrupolari o ottupolari, come gia' osservato nei piu' studiati sistemi con elettroni 4f. Il lavoro svolto e' stato finalizzato a comprendere le proprieta' strutturali, elettroniche e magnetiche di questo materiale ed e' stato fatto attraverso i metodi a primi principi con inclusione di effetti relativistici nel contesto della Density Functional Theory. Quello che abbiamo trovato e' che una distorsione locale degli ottaedri e' effettivamente presente e che lo stato magnetico e' fortemente dipendente dalla interazione Coulombiana "on site". Inoltre siamo riusciti a mappare la curva di energia in una Hamiltoniana di Pseudospin, la quale ci ha permesso di dimostrare che le interazioni di quadrupolo e ottupolo sono significative ai fini della stabilizzazione del dato ordine magnetico. Lo studio e' stato poi ripetuto nel caso del $\text{Ba}_2\text{CaOsO}_6$, dove l'Osmio ha configurazione elettronica $5d^2$. Questo e' servito come step preliminare per comprendere la natura di una possibile transizione di fase tra i due materiali qualora si intervenga su di essi attraverso il doping.

Chapter 1

Introduction

Transition Metal Oxides (TMOs) have been intensively studied because of their rich spectrum of structural, electronic and magnetic properties. One can think, for example, at the colossal magnetoresistance found in Manganites [72], or the high-temperature superconductors observed in Cuprates [15, 70]. Recently, interest is grown on 4d and 5d transition metal series, in which novel magnetic phases has been observed driven by the Spin Orbit Coupling (SOC) effect together with strong electron correlation [58, 73]. In particular Iridates have been the subject of many theoretical and experimental studies and it has been proved that SOC is indispensable for the appearance of a canted magnetic order and the formation of a Dirac-Mott gap (i.e. spin-orbit coupled mott insulating state)[9, 16, 59]. But the interest in relativistic oxides is not limited to Iridates. Osmates double perovskites constitute a breeding ground for the investigation of the interplay between electron correlation, local distortions and SOC effects. The last effect, in particular, is believed to be much stronger than in 3d or 4d TMOs, leading to new phases and magnetic orders driven by exchange interactions of higher order than bipolar, in a fashion similar to the more studied 4f electron systems. When it comes to describe a material with SOC effect two approaches are used depending on the strenght of the coupling. In the weak limit the interaction is included as a small perturbation in the total Hamiltonian, leading to a Spin Hamiltonian approach with correcting terms that take into account the anisotropy of the exchange interactions in presence of SOC. In the strong SOC limit the contribution cannot be considered as a perturbation as well as the spin momentum is no more a good quantum number. As a consequence the spin operator must be replaced by a total angular momentum operator and the exchange interactions can be strongly anisotropic, leading to higher order interactions that cannot be described within the Spin Hamiltonian approach and a Pseudo Spin Hamiltonian one is required. The Pseudospin is the semiclassical version of the total angular momentum operator and allows for a model Hamiltonian description of multipolar interactions in strong SOC systems, as is the case of UO_2 [68].

The possible effects of the strong SOC regime are also related to the structure of the

crystal. In fact, since the spin can interact with the lattice, the spin lattice interaction is affected by the lattice symmetry and this can break the symmetry of the lattice, as is the case of Sr_2IrO_4 [55]. The interest in the Mott insulator $\text{Ba}_2\text{NaOsO}_6$ can be easily understood by looking at previous studies. They proved that it is a Dirac-Mott insulator with a gap that can be opened only if both on site Coulomb interaction and SOC are considered. Furthermore it is a ferromagnet with low magnetic moment along the [110] axis even though Landau theory predicts that such ferromagnetic state is not allowed in a collinear spin systems. Finally no structural transition has been observed, but recent NMR studies has proven the appearance of a local symmetry breaking immediately before the magnetic phase transition.

But if $\text{Ba}_2\text{NaOsO}_6$ was already studied experimentally and theoretically, even if without the inclusion of non collinear spins and multipolar interactions, very few experiments has been done on $\text{Ba}_2\text{CaOsO}_6$ and theoretical predictions range over a large number of possible magnetic ground states. The interest with respect to this material is not limited to its magnetic phase, but, as in $\text{Ba}_2\text{NaOsO}_6$ also to the electronic and structural properties. In particular, the fact that the Os electronic configuration changes from d^1 to d^2 suggests possible phase transitions in passing from the first to the latter through doping.

This work is focused on the investigation of the properties outlined above through ab initio calculations made with the Vienna Ab initio Simulation Package (VASP).

The structure of the thesis is the following: Chapter one is divided into three main sections which are focused on the Theory and the Methods used. More specifically the first section is about magnetism as a quantum effect and the theoretical models that can describe it when dealing with TMOs. Particular attention to the many body problem of interacting electrons will be made as well. The second section faces the many body problem from another perspective. In this section the Density Functional Theory is introduced, with its theorems and implementations to specific cases like magnetic materials and relativistic materials. Finally the third section concerns the practical implementations of DFT on a computational level and the main aspects of an ab initio code with attention on some VASP tools especially when these are related to magnetism.

The second Chapter introduces the main properties, at the state of the art, of the two materials investigated, in Chapter 3 the practical methods used as well as the results obtained are presented. The theoretical models used for describing the physical properties will be presented in a way that allows to understand their necessity by underlying their strenghts and weaknesses.

Finally in Chapter 4 there is a summary of the results with further comments.

Chapter 2

Theory and Methods

2.1 Magnetism as a quantum effect

Magnetism in condensed matter is inherently a quantum mechanical effect.

In classical physics, magnetic moments are originated by electric current densities $\mathbf{j}(\mathbf{r})$ via

$$\boldsymbol{\mu} = \frac{1}{2} \int \mathbf{r} \times \mathbf{j} \, d\mathbf{r} \quad (2.1)$$

and they interact with each other through the dipole-dipole coupling

$$E = -\frac{\mu_0}{4\pi|\mathbf{r}|^3} \left(3(\boldsymbol{\mu}_1 \cdot \hat{\mathbf{r}})(\boldsymbol{\mu}_2 \cdot \hat{\mathbf{r}}) - \boldsymbol{\mu}_1 \cdot \boldsymbol{\mu}_2 \right) \quad (2.2)$$

where \mathbf{r} is the vector that connects the two dipoles.

This interaction is however not capable of describing the magnetic properties of materials, in fact, as an example, it is sufficient to take into account magnetite that is ferromagnetic at temperatures lower than 860 K. If one considers that the atomic magnetic moments have an intensity that is of the order of $\sim 1\mu_B$, two such moments at a distance of 1 Å will have a magnetostatic energy $E \sim 0.05$ meV, that corresponds to a temperature of less than 1 K.

Moreover, in classical mechanics, the contribution of electric and magnetic fields to the motion of a particle of charge q is given in the Hamiltonian by the substitution $\mathbf{p} \rightarrow \mathbf{p} + q\mathbf{A}$, where \mathbf{A} is the vector potential. This implies only a shift of the momentum into the classical partition function F , which can be easily reabsorbed, leaving F unchanged and leading to no net magnetization

$$M = - \left(\frac{\partial F}{\partial B} \right)_{T,V} . \quad (2.3)$$

The assertion that in a classical systems no net magnetization can appear at thermal equilibrium is known as the *Bohr-van Leuween theorem* [2].

It is necessary to jump into the quantum mechanical world to understand the truly physical origin of magnetism and, since we are interested in describing magnetism in condensed matter, the starting point is the non relativistic Hamiltonian for electrons

$$\mathcal{H} = \sum_{i=1}^N \frac{\mathbf{p}_i^2}{2m_e} + \sum_{i=1}^N V(\mathbf{r}_i) + \sum_{i>j}^N U(\mathbf{r}_i, \mathbf{r}_j) , \quad (2.4)$$

where the terms on the right side are in order: *kinetic energy*, *external potential*, *electron-electron interaction* and N is the number of electrons i.e. $N = ZN_{ions}$ where Z is the atomic number and N_{ions} is the number of ions.

Equation 2.4 is written already, implicitly, within the assumption that the kinetic energy term of the bare ions and the repulsive Coulombic interaction between them can be neglected, allowing us to write only the electronic terms. This approximation is known as the *Born Oppenheimer Approximation* [14].

The external potential is nothing but the Coulomb potential between ions and electrons:

$$V(\mathbf{r}_i) = \sum_{\alpha=1}^{N_{ion}} \frac{Ze^2}{|\mathbf{R}_\alpha - \mathbf{r}_i|} \quad (2.5)$$

and the electron-electron interaction

$$U(\mathbf{r}_i, \mathbf{r}_j) = \frac{e^2}{|\mathbf{r}_i - \mathbf{r}_j|} \quad (2.6)$$

The not so surprising result is that, even at such a simple level, no closed form solution to this many-body problem can be found explicitly and alternative approaches are needed. In particular, from equation 2.4 magnetism is not explicitly evident.

These topics will be discussed in the following sections, starting from simple atomic models and continuing with the Hubbard Model for describing magnetic interactions and magnetic properties of materials. The many body problem will be then treated within a different theoretical approach known as Density Functional Theory, with some focus on the computational and application methods for describing to magnetism.

2.2 Magnetism in Transition Metal Oxides

Transition Metal Oxides (TMOs) comprise a large class of materials with very diverse physical properties which provide a breeding ground for the investigation and the study of several interesting phenomena. The extent of this field can be understood easily by looking at the already known properties of some compounds. For example one can look at the electronic properties, and would find insulators (CoO, NiO, BaTiO₃), semiconductors, metals (CrO₂, ReO₃) and superconductors (YBa₂Cu₃O₇) [42]. Or one could be interested in the magnetic properties, and would encounter ferromagnetic (CrO₂), anti-ferromagnetic (CoO, NiO), ferrimagnetic (Fe₃O₄, Y₃Fe₅O₁₂) and ferro-electric (BaTiO₃) materials. The crystal structure can be also very different, from simple binary monoxides (NiO, CoO) with NaCl structure to ternary oxides (BaTiO₃, SrTiO₃) with perovskite structure or to complicated structures such as Co₃O₄ or Fe₃O₄ with the normal and inverse spinel structure [42]. This diversity allows transition metal oxides to find applications in many fields of technical interest, from nonlinear optics to sensors and catalysis [13, 65]

Although equation 2.4 seems to give no insight about magnetism in solids, all those informations are implicit in three properties apparently unrelated to it: *Pauli Exclusion principle*, *Coulomb exchange* and *kinetic exchange*.

The physical intuition behind these effects is not difficult. Since electrons are Fermions, they obey the Pauli exclusion principle, which does not allow two of them to be in the same quantum state, i.e. electrons with the same spin cannot be at the same position and electrons at the same position cannot have the same spin. As a natural consequence, electrons that have the same spin tend to avoid each other.

The Coulomb interaction is, on its classical viewpoint, an electrostatic interaction between charges that repels those of the same "sign" and attracts those of opposite "sign". The combination of just these two effects already brings to remarkable results. In fact, if electrons have the same spin they will tend to lower the Coulombic energy, leading to spin parallel states as the most favourable ones. When applied to a single atom this result is basically the first Hund's rule [25].

But electrons in materials can also move to neighboring ionic sites or orbitals, leading to a kinetic contribution that influences the electronic spin configuration since only electrons with unpaired spins can occupy the same orbital. This is the last effect known as kinetic exchange which is responsible for *direct exchange*, *superexchange*, *double exchange* and *orbital ordering* [24].

2.2.1 Coulomb exchange

The Coulomb repulsion of equation 2.6 is manifestly spin independent. Nevertheless, the antisymmetrization of the wavefunction leads to spin dependent energy terms.

As a simple model let's consider the two electron Hamiltonian

$$\mathcal{H} = \mathcal{H}_0(\mathbf{r}_1) + \mathcal{H}_0(\mathbf{r}_2) + \frac{e^2}{|\mathbf{r}_1 - \mathbf{r}_2|} \quad (2.7)$$

with the assumption that the electron-electron interaction is smaller than \mathcal{H}_0 , so that the perturbation theory can be applied. The calculation of the matrix elements requires the knowledge of the basis set of wavefunctions for the unperturbed term, which are given by

$$\psi_{\uparrow\uparrow} = \frac{1}{\sqrt{2}} \begin{vmatrix} \phi_a(\mathbf{r}_1)\alpha(\boldsymbol{\sigma}_1) & \phi_a(\mathbf{r}_2)\alpha(\boldsymbol{\sigma}_2) \\ \phi_b(\mathbf{r}_1)\alpha(\boldsymbol{\sigma}_1) & \phi_b(\mathbf{r}_2)\alpha(\boldsymbol{\sigma}_2) \end{vmatrix} \quad (2.8)$$

for electrons with both spins up, and

$$\psi_{\uparrow\downarrow} = \frac{1}{\sqrt{2}} \begin{vmatrix} \phi_a(\mathbf{r}_1)\beta(\boldsymbol{\sigma}_1) & \phi_a(\mathbf{r}_2)\beta(\boldsymbol{\sigma}_2) \\ \phi_b(\mathbf{r}_1)\alpha(\boldsymbol{\sigma}_1) & \phi_b(\mathbf{r}_2)\alpha(\boldsymbol{\sigma}_2) \end{vmatrix} \quad (2.9)$$

for electrons with one spin up and the other down. Where ϕ_a is the eigenvector of \mathcal{H}_0 with eigenvalue E_a , ϕ_b is the eigenvector of \mathcal{H}_0 with eigenvalue E_b . The complete basis is given by the other two possible spin configurations ($\psi_{\downarrow\downarrow}, \psi_{\downarrow\uparrow}$) with both spins down and with one spin down and the other up.

The matrix of the Coulomb term, in the basis of the states $\psi_{\uparrow\uparrow}, \psi_{\downarrow\downarrow}, \psi_{\uparrow\downarrow}, \psi_{\downarrow\uparrow}$ is

$$H = \begin{pmatrix} E_{ab} + K_{ab} - J_{ab} & 0 & 0 & 0 \\ 0 & E_{ab} + K_{ab} & -J_{ab} & 0 \\ 0 & -J_{ab} & E_{ab} + K_{ab} & 0 \\ 0 & 0 & 0 & E_{ab} + K_{ab} - J_{ab} \end{pmatrix} \quad (2.10)$$

where $E_{ab} = E_a + E_b$,

$$K_{ab} = \int \int d\mathbf{r}_1 d\mathbf{r}_2 \frac{e^2}{|\mathbf{r}_1 - \mathbf{r}_2|} |\phi_a(\mathbf{r}_1)|^2 |\phi_b(\mathbf{r}_2)|^2 \quad (2.11)$$

is the *Coulomb integral* and

$$J_{ab} = \int \int d\mathbf{r}_1 d\mathbf{r}_2 \phi_a^*(\mathbf{r}_1) \phi_b^*(\mathbf{r}_2) \frac{e^2}{|\mathbf{r}_1 - \mathbf{r}_2|} \phi_b(\mathbf{r}_1) \phi_a(\mathbf{r}_2) \quad (2.12)$$

is the *exchange integral*.

The diagonalization of this matrix gives a singlet state $(\psi_{\uparrow\downarrow} - \psi_{\downarrow\uparrow})/\sqrt{2}$ with energy

$$E_s = E_{ab} + K_{ab} + J_{ab} \quad (2.13)$$

and a triplet $\psi_{\uparrow,\uparrow}, \psi_{\downarrow,\downarrow}, (\psi_{\uparrow\downarrow} + \psi_{\downarrow\uparrow})/\sqrt{2}$ with energy

$$E_t = E_{ab} + K_{ab} - J_{ab} \quad (2.14)$$

It can be demonstrated that $J_{ab} > 0$, giving the configuration with parallel spins as the most favorable one. If ϕ_a and ϕ_b are degenerate atomic orbitals, this is an example of the Hund's first rule.

An interesting and useful consideration regards the possibility to parametrize the difference between the singlet and the triplet states by using spin operators \mathbf{S}_1 and \mathbf{S}_2 and the properties of coupled spins (see Appendix B). It is therefore straightforward to write an *effective Hamiltonian* starting from [12]

$$\mathcal{H} = \frac{1}{4}(E_s + 3E_t) - (E_s - E_t)\mathbf{S}_1 \cdot \mathbf{S}_2, \quad (2.15)$$

where the constant energy term can be adsorbed and the second term can be rewritten in terms of the exchange constant J_{ab} as

$$J_{ab} \equiv J = \frac{E_s - E_t}{2} \quad (2.16)$$

leading to a spin-dependent Hamiltonian

$$\mathcal{H} = -2J\mathbf{S}_1 \cdot \mathbf{S}_2 \quad (2.17)$$

The importance of this equation is related to the fact that it describes intrinsic physical proprieties by projecting those onto the spin only part of the wavefunctions. As it will be clear in the next sections, this procedure is often possible and simplifies the comprehension of the underlying magnetic quantum effects.

2.2.2 Simple model for direct exchange

Direct exchange is a consequence of the combination of Coulomb exchange with kinetic exchange, or the hopping of electrons. As a simple toy model one can consider the H_2 molecule, i.e. a system with two electrons on different ionic sites that can hop to the neighboring one. The matrix element that allows an electron to move will be given by $-t$ and also an on site Coulomb interaction U will be present when both electrons are on the same site.

The basis set of wavefunctions can be constructed starting from an orthogonal basis of one electron given, pictorially, by $\phi_1 = |\uparrow, \cdot\rangle$ and $\phi_2 = |\cdot, \uparrow\rangle$ in the specific case of a spin up electron.

The basis set for the two electron system will be

$$\begin{array}{ll} |\uparrow, \downarrow\rangle & |\downarrow, \uparrow\rangle \\ |\uparrow\downarrow, \cdot\rangle & |\cdot, \uparrow\downarrow\rangle \end{array} \quad \begin{array}{l} \text{Covalent states} \\ \text{Ionic states} \end{array} \quad (2.18)$$

$$(2.19)$$

and the Hamiltonian, written in this basis is

$$H = \begin{pmatrix} 0 & 0 & -t & -t \\ 0 & 0 & +t & +t \\ -t & +t & U & 0 \\ -t & +t & 0 & U \end{pmatrix} \quad (2.20)$$

whose + sign in the hopping elements is due to the Fermi statistics. The diagonalization of the Hamiltonian results in the following eigenvalues and eigenvectors [48]:

$$\begin{aligned} E_{\pm} &= \frac{U}{2} \pm \frac{\sqrt{U^2 + 16t^2}}{2}, & \Phi_{\pm} &= \frac{\left(|\uparrow, \downarrow\rangle - |\downarrow, \uparrow\rangle - (E_{\pm}/2t)[|\uparrow\downarrow, \cdot\rangle + |\cdot, \uparrow\downarrow\rangle] \right)}{\sqrt{2 + E_{\pm}^2/(2t^2)}} \\ E_{cov} &= 0, & \Phi_{cov} &= \frac{1}{\sqrt{2}} \left(|\uparrow, \downarrow\rangle + |\downarrow, \uparrow\rangle \right) \\ E_{ion} &= U, & \Phi_{ion} &= \frac{1}{\sqrt{2}} \left(|\uparrow\downarrow, \cdot\rangle - |\cdot, \uparrow\downarrow\rangle \right) \end{aligned}$$

This result is meaningful since it shows again that the energy depends on the spin configuration.

The physics behind direct exchange can be understood better if one considers the limit of large U, i.e. $U \gg t$, in fact two of the eigenfunctions have energies that rapidly increase as function of U (E_+ , E_{ion}), while the other two are always lower in energy (E_- , E_{cov}). Consequently one can try to split the states in order to consider only the latter ones, whose character is more covalent.

This can be achieved with the *downfolding technique* [62], that consists in partitioning the Hilbert space by projecting out of it the two high energy eigenfunctions. The others, in the limit of $U \rightarrow \infty$, become

$$\Psi_{cov,-} = \frac{1}{\sqrt{2}} \left(|\uparrow, \downarrow\rangle \pm |\downarrow, \uparrow\rangle \right) \quad (2.21)$$

The result of this procedure is an *effective Hamiltonian*

$$H_{eff} = \begin{pmatrix} -t & -t \\ +t & +t \end{pmatrix} \begin{pmatrix} \varepsilon - U & 0 \\ 0 & \varepsilon - U \end{pmatrix}^{-1} \begin{pmatrix} -t & +t \\ -t & +t \end{pmatrix} \simeq -\frac{2t^2}{U} \begin{pmatrix} 1 & -1 \\ -1 & 1 \end{pmatrix} \quad (2.22)$$

whose diagonalization brings to an effective interaction between the two eigensates of equation 2.21, with energies $\varepsilon_{cov} = 0$ and $\varepsilon_- = -4t^2/U$.

It is easy to recognize in the remaining wavefunctions the singlet state and one of the triplet ones of section 2.2.1, the latter being reduced to a single state because of Pauli Exclusion principle that acts cooperatively with the hopping.

The Hamiltonian can be rewritten in a more compact form by introducing the second quantization formalism [69].

$$\mathcal{H} = -t \left(c_{1\uparrow}^\dagger c_{2\uparrow} + c_{2\uparrow}^\dagger c_{1\uparrow} + c_{1\downarrow}^\dagger c_{2\downarrow} + c_{2\downarrow}^\dagger c_{1\downarrow} \right) + U \left(n_{1\uparrow} n_{1\downarrow} + n_{2\uparrow} n_{2\downarrow} \right) \quad (2.23)$$

$$= -t \sum_{i,j=1}^2 \sum_{\sigma=\uparrow,\downarrow} c_{i\sigma}^\dagger c_{j\sigma} + U \sum_{i=1}^2 n_{i\uparrow} n_{i\downarrow} \quad (2.24)$$

where $c_{1\sigma}^\dagger$, $c_{1\sigma}$ are the Fermionic creation and annihilation operators of an electron in the state 1 with spin σ and $n_{1\sigma}$ is the particle number operator for the same state. It is worth noticing that this equation is basically a two electron Hubbard Model (see Section 2.2.4). It is possible to demonstrate that equation 2.24 can be rewritten in terms of spin operators, in the approximation of $U \gg t$, as [62, 82]

$$H_{eff} = \frac{4t^2}{U} \left(\mathbf{S}_1 \cdot \mathbf{S}_2 - \frac{n_1 n_2}{4} \right) = J \left(\mathbf{S}_1 \cdot \mathbf{S}_2 - \frac{n_1 n_2}{4} \right) \quad (2.25)$$

Since J is always positive, the direct exchange interaction is antiferromagnetic.

2.2.3 Superexchange

In some compounds like MnF_2 , FeF_2 and CoF_2 antiferromagnetic phases have been observed [12, 82], even though the distance between atoms is large and the cations do not have strongly overlapped wavefunctions. In 1934 Kramers proposed a model for describing this phenomena [50], whose origin was addressed to the strong hybridization of the non magnetic ionic wavefunctions with the magnetic ones.

It can be understood using a simple model containing both onsite Coulomb interaction (U) and hopping term (t) analogous to the one of the previous section, but with three ionic sites M-O-M as in MnO (see Figure 2.1). For simplicity we assume that the magnetic moment on the Mn atom is due to one unpaired electron on the d orbital, while there are two electrons on the O p orbital. Then the possible situations are sketched in Figure 2.1.

If the starting configuration is an antiferromagnetic one (see Fig. 2.1 (a)) the possible excited states due to the hopping of electrons (see Fig. 2.1 (b) and (c)) are all allowed, while if the starting configuration is ferromagnetic (see Fig. 2.1 (d)), the two excited states are prohibited by Pauli exclusion principle. This interplay between ground and excited states is crucial for the appearance of antiferromagnetism in Transition Metal Oxides and must always be considered when describing such materials on a theoretical level.

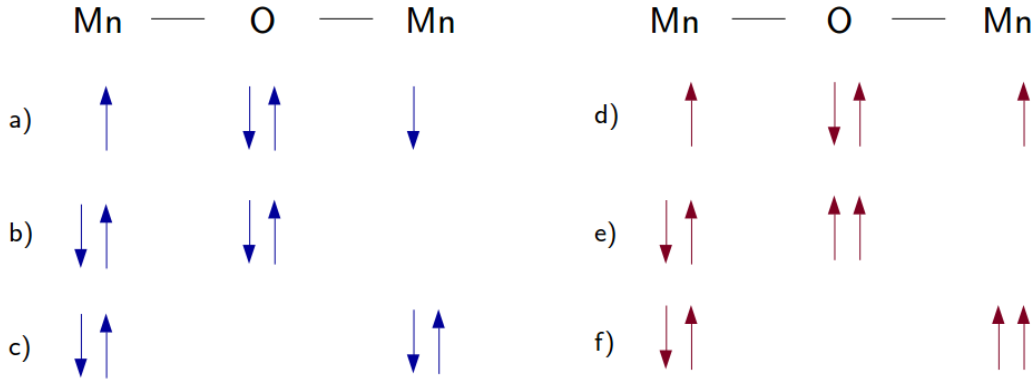


Figure 2.1: Magnetic phases for MnO. The left part of the plot shows the antiferromagnetic ground state configuration (a) and its excited states (b), (c). The right part shows the ferromagnetic ground state configuration (d) and its excited phases (e), (f) [12]

In this case, by following a mathematical procedure similar to the one of section 2.2.2, it is possible to show that the superexchange interaction between magnetic ions with angle between them of 180° is *antiferromagnetic*. Furthermore, a very significant result is that the magnetic interaction can be described by an effective Hamiltonian based on the cationic spin operators, i.e. it can be written as in equation 2.25, with

$$J = \frac{4t_{pd}^4}{(U_d + \Delta_{pd})^2} \left(\frac{1}{U_d} + \frac{1}{U_d + \Delta_{pd}} \right) \quad (2.26)$$

where t_{pd} is the hopping term between p-d orbitals, U_d is the on site Coulomb interaction on the d orbital and $\Delta_{pd} = \varepsilon_d - \varepsilon_p$ is the energy difference between the energy of an electron on the Mn site and the energy of an electron on the O site (see Figure 2.2 (a)).

The angle between the magnetic ions plays a significant role since it changes the number of orbitals involved and the final effective interaction itself as demonstrated by Goodenough and Kanamori [31, 32, 45], who enunciated two rules for establishing the nature of the superexchange interaction:

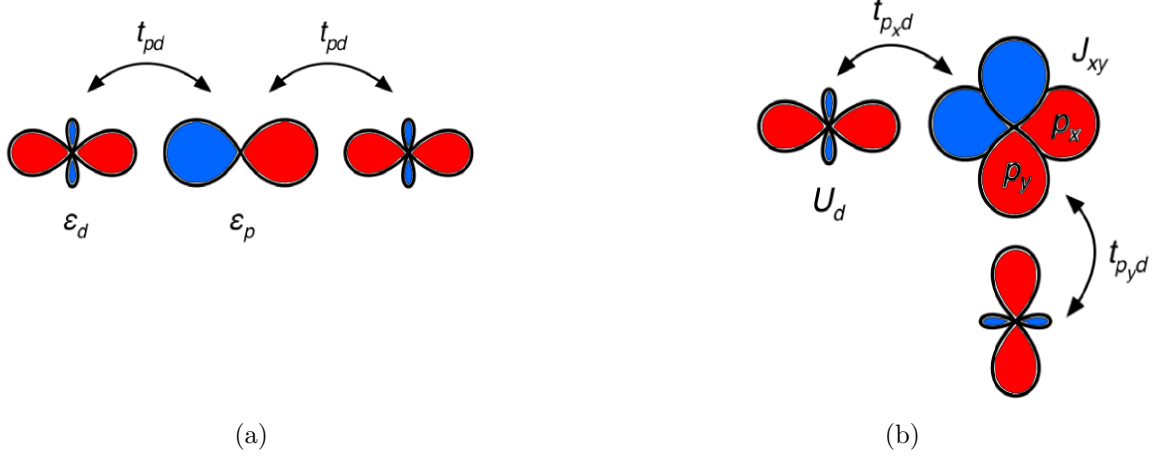


Figure 2.2: Exchange paths and Goodenough-Kanamori rules. (a) Simple graphical representation of a 180° exchange path between magnetic atoms. The orbitals on the sides are d orbitals, while the one in the middle is a p oxygen one. (b) Graphical representation of a 90° exchange path between magnetic atoms. Two p oxygen orbitals are needed in this case.

1. The electron transfer can happen only if the cation and anion orbitals are non orthogonal, i.e. they must overlap.
2. The exchange interaction is antiferromagnetic (ferromagnetic) if the angle between cations is 180° (90° respectively) .

The ferromagnetic order arising from superexchange interaction can be demonstrated by using a slightly different model (see Figure 2.2 (b)) where the angle between M -O -M is 90° , the exchange mechanism can occur only via Coulomb exchange on the connecting oxygen between two p orbitals.

By applying a similar approach of section 2.2.2, it is again possible to show that the ferromagnetic superexchange interaction can be described by an effective Hamiltonian that does not contain any contribution from the mediating oxygens and that depends only on the cationic spins (see eq 2.25).

In this case [48]

$$J = -\frac{4t_{pd}^4}{(U_d + \Delta_{pd})^2} \frac{2J_{xy}}{4(U_d + \Delta_{pd})^2 - J_{xy}^2} \quad (2.27)$$

where the new term J_{xy} is used for taking into account the Hund's first rule for the oxygen p orbitals.

2.2.4 Hubbard Model

The origin of the Hubbard Model traces back to 1960's, when Hubbard tried to describe, through a simple model, the behaviour of TMOs. It became rapidly one of the most studied models in solid state physics since it successfully reproduced the properties of strongly localized electronic systems and nowadays is still studied because of its capability to model a wide range of materials like Mott insulators or even superconductors [85].

In this section a simple overview of this model will be presented. It is necessary for understanding the connection between the theoretical description of TMOs and the computational procedure implemented in *ab initio* methods (see Section 2.3) that is impossible to disregard when one is interested in describing Mott insulators.

The Hubbard Hamiltonian (HH) in its basic version contains two terms

$$\mathcal{H} = H_T + H_U , \quad (2.28)$$

where the first is a single particle term or *tight binding* Hamiltonian, while the second is a two particle interaction in the form of a screened on site Coulomb interaction.

Written explicitly is

$$\mathcal{H} = - \sum_{ij} \sum_{\alpha\beta} t_{ij,\alpha\beta} c_{i\alpha}^\dagger c_{j\beta} + \sum_i \sum_{\alpha\beta\gamma\delta} U_{i,\alpha\beta\gamma\delta} c_{i\alpha}^\dagger c_{i\beta}^\dagger c_{i\gamma} c_{i\delta} \quad (2.29)$$

where $c_{i\alpha}^\dagger$, $c_{i\alpha}$ are the Fermionic creation and annihilation operators for electrons on the i -th ionic site in the α -th quantum state or atomic orbital and

$$U_{i,\alpha\beta\gamma\delta} = \langle \alpha\beta | U(|\mathbf{r}_1 - \mathbf{r}_2|) | \gamma\delta \rangle . \quad (2.30)$$

Equation 2.29 is a simplified version of the many body problem but is still prohibitively complex to solve analytically, and, even when a solution can be obtained, the estimation of the parameters involved is not a straightforward task [81]. This problem is usually approached via different techniques, from mean field analysis to diagrammatic theoretical methods, from *ab initio* electronic calculations to quantum Monte Carlo [28].

Here we will try to underline the main properties by making some approximations. The first and the more intuitive is to limit the number of states to the ones occupied by the valence d electrons in the transition metal ion (TMI). This already allows to reduce the number of constants also because, by symmetry considerations, many of the matrix elements in equation 2.30 are zero.

Our further assumption is that we can limit our model to a one orbital case and consider only nearest neighbor interaction, leading to

$$\mathcal{H} = -t \sum_{\langle i,j \rangle, \sigma} c_{i\sigma}^\dagger c_{j\sigma} + U \sum_i n_{i\uparrow} n_{i\downarrow} . \quad (2.31)$$

Here the interaction term is fully simplified and it consists of a constant U as well as the hopping term t . If one restricts the sum over the lattice sites to 2 it is easy to recognize the equation 2.24 already studied.

The main difference between this simplified version of the HH and the complete one consists on the number of interactions considered. It is a common approach to limit the number of parameters depending on the symmetry, strength of the interactions and exchange paths in a way that, in the end, it is possible to derive a phase diagram of the magnetic properties of the material under investigation. These phase diagrams will be encountered in section 3.1 and are usually a good yardstick for comparing the computational, experimental and theoretical results.

Here we will not investigate a model HH for our systems ($\text{Ba}_2\text{NaOsO}_6$ and $\text{Ba}_2\text{CaOsO}_6$) and we will instead consider two limiting cases:

Band Limit When $U \rightarrow 0$ the Hamiltonian can be exactly diagonalized via a Fourier Transform of the Fermionic operators

$$c_{\mathbf{k}\sigma}^\dagger = \frac{1}{\sqrt{N}} \sum_i e^{i\mathbf{k}\cdot\mathbf{r}_i} \quad (2.32)$$

where \mathbf{r}_i is the vector pointing at the i -th ionic site. The HH is then

$$\mathcal{H} = \sum_{\mathbf{k}} \sum_{\sigma} E(\mathbf{k}) c_{\mathbf{k}\sigma}^\dagger c_{\mathbf{k}\sigma} \quad (2.33)$$

where $E(\mathbf{k})$ is the energy dispersion relation in the reciprocal space. Under this limit it is possible to demonstrate that the magnetic susceptibility depends on the reciprocal vector \mathbf{q} near the Fermi surface, leading to a strong instability. Furthermore, depending on the shape of the Fermi surface, every classical magnetic order can be achieved [28].

Mott Limit When $t \rightarrow 0$ the Hamiltonian is already diagonal

$$\mathcal{H} = U \sum_i n_{i\uparrow} n_{i\downarrow} . \quad (2.34)$$

In the Mott limit, because of degeneracy, magnetism can always be present for some values of t . In particular, in contrast to what mentioned in the band limit, when $U \gg t$ and the half filling condition is imposed on the orbital, a superexchange Hamiltonian can be derived from a perturbation theory perspective. The appearance of antiferromagnetism is justified in the specific limit assumed and it is not the only magnetic order that can be achieved starting from the Hubbard Model and as we shall see in following sections (see 3.1).

2.2.5 Crystal Field

The electronic and magnetic properties of TMOs are strongly dependent on the electronic environment around the Transition Metal Ions. This effect is known as *crystal field effect* (CFE).

As starting point we consider an isolated atom. Its electronic states can be reasonably described by hydrogen like atomic orbitals because of the spherical symmetry and they can be labelled through the quantum numbers l (eigenvalue of the angular momentum operator \mathbf{L}) and m_l (eigenvalue of the angular momentum operator projected onto the z direction \mathbf{L}_z). Here $m_l = -l, -l + 1, \dots, l - 1, l$ [21]. As an example, the Os^{2+} atom with $l = 2$ (d orbital) has $2l + 1$ degenerate states.

While it is clear that this works for an isolated atom, ions in a crystal are not in a spherically symmetric environment. For example, in TMOs, the Transition Metal Ions are surrounded by neighboring oxygens with which they interact for "building" the chemical bonding. The presence of these ions can change the relative energies of the d orbitals and destroy degeneracy of the m_l states (see Fig 2.3 (a)).

A simple way of understanding this phenomenon is to consider the Os atom into a sphere of radius r which is uniformly charged, the energy of the 5 degenerate states is higher now because of the electrostatic interaction, but they are still degenerate.

When this uniform charge is splitted into 6 point charges around the atom (see Fig. 2.3 (c)) the d orbitals of the Os interact with them differently, depending on their symmetry. As a consequence, when the a d orbital overlaps with the point charge, the electrostatic interaction is higher and the state splits (see Fig. 2.3 (b)). This model is known as *point charge approximation*. The effect considered so far is essentially a linear correction in perturbation theory due to bonding and antibonding, which is formally and better described by group theory.

A remarkable consequence of the CFE concerns the magnetic ground state. In fact, the interplay between Coulomb interaction, Pauli exclusion principle and crystal field can lead to different magnetic ground states. From Figure 2.3 (b), if one considers the case of an ion with 1,2,3 and 8,9,10 electrons it is easy to see that the way they occupy the t_{2g} and e_g states is univoque. On the other hand, when 4,5,6, or 7 valence electrons are taken into account, it is clear that two possible arrangements of the spins can happen:

High spin The high spin configuration appears when the electrostatic interaction is stronger than the crystal field. Therefore it is more convenient for the electrons to occupy the e_g states even though they are higher in energy, leading to a net ferromagnetic phase. This limit is also known as the *weak-field case*.

Low spin If the crystal field energy is larger than the Coulombic interaction (*strong field case*), electrons will first doubly occupy the low lying states leading to ferromagnetic (4,5 electrons) or antiferromagnetic (6 electrons) phases.

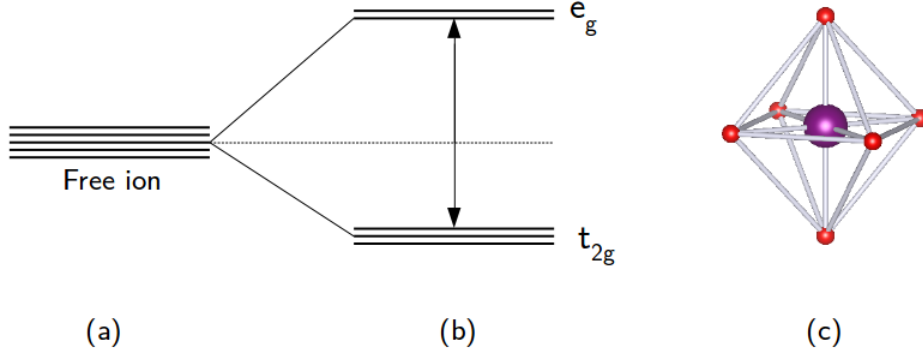


Figure 2.3: Energy splitting of d orbitals in an octahedral environment. In (a) there is the pictorial representation of the 5 degenerate d orbitals, while in (b) is shown the splitting due to the octahedral environment graphically seen in (c).

In the case of $\text{Ba}_2\text{NaOsO}_6$, if no other effects are involved, the Os d^1 electron will reside on one of the degenerate t_{2g} levels.

2.2.6 Spin-Orbit Coupling

Another effect that is relevant in TMOs and that cannot be ignored is the Spin-Orbit interaction or Spin-Orbit Coupling (SOC). It is a relativistic interaction between the spin of the electron with its orbital motion inside an atom.

On a semiclassical level it can be understood as a consequence of the influence on the electron arising from the magnetic field generated by the ion, in the reference frame of the electron:

$$\mathbf{B} = \frac{\boldsymbol{\mathcal{E}} \times \mathbf{v}}{c^2}, \quad (2.35)$$

where $\boldsymbol{\mathcal{E}}$ is the electric field due to the nucleus and \mathbf{v} is the velocity of the electron in its orbital state. It interacts with the spin moment of the electron leading to a term

$$\mathcal{H}_{SO} = \lambda \mathbf{S} \cdot \mathbf{L} \quad (2.36)$$

that couples its spin and orbital momentum. It is a relativistic effect since it can be formally derived only through Lorentz transformations between reference frames and it is intrinsically present in the Dirac's equation, i.e. in the equation that describes the quantum mechanical motion of relativistic particles.

The coupling constant λ in equation 2.36 has the following expression

$$\lambda = \frac{e\hbar^2}{2m_e c^2 r} \frac{dV(r)}{dr} \quad (2.37)$$

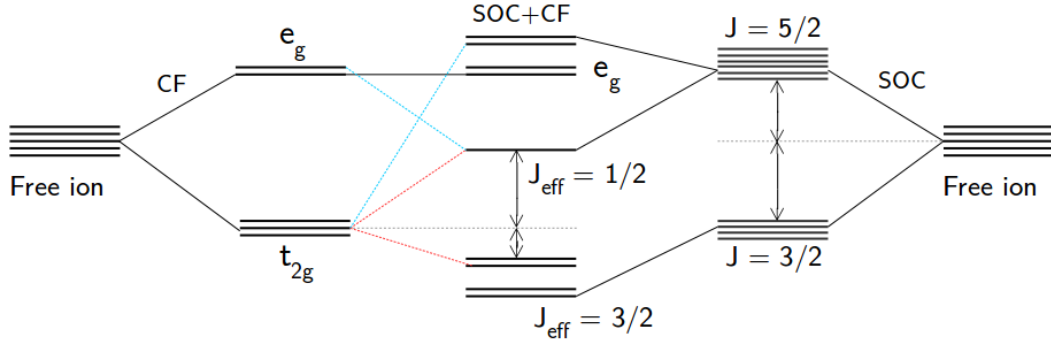


Figure 2.4: Evolution of the d orbitals under CFE and SOC. The far left and right part of the figure show the degeneracy of the d orbitals in a free atom. Coming from left there is (first) the energy splitting due to CFE, then (second) the further split of the t_{2g} states under SOC and finally (third) the splitting of the d orbitals caused only by SOC.

that can be explicitly derived for the specific case of a Coulomb field into an hydrogen like atom leading to the potential term

$$\frac{1}{r} \frac{dV(r)}{dr} = \frac{Ze^2}{4\pi\epsilon_0 r^3} . \quad (2.38)$$

This result, although strictly valid for a limited class of atoms, is meaningful because it shows that the SOC increases with the atomic number i.e. it becomes stronger the further the atom is in the periodic table. The relative strength of SOC with respect to CFE can change significantly the physics of TMOs as we will see in the following lines. But meanwhile it is important to analyze the consequences of the coupling $\mathbf{S} \cdot \mathbf{L}$.

In analogy with the Heisenberg Hamiltonian found previously (see Section 2.2.3), can be rewritten in terms of a new operator $\mathbf{J} = \mathbf{S} + \mathbf{L}$ called *total angular momentum* whose eigenvalues are given by the summation rules for momenta (see Appendix B). As an example, the d^1 electron of the Os atom in $\text{Ba}_2\text{NaOsO}_6$ without CFE has spin $S = 1/2$ and orbital momentum $L = 2$ and so its total angular momentum eigenvalues will be $J = 3/2, 5/2$ and the SOC energy term will be

$$\mathcal{H}_{SO} = \begin{cases} \lambda & \text{if } J = 5/2 \\ -\lambda & \text{if } J = 3/2. \end{cases} \quad (2.39)$$

The 5 fold degenerate d states are splitted in a sextet for $J = 5/2$ since degeneracy is given by $(2J + 1)$ and a quadruplet for $J = 3/2$.

The last ingredient that is necessary for comprehending the effect of SOC on the magnetic phase derives from the coupling between spin and the fictitious angular momentum

given by the CFE. In the specific case of an ion in an octahedral environment, the CFE leads to the two groups of degenerate states t_{2g} and e_g (see Section 2.2.5), the orbital angular momentum of the t_{2g} states can be described by a "fictitious" operator \mathbf{L} with eigenvalue $l = 1$ obtainable through a projection operator $\mathcal{P}_{t_{2g}}$, i.e.

$$\mathcal{P}_{t_{2g}} \mathbf{L} \mathcal{P}_{t_{2g}} = -\mathbf{L} . \quad (2.40)$$

When the spin is coupled to this operator via

$$\mathcal{H}_{SOC} = -\lambda \mathbf{S} \cdot \mathbf{L} \quad (2.41)$$

it leads to a total angular momentum operator \mathbf{j}_{eff} whose eigenvalues are $j_{eff} = 3/2$ (quadruplet) and $j_{eff} = 1/2$ (doublet). Now, by looking at figure 2.4 should be clear that several regimes can be found depending on the relative strenght of SOC and CFE: *Weak SOC*, *Strong SOC* and *very strong SOC* (Not considered here).

Weak SOC : In this case this inequality holds $CFE \gg SOC$ and therefore the electronic levels are not influenced by the SOC effect. This case, however can lead to non conventional magnetic configurations like zig-zag antiferromagnetic (Kitaev) or canted antiferromagnetic ones [55]. This can be understood by using a model Hamiltonian containing three terms

$$\mathcal{H} = \mathcal{H}_0 + \mathcal{H}_{CF} + \mathcal{H}_{SOC} \quad (2.42)$$

where \mathcal{H}_0 is a Hubbard like Hamiltonian that contains all the atomic and exchange contributions.

When SOC is weak both the spin and angular momentum operators are good quantum numbers allowing to project the full Hamiltonian onto a Spin Hamiltonian of the form

$$\mathcal{H} = \sum_{i \neq j} \mathbf{S}_i^T \underline{\mathbf{V}}_{ij} \mathbf{S}_j \quad (2.43)$$

where $\underline{\mathbf{V}}$ is a 3×3 matrix

$$\underline{\mathbf{V}}_{ij} = \begin{pmatrix} V_{11} & V_{12} & V_{13} \\ V_{21} & V_{22} & V_{23} \\ V_{31} & V_{32} & V_{33} \end{pmatrix} \quad (2.44)$$

and $\mathbf{S}_i, \mathbf{S}_j$ are the semi classical vectors referred to two interacting spins. This procedure is based on the assumption that a spin component has a perfectly definite component, i.e. with no uncertainty on the eigenvalues, while the others are completely undefined. For example, if we consider S_z has the defined component, then the relative mean squared deviation is

$$\frac{\langle |\mathbf{S} - S_z \hat{z}|^2 \rangle}{\langle \mathbf{S}^2 \rangle} \approx \frac{Const}{S} , \quad (2.45)$$

and the uncertainty of the angle of the spin, on a mean field level, is $O(1/\sqrt{S})$ and tends to 0 in the limit of $S \rightarrow \infty$ [41]. The mean field treatment allows to consider, in the end, the spin as a classical vector pointing at an arbitrary direction onto a sphere of radius S .

The interacting matrix is decomposed in three terms: a *isotropic part* J_{ij} , a *symmetric traceless part* $\underline{\mathbf{V}}^S$ and an *antisymmetric part* $\underline{\mathbf{V}}^A$, such that

$$\mathcal{H} = J_{ij} \mathbf{S}_i \cdot \mathbf{S}_j + \mathbf{S}_i^T \underline{\mathbf{V}}^S \mathbf{S}_j + \mathbf{S}_i^T \underline{\mathbf{V}}^A \mathbf{S}_j . \quad (2.46)$$

Now, since any antisymmetric (3×3) matrix can be expressed as a vector quantity, the antisymmetric interaction can be rewritten as

$$\mathbf{S}_i^T \underline{\mathbf{V}}^A \mathbf{S}_j = \mathbf{D}_{ij} \cdot (\mathbf{S}_i \times \mathbf{S}_j) , \quad (2.47)$$

that is the *Dzyaloshinskii-Moriya interaction* (DMI). For the symmetric traceless part it is reasonable to assume $\underline{\mathbf{V}}_{ij}^S = \underline{\mathbf{V}}_{ii}^S$ leading to the so called *Single Ion Anisotropy* (SIA) term. It should be clear that the isotropic part is nothing but the Heisenberg Hamiltonian.

This result, that we rewrite in its complete form

$$\mathcal{H} = \sum_{ij} J_{ij} \mathbf{S}_i \cdot \mathbf{S}_j + \sum_i H_{(SIA)} + \sum_{ij} \mathbf{D}_{ij} \cdot (\mathbf{S}_i \times \mathbf{S}_j) \quad (2.48)$$

can be obtained also through a perturbative approach by considering both the CFE and a weak SOC term, the latter leading to the DMI and SIA contributions [23, 61]. The SIA describes the coupling between the spin and lattice degrees of freedom and depends on the local symmetry of the magnetic ions, while the DMI depicts the relativistic effects.

Strong SOC In this case $CF \sim SOC$ or even $SOC > CF$. The impact of the SOC onto the t_{2g} states is given, pictorially in the middle inset of Figure 2.4 explicitly for the d^1 electron in Os in $\text{Ba}_2\text{NaOsO}_6$. In this case an accepted and used procedure [19, 20] is to project the operators involved in Equation 2.42 first onto the t_{2g} states and then again onto the j_{eff} ones. As an example, being $\mathcal{H}_{t_{2g}}$ the Hamiltonian for a specific TMO like $\text{Ba}_2\text{NaOsO}_6$, the action of the projector operator $\mathcal{P}_{3/2}$ onto the $j_{eff} = 3/2$ states will give

$$\mathcal{P}_{3/2} \mathcal{H}_{t_{2g}} \mathcal{P}_{3/2} = \tilde{\mathcal{H}}_{t_{2g}} , \quad (2.49)$$

restricting the Hilbert space to four low lying states, whose j_{eff}^z eigenvalues are $3/2$, $1/2$, $-1/2$ and $-3/2$. Then, this new Hamiltonian contains exchange interactions that are orbital dependent and that can lead to interactions of higher order than bipolar, like quadrupolar or octupolar. Their expression can be derived starting from an Hubbard like Hamiltonian or as a sum of multipolar tensor products [43, 68]. There is no univoque consensus over the more appropriate procedure and we will follow the latter one for the analysis of the computational results (see Section 4.4) [20].

2.2.7 Jahn-Teller effect

In section 2.2.5 the effect of the arrangement of atoms on the magnetic ground state was introduced, but it does not complete the description of the correlation between lattice degrees of freedom and the magnetic ones. In fact it was observed that, in order to minimize the energy related to the magnetic configuration, the crystal structure can locally distort and further lower its symmetry [44]. This happens because the increase in elastic energy is balanced or, more often, overcome by the energy saving due to the distortion. This phenomenon is known as *Jahn Teller distortion*.

The result is that there is a further split of the orbitals (see Figure 2.5) that can enhance a specific magnetic ground state. Jahn-Teller distortions are quite common in TMOs and in double perovskites (see Section 3.1) where the octahedra tend to rotate, tilt and distort in several ways. The focus here will be made on two specific cases that are the two depicted in Figure 2.5, where the effect of a symmetric elongation or a compression of the bonds along the z direction are applied to an octahedral environment.

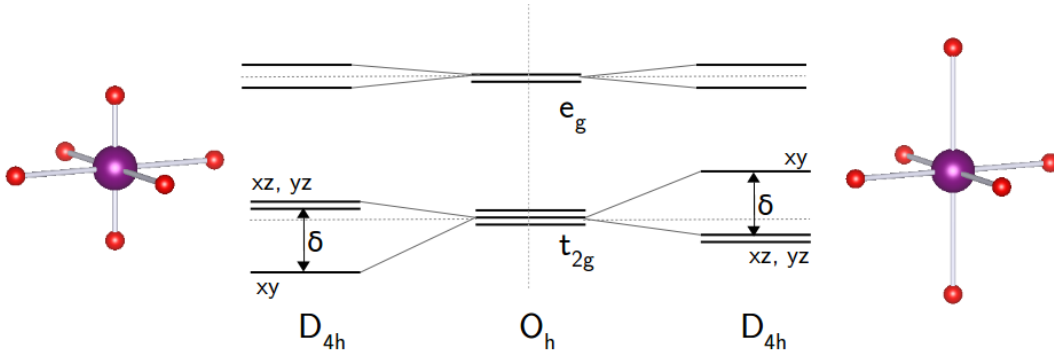


Figure 2.5: Jahn-Teller effect on t_{2g} states. The left inset and the right ones represent respectively a compression and an elongation of an octahedra. The figure shows, for the two cases how the t_{2g} states split when such distortions occur. For sake of completeness also the energy shift of the e_g states is shown.

The Point Group changes from O_h to D_{4h} and the t_{2g} orbitals are splitted in a singlet and a doublet states by a quantity δ , more specifically the d_{xy} are shifted by an amount $\delta_{xy} = +2/3 \delta$ ($\delta_{xy} = -2/3 \delta$) and the d_{xz} , d_{yz} by an amount $\delta_{xz,yz} = -1/3 \delta$ ($\delta_{xz,yz} = +1/3 \delta$) if an elongation (compression) is applied to the octahedra. The "still" degenerate d_{xz} and d_{yz} orbitals can further split if the symmetry is further lowered, i.e. if other distortions in the xy plane occur.

2.3 Density Functional Theory

Density Functional Theory (DFT) is, nowadays, one of the most important methods for investigating matter and solving the many body problem from a quantum mechanical approach. This is proven by the enormous variety of systems that can be treated via DFT, from binding energy of molecules to the band structure of solids, from magnetic properties of materials to polarons on surfaces [22, 66].

This section is focused on the theoretical derivation of DFT, i.e. on the attempts to solve the many body problem thanks to the Kohn Hohenberg theorems as well as on the possible practical implementations obtainable through the Kohn Sham equations. These will be the starting point for understanding how DFT codes like the one used (Vienna Ab initio Simulation Package) actually allow to calculate the properties of interest of materials. The last part will deal with the resolution of very important computational problems that are strongly related to the materials studied: the Mott Insulator problem and the extension of DFT for magnetic systems with SOC interaction.

One of the biggest obstacles in the theoretical study of solid state physics is to solve the non relativistic many body problem of equation 2.4, which can be re expressed as

$$\mathcal{H} = T + U + \int v(\mathbf{r})n(\mathbf{r})d\mathbf{r} , \quad (2.50)$$

where T, U are the *kinetic energy* and the *Coulomb interaction* between electrons, while the third term is the contribution from the electrostatic interaction between electrons and nuclei in the lattice. The difficulty in solving such equation arises mainly from the Coulombic term, which couples electrons on different positions, leading to an expression that can not be reduced to a single particle Hamiltonian.

This is because in quantum mechanics, the standard approach used to solve the Schrödinger equation is to specify the external potential $v(\mathbf{r})$, then calculate the eigenvalue problem which gives the (many body) wavefunction Ψ that will be used then for calculating the expectation values of operators. This process is analytically prohibitive for real solids since the number N of electrons is $\sim 10^{24}$, meaning that the wavefunction of the many body system has $3N$ coordinates, if we assume that it is real and ignore the spin. Some powerful methods has been proposed, like the diagrammatic perturbation theory, which is based on Greens functions and Feynman diagrams which, although very accurate, are computationally expensive for large systems. Therefore DFT, as we will show, is a valid alternative, sometimes less accurate, but theoretically exact.

The main feature of DFT is to promote the single electron density $n(\mathbf{r})$, defined as

$$n(\mathbf{r}) = N \int d\mathbf{r}_2 \int d\mathbf{r}_3 \dots \int d\mathbf{r}_N \Psi^*(\mathbf{r}, \mathbf{r}_2, \dots, \mathbf{r}_N) \Psi(\mathbf{r}, \mathbf{r}_2, \dots, \mathbf{r}_N) \quad (2.51)$$

from a simple observable to a key variable, from which all the calculations can be derived. Furthermore the DFT approach differs from the "classical" one and it can be summarized in three steps. The first consists in deriving $n(\mathbf{r})$ from which, in the second step, the many body wavefunction can be obtained. Finally the knowledge of the wavefunction implies the knowledge of the external potential and therefore of all the other variables. This scheme represents the ideal structure of DFT, even though, as we will see, it differs from the practical implementation.

2.3.1 Hohenberg-Kohn theorems

The cornerstones of DFT are two theorems named *Hohenberg and Kohn theorems* after their discoverers, which will be introduced here without proof (that can be found in several books [22, 27, 67]).

Theorem 1. *The external potential $v(r)$ is a functional of the electron density $n(r)$ and it is determined, within a trivial additive constant, by the ground state electron density $n_0(r)$.*

The first Hohenberg and Kohn theorem can be also rewritten in another form known as *strong form* [34, 78]

$$\int \Delta v(\mathbf{r}) \Delta n(\mathbf{r}) < 0 \quad (2.52)$$

where $\Delta v(\mathbf{r})$ and $\Delta n(\mathbf{r})$ correspond to the change in potential and electron density respectively. It is straightforward to see that if $\Delta v(\mathbf{r}) \neq 0$ is impossible to have $\Delta n(\mathbf{r}) = 0$ i.e. a change in the potential determines a change in the electron density.

The meaning of this theorem is, ultimately, that given a ground state density $n_0(\mathbf{r})$ is possible to derive the corresponding ground state wave function $\Psi_0(\mathbf{r}_1, \mathbf{r}_2, \dots, \mathbf{r}_N)$. In fact, since $v(\mathbf{r})$ is uniquely determined by the ground state density, the knowledge of it automatically gives the knowledge of the full Hamiltonian, or, in other words, the many body wavefunction is a functional of $n(\mathbf{r})$

$$\Psi_0(\mathbf{r}_1, \mathbf{r}_2, \dots, \mathbf{r}_N) = \Psi[n_0(\mathbf{r})] . \quad (2.53)$$

Hence, the expectation value of an operator \hat{O} in the ground state is

$$\langle \hat{O} \rangle_0 = \langle \Psi[n_0(\mathbf{r})] | \hat{O} | \Psi[n_0(\mathbf{r})] \rangle = O[n_0(\mathbf{r})] \quad (2.54)$$

and it is, itself, a functional of the ground state electron density.

Among all the observables, the most important is the energy, given by the expectation value of the Hamiltonian. By inserting the Hamiltonian of equation 2.50 into the expression above it is easy to find that

$$E_0 = E[n_0(\mathbf{r})] = \langle \Psi[n_0(\mathbf{r})] | \hat{\mathcal{H}} | \Psi[n_0(\mathbf{r})] \rangle = F_{HK}[n_0(\mathbf{r})] + \int v(\mathbf{r}) n_0(\mathbf{r}) d\mathbf{r} , \quad (2.55)$$

where $F_{HK}[n(\mathbf{r})]$ is called the *Hohenberg-Kohn* functional and it represents the system-independent part or *universal* part of the Hamiltonian. It is "universal" since its expression does not depend on the specific system considered

$$F_{KH}[n(\mathbf{r})] \equiv \langle \Psi[n_0(\mathbf{r})] | \hat{T} + \hat{U} | \Psi[n_0(\mathbf{r})] \rangle . \quad (2.56)$$

The second Hohenberg Kohn theorem pushes forward the knowledge of the ground state energy by stating that

Theorem 2. *Given an arbitrary single electron density $\tilde{n}(\mathbf{r})$, such that $\tilde{n}(\mathbf{r}) \geq 0$ one can never obtain a ground state energy below the one obtained via $n_0(\mathbf{r})$, or, in other words*

$$E[n_0(\mathbf{r})] \leq E[\tilde{n}(\mathbf{r})] \quad (2.57)$$

This theorem, proved by Levy and Lieb [53, 67], basically means that the ground state energy can be obtained via variational approach by minimizing E

$$E_0 = \min_{\Psi'} \langle \Psi' | \hat{\mathcal{H}} | \Psi' \rangle \quad (2.58)$$

and imposing the constraint on the total particle number N

$$\frac{\delta E[n]}{\delta n(\mathbf{r})} = \mu = \frac{\partial E}{\partial N} , \quad (2.59)$$

where Ψ' in equation 2.58 is an arbitrary manybody wavefunction and μ in equation 2.59 is the chemical potential.

So far the robustness of the DFT approach has been showed, but this was because some conceptual problems were intentionally swept under the carpet til now. These are known as the *N representability problem* and *v representability problem*.

N representability concerns the fact that, given an arbitrary function $n(\mathbf{r})$, is not necessary true that there is a corresponding N-body antisymmetric wavefunction from which it can be derived (see eq 2.51). This problem for a single particle density was solved and now it can be demonstrated that any non negative function can be written in terms of an antisymmetric $\Psi_0(\mathbf{r}_1, \mathbf{r}_2, \dots, \mathbf{r}_N)$ [30, 38].

The *v* representability regards the knowledge of $v(\mathbf{r})$ from the electron density. In fact, in principle, it can happen that for a given function $n_0(\mathbf{r})$ there is no corresponding local potential $v(\mathbf{r})$ and therefore no real physical system. Indeed the Hohenberg Kohn first theorem guarantees that cannot exist more than one potential for a given electronic ground state density, but it does not exclude that can be less than one. In general it can be demonstrated [54, 80] that in *discretized systems* every density is *ensemble v* representable. The *v* representability problem however has still no solution in the case of continuous systems with pure states, but this still does not prevent to use it as a computational approach to solid state physics.

Another problem arises as soon as the information about the excited states is required. Recalling that all the informations obtained on the physical system correspond to the ground state properties, it could be assumed that the other extrema of the functional $E[n(\mathbf{r})]$ correspond to excited state densities as well. This is the case, but, on the other hand not every excited state density is an extrema of the functional, i.e. those solutions are effective excited state, but they do not cover the entire spectra [17, 63].

2.3.2 Kohn-Sham equations

The route followed till now is correct, but impractical for calculation purposes. The desirable way for calculating the energy functional would be to use an iterative approach as the ones often found in cases when it is prohibitive to find an analytic solution.

This task can be achieved thanks to the *Kohn Sham equations*. Kohn and Sham investigated the possibility to transform the density functional theory to an N non interacting particle problem, in a way that reminds the Hartree's method [39].

The starting point of the Hartree's method is to consider the electrons moving in an effective single-particle potential $v_H(\mathbf{r})$ of the form

$$v_H(\mathbf{r}) = v(\mathbf{r}) + \int \frac{n(\mathbf{r}')}{|\mathbf{r} - \mathbf{r}'|} d\mathbf{r}' . \quad (2.60)$$

The electron electron interaction is therefore taken into account as an effective interaction in the new external potential, leading to a form of the Schrödinger equation that can be reduced to a set of single particle equations. The energy term is therefore given by

$$E[n(\mathbf{r})] = \int v(\mathbf{r})n(\mathbf{r})d\mathbf{r} + \hat{T}_S[n(\mathbf{r})] \quad (2.61)$$

where $\hat{T}_S = -\frac{1}{2}\nabla^2$ is the *non correlated* kinetic energy term. Applying the Euler-Lagrangian equation for this case gives [17]

$$\delta E[n(\mathbf{r})] = \int \delta n'(\mathbf{r}) \left[v_H(\mathbf{r}) + \frac{\delta}{\delta n'(\mathbf{r})} T_S[n'(\mathbf{r})] \Big|_{n'(\mathbf{r})=n(\mathbf{r})} - \epsilon \right] d\mathbf{r} = 0 \quad (2.62)$$

where ϵ is the Lagrangian multiplier. For a system of non interacting particles the total energy is straightforward

$$E = \sum_{i=1}^N f_i \epsilon_i , \quad (2.63)$$

here f_i is the occupation of the i-th orbital, and the electronic density is

$$n(\mathbf{r}) = \sum_{i=1}^N f_i |\phi_i(\mathbf{r})|^2 . \quad (2.64)$$

Kohn and Sham used this approach, but they substituted the kinetic energy term \hat{T}_S with the universal energy potential of equation 2.56 in the form

$$F[n(\mathbf{r})] = \hat{T}_S[n(\mathbf{r})] + \frac{1}{2} \int \frac{n(\mathbf{r})n(\mathbf{r}')}{|\mathbf{r} - \mathbf{r}'|} d\mathbf{r}d\mathbf{r}' + E_{xc}[n(\mathbf{r})] \quad (2.65)$$

where the second term describes the electrostatic self repulsion of electron density and the last term is known as *exchange-correlation* energy and accounts for two separate effects:

Exchange It is an example of a more general property of indistinguishability of particles in quantum physics, which leads to correlations. It was already treated in section 2.2.1 for magnetic interactions in TMOs, but here the focus is given on the energetic contribution to equation 2.65. A way of approaching this topic is to start from the Hartree approximation, where all correlations are neglected except those required by the Pauli exclusion principle. As seen previously the instantaneous electron-electron repulsion is replaced with a repulsion of each electron with an average electron charge cloud. As a consequence the energy has an exchange term equivalent to the one found in equation 2.12, which, in turn, lowers the total energy. The exchange term can be interpreted as the interaction of each electron with a positive *exchange hole* whose density is given by

$$\Delta n_x(\mathbf{r}, \sigma, \mathbf{r}', \sigma') = -\delta_{\sigma, \sigma'} \left| \sum_i \Psi_i^\sigma(\mathbf{r}) \Psi_i^{\sigma'}(\mathbf{r}') \right| \quad (2.66)$$

if the spin orbitals are orthonormal. The properties of the exchange hole are two:

- 1) $\Delta n_x(\mathbf{r}, \sigma, \mathbf{r}', \sigma') \leq 0$
- 2) The integral over \mathbf{r}' of $\Delta n_x(\mathbf{r}, \sigma, \mathbf{r}', \sigma')$ is exactly one missing electron per electron at any point \mathbf{r} .

The exchange-hole can be evaluated for simple cases like the H atom and for the He one, while for systems with many electrons numerical calculations are required. An exception is the homogeneous gas approximation [67].

Correlation The Hartree approximation does not consider the real electron-electron interaction, leading to an error in the wavefunction and that has an impact on the total energy. The energy error is called *correlation energy* and it is defined as

$$E_c = E_{exact} - E_{HF} \quad (2.67)$$

where E_{HF} is the Hartree Fock energy. Another way of defining this quantity will be given after having introduced the Kohn-Sham equations.

The Euler-Lagrange equations for interacting electrons becomes

$$\delta E[n(\mathbf{r})] = \int \delta n(\mathbf{r}) \left[v_{eff}(\mathbf{r}) + \frac{\delta}{\delta n(\mathbf{r})} T_S[n(\mathbf{r})] - \epsilon \right] d\mathbf{r} = 0 \quad (2.68)$$

where

$$v_{eff}(\mathbf{r}) = v_H(\mathbf{r}) + v_{xc}(\mathbf{r}) . \quad (2.69)$$

This is the *first Kohn-Sham equation*. The exchange-correlation potential is defined through the variational equation

$$v_{xc} = \frac{\delta}{\delta n(\mathbf{r})} E_{xc}[n(\mathbf{r})] . \quad (2.70)$$

Consequently, one can calculate the density of the interacting many body problem in an external potential $v(\mathbf{r})$ by solving the Schrödinger equations of a noninteracting electrons that "feel" an effective potential $v_{eff}(\mathbf{r})$

$$\left[-\frac{1}{2}\nabla^2 + v_{eff}(\mathbf{r}) \right] \phi_j(\mathbf{r}) = \epsilon_j \phi_j(\mathbf{r}) \quad j = 1, 2, \dots, N \quad (2.71)$$

which yield to single particle orbitals $\phi_i(\mathbf{r})$ that have the property of reproducing the density of the original system

$$n(\mathbf{r}) = \sum_{i=1}^N f_i |\phi_i(\mathbf{r})|^2, \quad (2.72)$$

This equation is the *second Kohn-Sham equation*.

It is worth to underline that the eigenvalues of the Schrödinger equation 2.71 are not the real energy eigenvalues, that are given instead by [17]

$$E = \sum_i \epsilon_i + E_{xc}[n(\mathbf{r})] - \int v_{xc}(\mathbf{r}) n(\mathbf{r}) d\mathbf{r} - \int \int \frac{n(\mathbf{r}) n(\mathbf{r}')}{|\mathbf{r} - \mathbf{r}'|} d\mathbf{r} d\mathbf{r}' . \quad (2.73)$$

This is not the end of the story, in fact two interesting observations can be made on the Kohn-Sham procedure.

The first regards the exchange-correlation energy: the functional $E_{xc}[n]$ can be approximated locally as a functional of the density, and therefore can be expressed as

$$E_{xc} = \int n(\mathbf{r}) \epsilon_{xc}([n], \mathbf{r}) d\mathbf{r} \quad (2.74)$$

where $\epsilon_{xc}([n], \mathbf{r})$ is the exchange-correlation potential energy per electron that depends on the electronic density in some point near to \mathbf{r} . It is clear that, the more ϵ_{xc} accurately

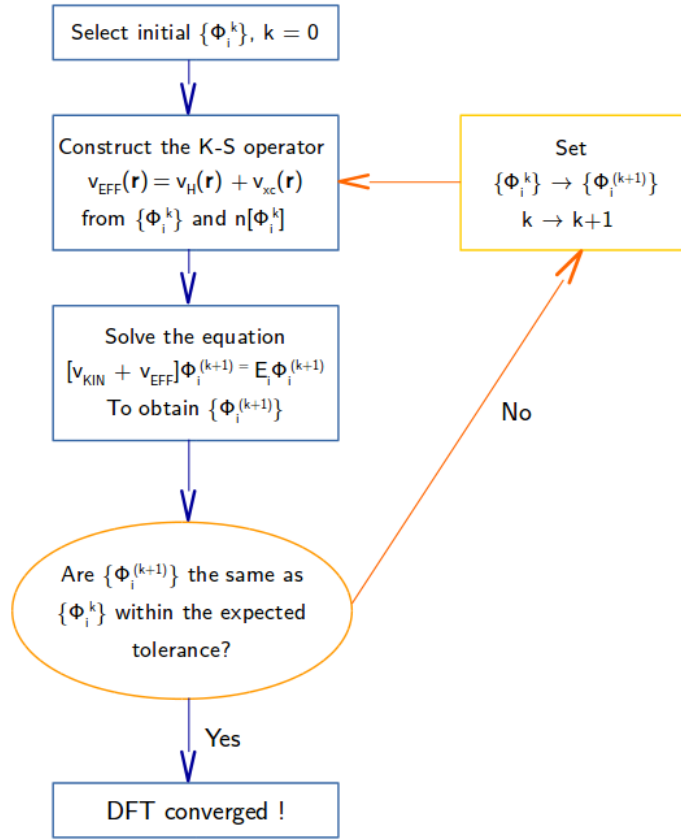


Figure 2.6: DFT self consistent cycle. The graph shows a typical self consistent cycle implemented in DFT programs in order to solve the Kohn-Sham equations. Here k is the number of iterations.

reproduces the true E_{xc} , the closer will be total energy functional to the real physical value.

The second consideration is about the first Kohn-Sham equation 2.69: both v_H and v_{xc} depend on $n(\mathbf{r})$, but it depends on $\phi_i(\mathbf{r})$ which already is a function of v_{eff} . Therefore the problem of solving 2.69 is a non linear problem and a self consistent cycle is necessary (see Figure 2.6).

2.3.3 Functionals for Exchange and Correlation

The crucial quantity in the Kohn-Sham approach is the Exchange-Correlation (XC) energy, which can be expressed as a functional of the density. More specifically, the Kohn-Sham equations demonstrate that a many body problem can be reduced to a system of non interacting particles and that, apart from the kinetic energy term and the Hartree one, the last constituent is exactly the XC functional, or, in other words,

$$E_{xc}[n] = \mathcal{E}_{exact} - F[n(\mathbf{r})] . \quad (2.75)$$

In this section the two most used approaches for describing E_{xc} , Local Density Approximation (LDA) and the Generalized Gradient Approximation (GGA), will be briefly described.

The LDA functional is derived from the hypothesis that many solids can be considered close to the homogeneous gas behaviour. The XC energy is therefore given by

$$E_{xc}^{LDA}[n] = \int n(\mathbf{r})\varepsilon_{xc}(n)d\mathbf{r} , \quad (2.76)$$

where ε_{xc} is the XC energy per particle of a homogeneous electron gas of charge density $n(\mathbf{r})$.

The success of this functional is given by the fact that the expression of the exchange part is known analytically

$$E_x^{LDA}[n] = -\frac{3}{4} \left(\frac{3}{\pi} \right)^{1/3} \int n(\mathbf{r})^{4/3} d\mathbf{r} \quad (2.77)$$

and also the correlation functional is known in the high and low density limits [22], while for intermediate correlations Quantum Monte Carlo simulations have been performed and provided accurate solutions [18].

An improvement of the XC functional can be obtained with the GGA, where it is assumed that the functional depends not only on the density $n(\mathbf{r})$, but also on its gradient $|\nabla n(\mathbf{r})|$. Several ways to introduce this term has been proposed [22] so it is more convenient to define the functional in a generalized form as

$$E_{xc}^{GGA}[n] = \int n(\mathbf{r})\varepsilon_{xc}^{GGA}(n(\mathbf{r}), |\nabla n(\mathbf{r})|)d\mathbf{r} , \quad (2.78)$$

where most of the GGA functionals are constructed in the form of a correction added to the LDA functional, like

$$\varepsilon_{xc}^{GGA}[n] = \varepsilon_{xc}^{LDA}[n] + \Delta\varepsilon_{xc} \left[\frac{|\nabla n(\mathbf{r})|}{n^{4/3}(\mathbf{r})} \right] . \quad (2.79)$$

Other efforts for improving accuracy were made by introducing the Laplacian of the density $\nabla^2 n(\mathbf{r})$. These functionals are known as Meta-GGA (MGGA). In practice, instead of $\nabla^2 n(\mathbf{r})$, the kinetic energy density

$$\tau(\mathbf{r}) = \sum_i \frac{1}{2} |\nabla \Psi_i(\mathbf{r})|^2 \quad (2.80)$$

is used because it is numerically more stable.

2.3.4 The Mott Insulator problem (DFT + U)

One of the most famous failures of DFT is represented by an entire class of materials known as *Mott insulators* [3, 5, 6].

These systems are characterized by a strong Coulomb repulsion between electrons that stresses them to localize into atomic like orbitals. This phenomenon, known as *Mott localization*, leads to strong correlation effects that can enhance an insulating state even when bands are half filled [5].

All the problems traces back to the XC functional. The LDA and GGA functionals dramatically fail to reproduce the insulating state and other basic properties related to those materials including the equilibrium crystal structure, vibrational spectrum and so on. This is because they are based on metallic like models that tend to delocalize the electronic states.

In principle this problem can be solved via DFT approach by simply finding an adequate E_{xc} , but it is not an easy task. A method proposed to solve this problem is to consider the Hubbard model and the HH (see Equation 2.31) as an implementation to the usual DFT XC functionals. The Hubbard model is, in fact, capable of describing the Mott insulating state in the limit of $U \gg t$. The idea is to describe the strongly correlated electronic states like d or f electrons through an HH like term and the rest of the valence electrons with standard functionals and it is usually called *DFT + U* approximation.

The new functional is

$$E^{DFT+U}[n] = E^{DFT}[n] + E^U[n_i^\sigma] - E^{dc}[n_i^\sigma], \quad (2.81)$$

where $E^{dc}[n_i^\sigma]$ is the *double counting* term. It necessary since the energy contribution of the correlated orbitals is already included in the functional and therefore a correcting term for this double counting must be considered. Usually the $E^{dc}[n_i^\sigma]$ is derived as a mean-field value of the Hubbard term, i.e.

$$E^{dc}[n_i^\sigma] = UN(N-1)/2 \quad (2.82)$$

and the energy functional becomes

$$E^{DFT+U}[n] = E^{DFT}[n] + \frac{U}{2} \sum_{i \neq j} n_i n_j - UN(N-1)/2 \quad (2.83)$$

2.3.5 Spin Density Functional Theory

The DFT described so far does not include the spin contribution to the many body wavefunction and therefore its validity is limited to non spin polarized system. Since we are interested in magnetic materials, the inclusion of spins is mandatory especially for systems in which SOC is significant, as extensively shown in section 2.1. This step marks the transition from DFT to Spin Density Functional Theory (SDFT).

The starting point is the Dirac equation for a one electron system [10]:

$$i\hbar \frac{\partial \Psi(\mathbf{r}, t)}{\partial t} = (c\boldsymbol{\alpha} \cdot \mathbf{p} + \beta mc^2) \Psi(\mathbf{r}, t) \quad (2.84)$$

where $\boldsymbol{\alpha}$, β are 4×4 matrices whose expression is not unique and can be written starting from the Pauli matrices $\boldsymbol{\sigma} = (\sigma_x, \sigma_y, \sigma_z)$ (see Appendix B).

$$\alpha_i = \begin{pmatrix} 0 & \sigma_i \\ \sigma_i & 0 \end{pmatrix}, \quad \beta = \begin{pmatrix} \mathbf{1} & 0 \\ 0 & \mathbf{1} \end{pmatrix}. \quad (2.85)$$

The wavefunction $\Psi(\mathbf{r}, t)$, solution of the Dirac equation, is a four component object called *spinor*

$$\Psi(\mathbf{r}) = \begin{pmatrix} \Psi_\alpha(\mathbf{r}) \\ \Psi_\beta(\mathbf{r}) \end{pmatrix}, \quad (2.86)$$

where α and β represent the spin part of the wavefunction that can assume values $+$ or $-$ (equivalently written as \uparrow, \downarrow)¹

The Dirac equation for a single electron in an electromagnetic field can be written easily by applying the usual substitutions:

$$\boldsymbol{\pi} \rightarrow \mathbf{p} - e\mathbf{A}(\mathbf{r}) \quad E \rightarrow E - e\phi(\mathbf{r}) \quad (2.87)$$

where $\mathbf{A}(\mathbf{r})$ is the *vector potential* and $\phi(\mathbf{r})$ is the *scalar potential*. Equation 2.84 becomes, for the two spinor components

$$i\hbar \frac{\partial \Psi_\alpha(\mathbf{r}, t)}{\partial t} = c\boldsymbol{\sigma} \cdot \boldsymbol{\pi} \Psi_\beta(\mathbf{r}, t) + (mc^2 + e\phi(\mathbf{r})) \Psi_\alpha(\mathbf{r}, t) \quad (2.88)$$

$$i\hbar \frac{\partial \Psi_\beta(\mathbf{r}, t)}{\partial t} = c\boldsymbol{\sigma} \cdot \boldsymbol{\pi} \Psi_\alpha(\mathbf{r}, t) - (mc^2 - e\phi(\mathbf{r})) \Psi_\beta(\mathbf{r}, t) \quad (2.89)$$

where is worth noticing that the vector and scalar potential are chosen with no temporal dependence. This allows to write the wavefunction in the form of $\Psi(\mathbf{r}, t) = \exp(-iEt/\hbar) \Psi(\mathbf{r})$ leading to two solutions for the time-independent Dirac equation

$$c\boldsymbol{\sigma} \cdot \boldsymbol{\pi} \Psi_\beta(\mathbf{r}, t) + (mc^2 + e\phi(\mathbf{r}) - E) \Psi_\alpha(\mathbf{r}, t) = 0 \quad (2.90)$$

$$c\boldsymbol{\sigma} \cdot \boldsymbol{\pi} \Psi_\beta(\mathbf{r}, t) - (E + mc^2 - e\phi(\mathbf{r})) \Psi_\alpha(\mathbf{r}, t) = 0. \quad (2.91)$$

¹The indices α, β for the spinors are not related with the matrices introduced in equation 2.84 i.e. they have a different meaning.

Electrons in atomic orbitals have a ratio $v/c \sim Z\alpha$ where α is the *fine structure constant* and its value is $\sim 1/137$. Therefore it is possible to consider the limit of small v/c and Taylor expand the Hamiltonian terms up to order $(v/c)^2$. The result is

$$H_{Dirac} = \left[\frac{1}{2m_e} (\boldsymbol{\sigma} \cdot \boldsymbol{\pi})(\boldsymbol{\sigma} \cdot \boldsymbol{\pi}) + e\phi(\mathbf{r}) \right] - \frac{p^4}{8m^3c^2} + \frac{\hbar^2 e}{8m^2c^2} \nabla \cdot \nabla \phi(\mathbf{r}) - \frac{\hbar e}{4m^2c^2} \boldsymbol{\sigma} \cdot \left[\boldsymbol{\pi} \times \nabla \phi(\mathbf{r}) \right] \quad (2.92)$$

where the terms are in order the *Pauli Hamiltonian*, *mass-velocity*, *Darwin* and *Spin-Orbit*. Before underlying the main properties of this equation it is worth to rewrite the Pauli term by using the relation

$$(\boldsymbol{\sigma} \cdot \boldsymbol{\pi})(\boldsymbol{\sigma} \cdot \boldsymbol{\pi}) = \boldsymbol{\pi}^2 - \hbar e \boldsymbol{\sigma} \cdot \nabla \times \mathbf{A}(\mathbf{r}) \quad (2.93)$$

that allows to rewrite it as

$$H_{Pauli} = \left[\frac{\boldsymbol{\pi}}{2m} - \frac{\hbar e}{2m} \boldsymbol{\sigma} \cdot \mathbf{B}(\mathbf{r}) + e\phi(\mathbf{r}) \right]. \quad (2.94)$$

It shows that the electron, apart from the magnetic field that is generated by its orbital motion, it has also a "magnetic" moment itself. It is nothing but the spin. Furthermore, the magnetic field generated by its motion that brings to the SOC, this time is intrinsically present in the equation even in the small v/c limit. Last but not least, it is possible to show that $[H, \mathbf{L}] \neq 0$ and $[H, \mathbf{S}] \neq 0$, while $[H, \mathbf{J}] = 0$ as already mentioned in Section 2.2.6.

Now that the framework is known, it is possible to threat the many body problem of interacting electrons with spin. The first step is the Hamiltonian

$$H = \sum_i \left[\frac{\mathbf{p}_i}{2m} - \mu_B \boldsymbol{\sigma}_i \cdot \mathbf{B}(\mathbf{r}_i) + e\phi(\mathbf{r}) \right] + \frac{1}{2} \sum_{ij} \frac{e^2}{|\mathbf{r}_i - \mathbf{r}_j|}. \quad (2.95)$$

Within the SDFT an important operator is the 2×2 *spin density matrix* $n^{\alpha\beta}(\mathbf{r})$ defined as

$$n^{\alpha\beta}(\mathbf{r}) = \sum_i \langle \Psi_{\beta,i} | \mathbf{r} \rangle \langle \mathbf{r} | \Psi_{\alpha,i} \rangle. \quad (2.96)$$

Its importance is related to two basic variables of SDFT: the one electron density $n(\mathbf{r})$ and the magnetization $\mathbf{m}(\mathbf{r})$ through

$$n(\mathbf{r}) = Tr \left[n^{\alpha\beta}(\mathbf{r}) \right] = \sum_{\alpha} n^{\alpha\alpha}(\mathbf{r}) \quad (2.97)$$

$$\mathbf{m}(\mathbf{r}) = \sum_{\alpha,\beta} n^{\alpha\beta}(\mathbf{r}) \cdot \boldsymbol{\sigma}_{\alpha\beta}. \quad (2.98)$$

In the following lines the main results of DFT will be "translated" into the new formalism. The Kohn-Sham density functional becomes

$$E[n^{\alpha\beta}(\mathbf{r})] = T_s[n^{\alpha\beta}(\mathbf{r})] + \frac{1}{2} \int \int \frac{n(\mathbf{r})n(\mathbf{r}')}{|\mathbf{r} - \mathbf{r}'|} d\mathbf{r}d\mathbf{r}' + \sum_{\alpha,\beta} \int V_{ext}^{\alpha\beta}(\mathbf{r})n^{\alpha\beta}(\mathbf{r})d\mathbf{r} + E_{xc}[n^{\alpha\beta}(\mathbf{r})] , \quad (2.99)$$

where

$$T_s[n^{\alpha\beta}(\mathbf{r})] = \sum_{\alpha} \sum_i \langle \Psi_{\alpha,i} | -\frac{1}{2} \nabla^2 | \Psi_{\alpha,i} \rangle . \quad (2.100)$$

As a result, the Khon Sham equations have the following expression

$$\left[-\frac{1}{2} \nabla^2 + \sum_{\beta} V_{eff}^{\alpha\beta}(\mathbf{r}) \right] \phi_j^{\beta}(\mathbf{r}) = \epsilon_j \phi_j^{\alpha}(\mathbf{r}) \quad j = 1, 2, \dots, N , \quad (2.101)$$

with $\phi_j^{\alpha}(\mathbf{r})$ that are the Khon-Sham orbitals that give the correct spin-density matrix, i.e.

$$n^{\alpha\beta}(\mathbf{r}) = \sum_j \phi_j^{\beta*}(\mathbf{r}) \phi_j^{\alpha}(\mathbf{r}) . \quad (2.102)$$

2.4 Practical implementations of DFT

This section is focused on the practical tools necessary for running a DFT self consistent cycle efficiently in real life. It is not a complete guide to practical *ab initio* electronic calculations, but the aim is to underline the main properties and to characterize some specific implementations contained in the Vienna Ab initio Package Simulation (VASP) through which is possible to reduce the computational cost and enhance the efficiency. Furthermore, since this work is focused on magnetic materials with SOC interactions.

2.4.1 Plane Waves

Crystal structures are formed by atoms arranged on tridimensional periodic pattern known as crystal lattice. They can be easily characterized by defining the *Bravais lattice* and the *basis* [7]. One of the most known and fundamental theorems related to the translational invariance in condensed matter is the *Bloch Theorem*.

It states that the electronic wavefunctions can be written as

$$\Psi_{n\mathbf{k}} = u_{n\mathbf{k}}(\mathbf{r})e^{i\mathbf{k}\cdot\mathbf{r}} \quad (2.103)$$

where $u_{n\mathbf{k}}$ has the same periodicity of the lattice.

This allows to write all the cell periodic functions as a sum of plane waves

$$u_{n\mathbf{k}} = \frac{1}{\sqrt{\Omega}} \sum_{\mathbf{G}} C_{\mathbf{G}n\mathbf{k}} e^{i\mathbf{G}\cdot\mathbf{r}} \quad \Psi_{n\mathbf{r}} = \frac{1}{\sqrt{\Omega}} \sum_{\mathbf{G}} C_{\mathbf{G}n\mathbf{k}} e^{i(\mathbf{G}+\mathbf{k})\cdot\mathbf{r}} \quad (2.104)$$

where Ω is the volume of the primitive cell. Using plane waves is convenient for several reasons that can be summarized in *historical*, *practical* and *computational*. The historical reason is related to the fact that the pseudopotential theory [77] was initially created for those functions and, as it will be shown, it is fundamental in the development of *ab initio* DFT codes. The practical reason is related both on the fact that the Hamiltonian can be easily written and on the band structure of many elements that can be described in a free electron picture. Finally the computational reason regards the efficiency of the program that is exceedingly better if one combined plane waves with the Fast Fourier Transform.

2.4.2 The projector augmented-wave method (PAW)

Within the DFT approach, several methods has been proposed for solving the Kohn-Sham equations. Two of those are the *linear augmented-plane wave* and the *pseudopotential scheme*, the former introduced by Andersen and first applied by Koelling and

Arbman [4, 49] while the latter proposed by Hamann, Schluter and Chiang [35, 40]. The pseudopotential method is going to be the starting point of this section.

The ideas behind the pseudopotential method are essentially two: the first is that the core electrons in an atom do not play a significant role in the formation of the chemical bonding and the second is that, in general, the main properties of a material are given by the valence electrons in the region outside the "core sphere". This assumptions allows to ignore the rapidly oscillating part of the electronic wavefunctions near the nucleus that will be very expensive, on a computational level, to be described by plane waves. The real wavefunction is substituted by a "pseudized" one, i.e. by a function that respects the true behaviour outside the core region, while it is smoothly simplified within the same region.

Formally this can be written as

$$\tilde{\phi}(r) = \begin{cases} \sum_i \alpha_i \beta_i(r) & r < r_c \\ \phi(r) & r \geq r_c \end{cases} \quad (2.105)$$

where $\tilde{\phi}(r)$ is the *pseudo wave function*, with the continuity condition imposed when $r = r_c$ (possibly also norm-conserving conditions) and $\phi(r)$ is the true wavefunction. The construction of $\tilde{\phi}(r)$ can be made through different basis sets. The one used in VASP is the *Spherical Bessel-functions* set [1].

The problem of the efficiency related to this method is now shifted to the computational cost of writing the Bessel functions and on the number of those to use in practice. In order to speed up the calculations a slightly different approach was proposed called *Projector Augmented Wave method*. It consists in choosing a local potential V_{loc} and construct a projector $|p\rangle$ such that $\langle p|\tilde{\phi}\rangle = 1$. The All Electron (AE) Hamiltonian will be then factorized into a local and non local part through this projection, leading to a *pseudo* Hamiltonian

$$H_{AE} = \left(-\frac{1}{2m}\nabla^2 + V_{loc} + |p\rangle D \langle p| \right) |\tilde{\phi}\rangle = \epsilon |\tilde{\phi}\rangle \quad (2.106)$$

with

$$D = \langle \tilde{\phi} | \left(\frac{1}{2m}\nabla^2 - V_{loc} + \epsilon \right) | \tilde{\phi} \rangle, \quad (2.107)$$

being ϵ the eigenvalue of the Kohn-Sham equations for the AE system.

The method first introduced by Bloch [11] and improved by Kresse [51, 52] from which the VASP code is based on is the PAW method. It consists in dividing the wavefunction in two parts, the core region is treated in the frozen core approximation, while the AE wavefunction is obtained from the pseudized functions through a transformation:

$$|\Psi_n\rangle = |\tilde{\Psi}_n\rangle + \sum_{lm\epsilon} (|\phi_{lm\epsilon}\rangle - |\tilde{\phi}_{lm\epsilon}\rangle) \langle p_{lm\epsilon} | \tilde{\Psi}_n \rangle \quad (2.108)$$

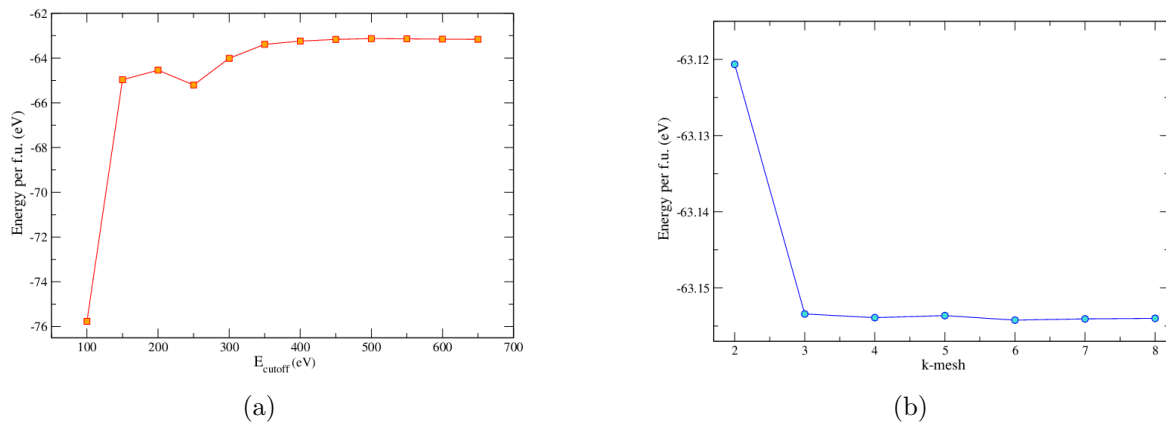


Figure 2.7: E_{cutoff} and k-mesh test for $\text{Ba}_2\text{NaOsO}_6$. In (a) there is the Energy per f.u. as a function of the E_{cutoff} parameter. In (b) there is the energy per f.u. as a function of the k-mesh, the number on the x axis represent the number of k points in each direction ($k \times k \times k$).

where l, m are indices for the angular and magnetic quantum numbers and ϵ is referred to a reference energy. The meaning of such procedure is basically to construct the AE wavefunction by taking the pseudo AE part ($|\tilde{\Psi}_n\rangle$) and, after having subtracted from it the pseudo on-site terms (atomic terms $\sum |\tilde{\phi}_{lm\epsilon}\rangle c_{lm\epsilon}$, substitute them with the AE on site functions $\sum |\phi_{lm\epsilon}\rangle c_{lm\epsilon}$.

These steps lead to a core radius that is smaller, that means a larger basis set of wavefunctions to be used. PAW method is therefore computationally more demanding than the simple pseudopotential one, but it gives better results and allows to describe reasonably the nodes in the core region.

In practice the basis set of plane waves is chosen in order to have completeness, low time consuming iterations and good convergence. As a consequence not every plane wave is used, but only the ones who satisfy the condition

$$\frac{\hbar^2}{2m_e} |\mathbf{G} + \mathbf{k}|^2 < E_{cutoff}. \quad (2.109)$$

The E_{cutoff} limit is one of the parameters that must be tested and tuned before running a calculation since it contributes to reach a certain convergence. This is easy to see from Figure 2.7 (a), where the energy as a function of E_{cutoff} is plotted for $\text{Ba}_2\text{NaOsO}_6$, the energy converges to ~ 0.1 meV for values of $E_{cutoff} \geq 500$ eV. Therefore, for subsequent calculations, the parameter was set to $E_{cutoff} = 600$ eV.

2.4.3 Sampling the Brillouin Zone

The evaluation of many quantities like energy and density requires the integration over the Brillouin Zone (BZ), i.e. over the the Wigner Size cell in the reciprocal space.

The integration of quantities like the energy or the charge density, on a computational level, is done through numerical evaluation of the integrand on a finite set of point called *grid* or *mesh* and through weighted sums on those points in order to obtain an approximation of the integral. A good choice of the integration points and weights is therefore essential when a certain accuracy is required. In this section we will discuss in particular the choice of the set of points necessary for evaluating correctly the properties of materials. In fact, different accuracy is required for different materials, depending on several factors like the type of electronic state, the symmetry and the computational cost.

Before discussing, more specifically, about the integration mesh necessary for insulators and metals, and on how those grids are practically 'build' in VASP, it is mandatory to describe the role of the *special points*. The *Special points* are points in the reciprocal space that have special properties of symmetry and that can be used to reduce the integration grid. Integrals in insulator have the form

$$\bar{f}_i = \frac{1}{N_{\mathbf{k}}} \sum_{\mathbf{k}} f_i(\mathbf{k}) \quad (2.110)$$

with the integrand that is a function of the eigenfunctions $\psi_{i,\mathbf{k}}$ and eigenvalues and is periodic in the reciprocal space. Special points are chosen in order to calculate efficiently those sums.

When it comes to calculate the energy or other quantities, insulators are since they have filled bands that can be integrated by chosing only few good points such as the special ones. For metals the situation is different, in fact the integration for the bands near the Fermi level must be very accurate in order to not lose important informations [7].

Practically, the choice is based on two facts, the first is that there is always a "mean value" point where the integrand equals the integral as demonstrated in the *First mean value theorem for definite integrals*. The second is that one can use the crystal point symmetry to reduce the BZ to an Irreducible Brillouin Zone (IBZ) which is the smallest fraction of the BZ that is sufficient to determine all the informations about the crystal itself.

The method used in VASP is the Monkhorst and Pack [60] because it gives an uniform set of points determined by a simple formula valid for any crystal structure

$$\mathbf{k}_{n_1, n_2, n_3} = \sum_i^3 \frac{2n_i - N_i - 1}{2N_i} \mathbf{b}_i \quad (2.111)$$

where \mathbf{b}_i are the primitive vectors of the reciprocal lattice and $n_i = 1, 2, \dots, N_i$.

The VASP k mesh can be constructed in two ways, it can be centered on the Γ point or shifted arbitrarily. The first choice is always recommended because a Γ centered mesh is almost always more symmetric and computationally less demanding.

The convergence over the k-mesh is a preliminary calculation that allows to understand which set of points can give accurate results. This calculation was done for $\text{Ba}_2\text{NaOsO}_6$ for example and it is graphically shown in Figure 2.7 (b), where the energy is given as a function of the k mesh (k meaning $k \times k \times k$).

It is clear that the energy converges to ~ 0.1 meV for the unit cell used when a grid of $6 \times 6 \times 6$ or greater is used.

2.4.4 Collinear vs Non Collinear systems

Magnetic materials that can be modelled with spins having all the same direction are called *collinear*. When this is not true then it is an example of a *non collinear* system. The main property of the first class of materials is that, from a theoretical point of view, their Hamiltonian can always be diagonalized through a common rotation of all the spins in the spinor basis. The latter case, on the other hand, is a consequence of the SOC, whose effect is to link the spin degrees of freedom to the crystalline ones.

When non collinear magnetic phases are considered and the total energies of the magnetic phases differ in the meV scale, then it should be mandatory to use the SOC contribution and also reduce the symmetry for the calculation purposes, since the coupling between spin and lattice can lower the symmetry of the wavefunctions. Magnetic materials can however show non conventional non collinear configurations usually driven by SOC [55]. In this case it is useful to constrain the direction of the magnetic moments in order to probe the dependence of the energy on the canting angles. This can be done in VASP by applying a penalty energy contribution to the total energy E_0 in the form

$$E_{pe} = \sum_I \lambda \left[\mathbf{M}_I - \hat{\mathbf{M}}_I^0 (\hat{\mathbf{M}}_I^0 \cdot \mathbf{M}_I) \right], \quad (2.112)$$

where I runs over all atomic sites, $\hat{\mathbf{M}}_I^0$ is the direction of the magnetic moments as imposed in the compiled files and \mathbf{M}_I is the integrated magnetic moment for each ion, i.e.

$$\mathbf{M}_I = \int_{\Omega_I} \mathbf{m}(\mathbf{r}) F_I(|\mathbf{r}|) d\mathbf{r}, \quad (2.113)$$

where F_I is a function that goes smoothly to zero as it approaches the boundaries of Ω_I , which is a sphere of radius R_I .

The relevant parameters are R_I and λ in equation 2.112. The former allows a correct integration of the magnetic moments as it defines the radius of the integration sphere if the atoms are considered as hard spheres. It is, consequently, important to define it

correctly in order to have the largest volume for a given atom without letting its sphere overlap with the neighboring ones. The choice made for the subsequent calculations was always to set such parameter at the value of the ionic Wigner-Seitz radius.

The λ parameter, instead, controls the strength of the penalty energy and how much the direction of the magnetic moments is constrained. Its value must be carefully tuned, because, if the penalty energy is too high, it prejudices the accuracy of the results. For the case of $\text{Ba}_2\text{NaOsO}_6$ and $\text{Ba}_2\text{CaOsO}_6$ its value was always lower than 10^{-7} eV for $\lambda = 10$, leading to a "trustful" energy up to 10^{-6} eV.

Chapter 3

Double perovskites $\text{Ba}_2\text{NaOsO}_6$ and $\text{Ba}_2\text{CaOsO}_6$

In this chapter the properties of $\text{Ba}_2\text{NaOsO}_6$ (BNOO from now on) and $\text{Ba}_2\text{CaOsO}_6$ (BCOO from now on) will be discussed.

These are transition metal oxides with a double perovskite structure and rock-salt ordering of B cations [26, 79] and therefore they provide the chance for investigating unconventional electronic interactions and magnetic orders. The general chemical composition of a double perovskite is $A_2BB'O_6$, where A is a large cation while B and B' are typically smaller cations. These double perovskites can show geometric magnetic frustration only when B is a diamagnetic ion and B' is magnetic ion, as these sites are crystallographically distinct and each forms a face-centered cubic sublattice.

The interest regarding these specific double perovskites is not limited to magnetic frustration, since, among the strongly spin-orbit coupled materials, these osmates with $5d^1$ and $5d^2$ electronic configuration, respectively, are also very intriguing for investigating the interplay between SOC, electronic correlation and highly anisotropic interactions that are believed to bring to magnetic ground states driven by quadrupole quadrupole exchange interactions.

More specifically, BNOO is believed to show a canted antiferromagnetic state and local symmetry breaking, while for BCOO experimental studies have shown the presence of an antiferromagnetic phase but, at the state of the art, the specific antiferromagnetic configuration is still unknown.

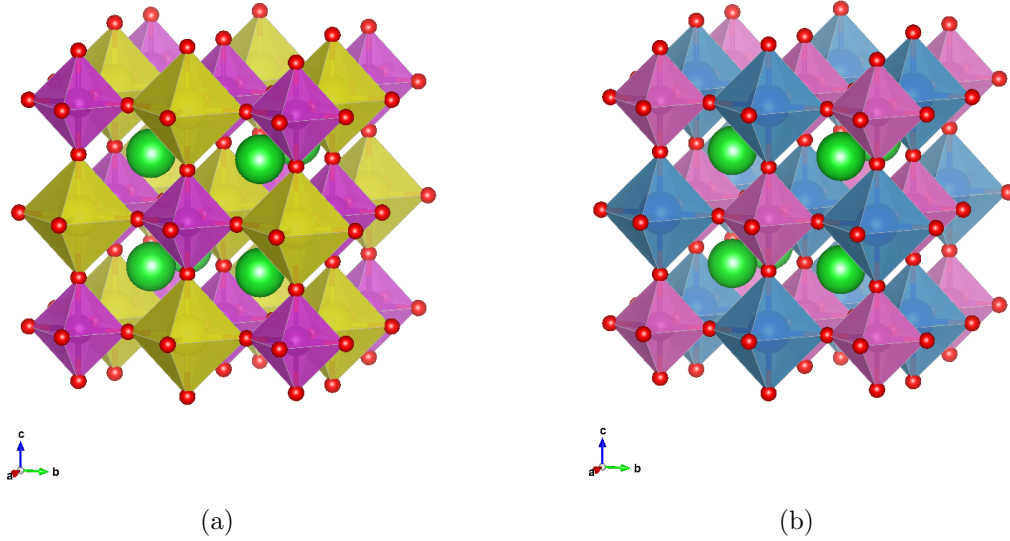


Figure 3.1: Crystallographic structure of BNOO and BCOO. (a) Double perovskite structure of BNOO, where the yellow octahedra and the purple one are centred on Na and Os sites respectively. (b) Double perovskite structure of BCOO, where the blue octahedra and the purple one are centred on Ca and Os sites respectively.

3.1 Physical properties of BNOO

The crystal structure of BNOO is face-centered-cubic (fcc) with space point group $Fm\bar{3}m$ and lattice constant $a = 8.2870(3) \text{ \AA}$, as measured at room temperature [76] and shown in Figure 3.1 (a).

The position of each atom, according to the crystal point symmetry, is listed in Table 3.1 in direct coordinates.

Atom	x	y	z
Ba(1)	1/4	1/4	1/4
Na(1)	1/2	1/2	1/2
Os(1)	0	0	0
O(1)	0.2256(6)	0	0

Table 3.1: Crystallographic positions of atoms in BNOO as obtained via X-ray powder diffraction at room temperature [76].

The measurement of the crystal structure, via X-ray powder diffraction, even at lower temperatures, revealed no structural change [76], but local point symmetry distortions were observed via NMR measurements [57] and will be discussed in more detail in Section 3.1.2.

Furthermore BNOO has attracted interest because it is a rare example of a heptavalent Osmium compound with several unique properties. First of all, since the formal valence of the Os atom is 7+, it corresponds to electronic configuration $5d^1$ so it should be a metal. However both DC resistivity and infrared reflectivity measurements revealed that it is indeed an insulator [26], and from subsequent tight binding analysis it was possible to estimate both the *hopping matrix element* that couples adjacent octahedra t and the Hubbard U associated with moving an electron from the OsO_6 octahedra to its neighbor one. The respective values are $t \sim 0.05$ eV and $U \sim 3.3$ eV [26]. Since $U \gg t$ it was believed to be a Mott insulator. It turned out, from ab initio calculations, that it is instead a Relativistic-Mott insulator [83].

Relativistic-Mott insulators, more commonly named *Dirac-Mott* insulators, are materials in which the metal insulator transition is driven by the combination of SOC and strong correlation effects. The first reported case is Sr_2IrO_4 , where several works have underlined the importance of the J_{eff} splitting, together with the Mott mechanism in the formation of the band gap [8, 47].

Concerning BNOO, Whangbo et al. showed that only by using SOC and on site Coulomb interaction with $U = 2.85$ eV they could open a gap of ~ 0.3 eV along [001] [110] [111] directions proving that it is indeed a Dirac-Mott insulator [83]. But, in their work, they only apply collinear magnetic calculations. We will show in this thesis that we confirm the Dirac-Mott nature of BNOO, but we will further investigate the role of SOC both on the electronic structure and on its magnetic one by using non collinear magnetic and relativistic calculations.

3.1.1 Magnetic properties

Simpler osmium oxides are typically paramagnetic because of the large extent of 5d orbitals, as it is the case of OsO_2 or other simple perovskites like $SrOsO_3$ and $BaOsO_3$ [33, 46, 71].

More complex structures however exhibit a local moment behaviour, including double and triple perovskites La_2NaOsO_6 , Ba_2AOsO_6 ($A = Li, Na$) [75, 76]. From NMR and μ SR measurements [57, 74] was observed that BNOO is a ferromagnet with small magnetic moment of $\sim 0.2\mu_B$ at zero field, with order appearing at $T_C = 6.8K$ as derived from temperature dependence of magnetization and from heat capacity measurements.

By fitting the susceptibility curve with a Curie-Weiss law

$$\chi = \frac{C}{T - \Theta_{CW}} + \chi_0 \quad (3.1)$$

was found a negative Curie-Weiss temperature $\Theta_{CW} = -10, -10$ and -30 K along $[100]$, $[111]$, $[110]$ with effective magnetic moments $\mu_{eff} = 0.602, 0.596$ and $0.647 \mu_B$ respectively [26].

This result is an evidence of an antiferromagnetic coupling, which however was not observed experimentally. It is also worth noticing that the isostructural, isovalent and Mott insulating Ba_2LiOsO_6 (BLOO) orders antiferromagnetically, in spite of a very similar Curie-Weiss susceptibility [74] and similar volume. Finally, as pointed out in several papers [29, 83], the $[110]$ direction is found to be the easy axis, in contrast with the Landau theory of ferromagnetism, that predicts easy axis parallel to the $[100]$ direction.

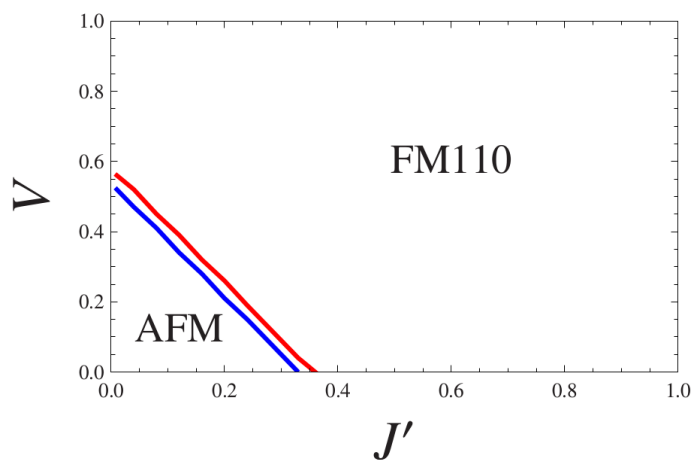


Figure 3.2: Mean field phase diagram for BNOO in cubic symmetry at $T=0$. Two phases are suggested: AFM denotes a conventional antiferromagnetic ground state while FM110 denotes a two sublattice canted antiferromagnetic state with easy axis oriented along $[110]$ direction. The J' and V represent the antiferromagnetic and the quadrupolar exchange couplings in the Hubbard model picture. They are rescaled with respect to the ferromagnetic exchange coupling J , which is set $J = 1$.

However, when taking into account the strong SOC effect, together with a quadrupolar interaction, it turns out that other unconventional magnetic states are possible, as proposed by Chen et. al. [20]. The phase diagram extracted from their mean field analysis is plotted in Figure 3.2. It shows two possible magnetic configurations: AFM and FM. The first is a collinear AFM state i.e. with magnetic wavefunctions perfectly orientated along the same crystallographic axis, but pointing in opposite directions. The latter is a non-collinear canted FM state and it will be discussed in more detail in the next Section. The transition between the two can be achieved depending on the relative strength of three parameters: J , J' and V . J is the ferromagnetic exchange coupling con-

stant, J' is the antiferromagnetic one and V is the quadrupolar potential contribution. In the plot they are rescaled such that $J = 1$.

3.1.2 Local symmetry breaking and canted ferromagnetism

The issues regarding BNOO are not limited to its electronic and magnetic properties, but they are extended to its local structure as well. In fact, so far, the local symmetry of the NaO_6 octahedra has not been considered and it is known that, several distortions can appear [8, 55]. The first experimental studies were done by using X-ray powder diffraction which is not capable of investigating the local configuration of the O atoms since they have a very low scattering power.

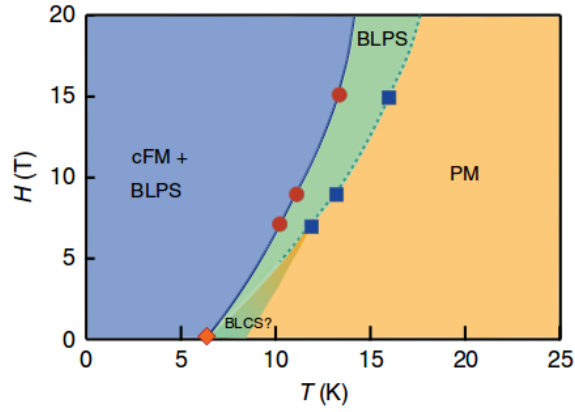
A turning point, was the study of L. Lu et al. [57], that revealed, via NMR measurements, the presence of a local point group symmetry breaking that slightly precedes the magnetic phase transition (see Figure 3.3 (a)) whose proof is given by the shift of the transition temperature with increasing intensity of the applied magnetic field.

In Figure 3.3 (b) there is the experimental evidence of the phase transition given by the splitting of the ^{23}Na spectral lines in triplets when a field of 9 T is applied along the [001] crystalline axis.

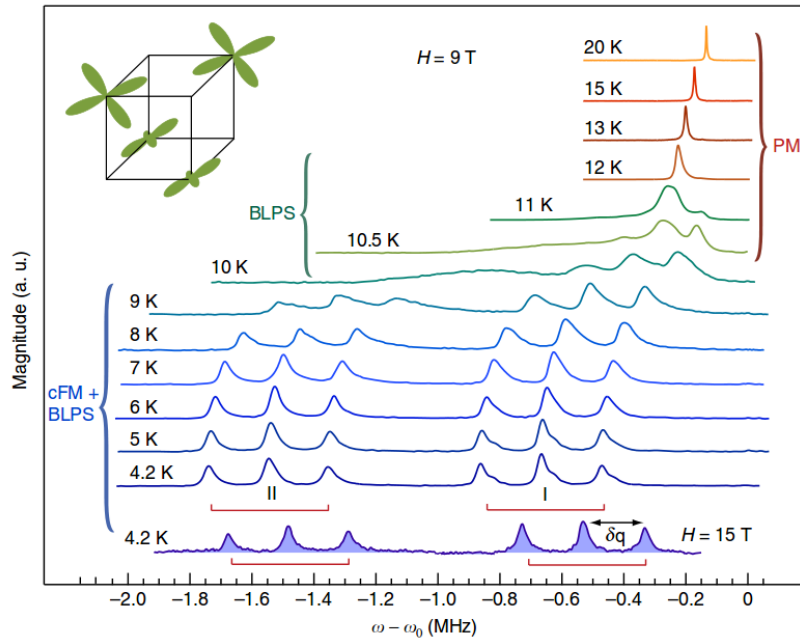
The origin of these splitting is due to two effects: *magnetism* and *electric field gradient* (EFG). The first is responsible for the two groups denoted as I, II in Figure 3.3 (b) and is indicative of a different magnetic field felt by the Na atoms.

The experimental analysis is consistent with a *canted ferromagnetic* state with two sublattices. These sublattices are the xy parallel planes along the [001] direction, and, from the definition of sublattice itself, they are the planes where all the spins have the same alignment. Between spins on parallel planes the canting angle (defined in Figure 3.4 (b)) is $\phi \approx 67^\circ$ and it gives a net and low ferromagnetic moment ($\mu \approx 0.6\mu_B$) along the [110] direction in agreement with previous studies. A graphical representation of the magnetic state can be found in Figure 3.4 (a).

The EFG is instead responsible for the splitting in triplets of the I and II peaks, whose width are labelled as δq in Figure 3.3 (b) and originates from quadrupole interaction that brings to a change in the local charge distribution, or in other words, to a break of the local point symmetry. In the field of NMR, *the quadrupole effect* is an effect observed when there is an interaction between the nonspherical charge distribution and an electrostatic field external to the nucleus, and its strength is related to the product of the nuclear quadrupole moments and the magnitude of the EFG. In nuclei with spin $I > 1/2$ the quadrupole moment is nonzero, while the EFG is nonvanishing only if the local symmetry is lower than cubic. Therefore such splitting is a clear evidence of a symmetry breaking from cubic to lower ones.

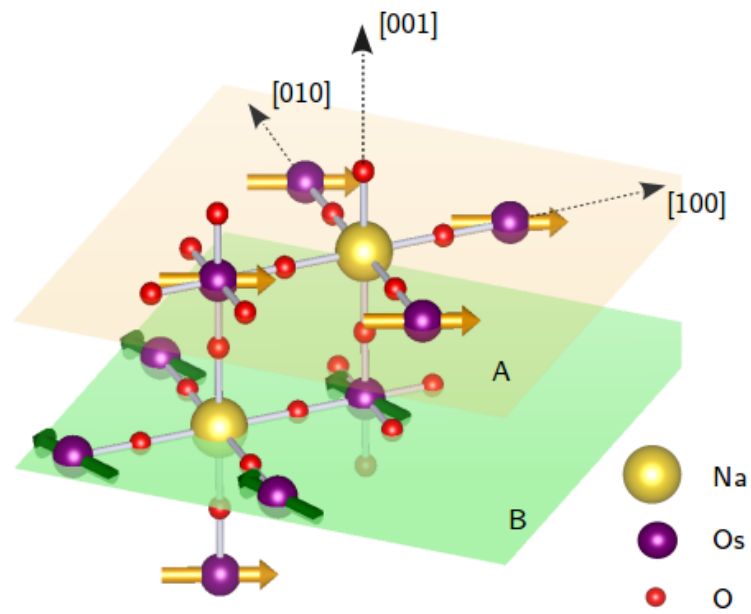


(a)

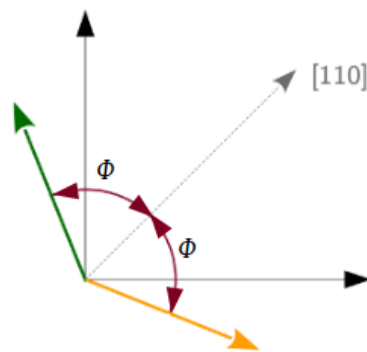


(b)

Figure 3.3: Sketch of the phase diagram of BNOO from NMR measurements. The circles are the T_c transition temperatures from paramagnetic to canted antiferromagnetic state from NMR. The diamonds are the T_c transition temperatures from paramagnetic to canted antiferromagnetic state from thermodynamic measurements.



(a)



(b)

Figure 3.4: Canting angles between spins in the two sublattice magnetic order of BNOO. (a) Graphical description of the magnetic order in BNOO, (b) Reference frame used for describing the canting angles ϕ [57].

In another paper [56] W.Liu et al. investigated via computed models the EFG in the point charge approximation and estimated which kind of distortion of the Na-O octahedra could bring to the δq splitting observed experimentally.

The possible distortions that agree with the experimental results are:

- Identical *compression* of all the Na octahedra, with O atoms that can move independently, but symmetrically about the central Na site as in Figure 3.5 (a). This model will be addressed as model A from now on.

A notation for the bonds is necessary to be introduced. When talking about any bond α , the letters a, b, c will mean the α bond along x, y, z respectively, as in the reference frame of Figure 3.5 (b). Therefore also the $(x\ y)$ plane is equivalent to the $(a\ b)$ plane and so on.

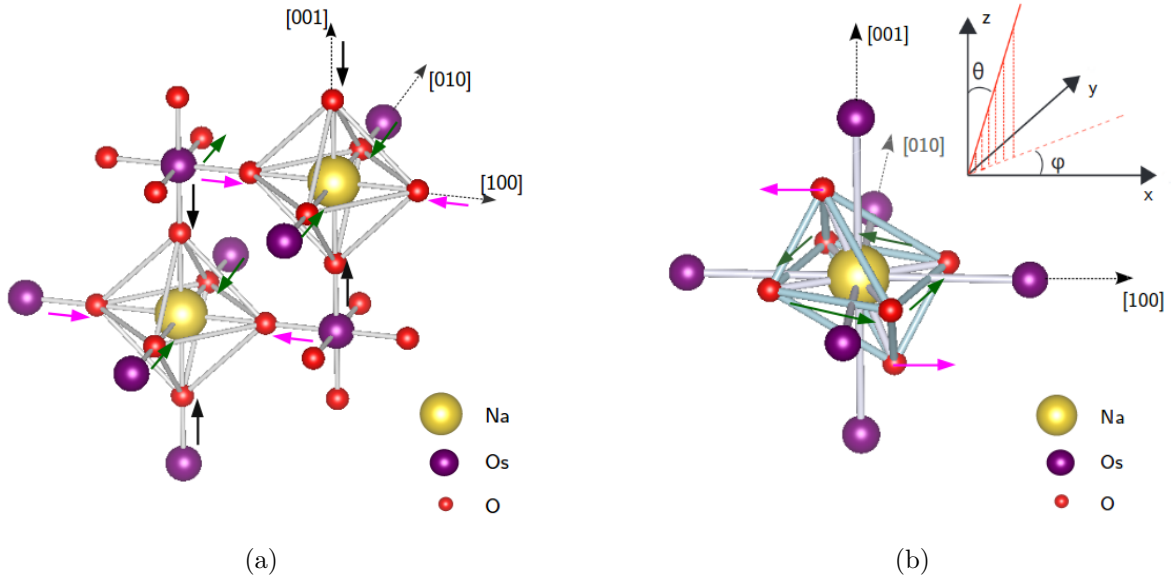


Figure 3.5: Suggested distortions of the Na octahedra in BNOO. (a) **Model A:** Identical compression (or expansion) of the Na-O octahedra with respect to the principal axis. (b) **Model E:** Identical rotational distortion in the (x,y) plane and tilting in the (x,z) plane.

The relative compressions of the a, b, c , Na-O bondlengths from the experimental value of 2.274 \AA for model A are

δ_a	δ_b	δ_c
-0.65 %	-0.25 %	-0.1 %

- Identical *expansion* of all the Na octahedra, with O atoms that can move independently, but symmetrically about the central Na site as in Figure 3.5 (a), but with reverted arrows. This is still in the model A group.

The relative expansions of the a, b, c Na-O bondlengths from the experimental value of 2.274 Å are

δ_a	δ_b	δ_c
+ 0.55 %	+ 0.1 %	+ 0.2 %

- Identical rotational distortion of all the Na octahedra in the (a,b) plane together with a tilt distortion in the (a,c) plane, with distortion angles θ and ϕ as in Figure 3.5 (b). This model will be addressed ad model E.

The suggested values are $\theta = 8.7^\circ$ and $\phi = 12^\circ$.

It is important to underline that local symmetry, in SOC materials, is intrinsically related to the magnetic properties as well since the effect of the relativistic interaction is to couple the spin degrees of freedom with the lattice ones.

3.2 Physical properties of BCOO

The crystal structure of the double perovkite BCOO is face-centered-cubic (fcc) with space point group $Fm\bar{3}m$ and lattice constant $a = 8.3619(6)$ Å at room temperature ($a = 8.3462(7)$ Å at 3.5 K) [84].

The position of each atom, according to the crystal point symmetry, is listed in Table 3.2 [84] in direct coordinates.

Atom	x	y	z
Ba(1)	1/4	1/4	1/4
Ca(1)	1/2	1/2	1/2
Os(1)	0	0	0
O(1)	0.2294(23)	0	0
	[0.22911(16)]		

Table 3.2: Crystallographic positions of atoms in BCOO as obtained via X-ray powder diffraction at 280 K, together with the refinements obtained from neutrons only at 3.5 K, reported in square brackets [84].

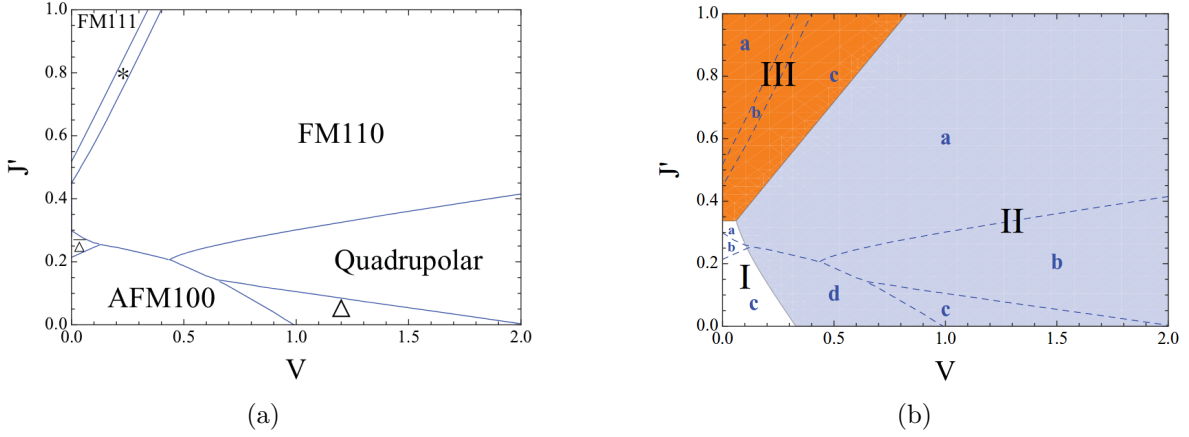


Figure 3.6: Magnetic phase diagrams of BCOO [19]. (a) Magnetic phase diagram at $T = 0$ K. (b) Phase diagram at $T > 0$ K.

3.2.1 Magnetic properties

The d.c. susceptibility measurements [84] highlighted a Curie Weiss behaviour for $T > 100$ K and a long range magnetic order for $T < T_C = 50$ K, consistent also with muon spin rotation and heat capacity measurements [79]. The Curie Weiss temperature is found to be $\Theta_{CW} = -156.2(3)$ K.

Since the oxidation state of Os in BCOO is Os^{+6} , one would expect a spin only value of the $5d^2$ orbital $S = 1$, but the estimated ordered moment is around $0.2\mu_B$. This low magnetic moment implies a strong influence of SOC, as in BNOO.

From a teoretical point of view, a recent study [19] proposed a phase diagram(see Figure 3.6 (a)) at $T = 0$ K with seven potential ground states. The possible suggested ground states can be grouped in three categories: *antiferromagnetic*, *ferromagnetic* and *quadrupolar*.

Among the ferromagnetic states, the FM110 is a two sublattice ferromagnetic order as already seen for BNOO, as well as the intermediate "*/", while FM111 is a pure ferromagnetic state. Among the antiferromagnetic states, Δ and $\bar{\Delta}$ are a more complex 4 sublattices antiferromagnetic orders, not well understood yet, while the AFM100 is a simple antiferromagnetic orientation. Finally. the quadrupolar state is found to break the time reversal symmetry with a two sublattice structure and spin nematic phase.

The antiferromagnetic order found experimentally seems to restricts to three AFM states the possible magnetic order, but one can make light by considering the phase transition to those states from the $T = 0$ to the $T > 0$ phase diagram of Figure 3.6 (b) where all the previous magnetic states are labelled via letters. Muon spin rotation experiment, in fact, showed a continous phase transition, which, depending of the regions I, II, III is adressed to different magnetic states [79].

More precisely the continuous transitions in region I is from the paramagnetic to the four sublattice $\bar{\Delta}$ phase. In region II, at mean field level, the transition from the paramagnetic to the quadrupolar phase is continuous as well as the transitions from the quadrupolar to low temperature phases like FM110 and Δ . Finally in region III the transition from paramagnetic to FM111 and from the latter to FM110 and * are all continuous. All the others are of the first order.

Should be clear that the properties of BCOO are not yet well understood, as demonstrated, for example, from the fact that no studies are available on the local point symmetry. It is also not clear the strength and role of the Hubbard U as well as of SOC, all "ingredients" that make this material a forefront in research.

Chapter 4

Results

*This chapter is focused on the results obtained via *ab initio* calculations for BNOO and BCOO. The procedure used for calculations is outlined step by step as well as the theoretical derivations.*

What we find is that BNOO has a structure that is locally distorted in his ground state, in accordance with Model A (see Section 3.1). The distortion is driven by SOC since it can be observed only by including the relativistic interaction in the DFT + U scheme. We also agree with the Dirac-Mott description of the material since we show that the band gap can be opened only by including SOC. Furthermore, we find that the canting angle observed experimentally competes with another stronger "ferromagnetic" one and that such competition is strongly dependent on the electron correlation as well as on local distortions. For values of $U - J$ sufficiently large, the total energy has a global minima in correspondence of the experimental canting angle. Its overcome, with respect to the other minimum, can be addressed interactions of higher order than dipolar, especially to octupolar ones. This result is obtained by mapping the total energies onto a Pseudospin Hamiltonian in a fashion similar to the mean field Spin Hamiltonian, that can be written as a sum of multipolar tensor products. Concerning BCOO, we find that it is also a Dirac-Mott insulator with local symmetry breaking analogous to the Model A used for describing BNOO. Its magnetic ground state turns out to be a two sublattice collinear antiferromagnetic state with magnetic moments aligned along the $[110]$ direction.

4.1 Distortions in BNOO

The first step that is necessary for characterizing the material is to understand the role of the local point symmetry, as described in Section 3.1.2, so we focused our attention on the two models A and E.

The unitary cell used for calculations is a cell of $a/\sqrt{2} \times a/\sqrt{2} \times a$ ($5.85979 \times 5.85979 \times 8.287 \text{ \AA}^3$), together with a k mesh of $6 \times 6 \times 6$ and an energy cutoff $E_{cutoff} = 600 \text{ eV}$ with high accuracy of $\sim 10^{-8} \text{ eV}$. This setup was used for all the calculations regarding BNOO.

In order to fully understand the origin of the distortions, several approaches were used with fixed experimental lattice constant and fixed positions of Na, Ba, Os atoms, while the oxygens were allowed to relax freely to the optimal position depending on the specific task. A quasi-Newton (or variable metric) algorithm was used to relax the ions into their instantaneous groundstate through the use of forces and stress tensor that allow to find the directions along which there is the equilibrium position.¹

The calculations done were:

Relaxation with LDA : In this case all the O atoms were allowed to relax to their optimal configuration, but no magnetic moments were initialized and the material was therefore considered as paramagnetic. This surely brought to a bias in the characterization since it is known that the Mott insulating state appears from the contribution of on site Coulomb interaction and, in fact, in this case, BNOO is a metal. The importance of this method consists in probing if the distortions can be driven simply by electrostatic interactions, or from the magnetic ones.

No symmetry breaking was observed.

Complete relaxation with LDA + U : Also in this case all the O atoms were relaxed, but an LDA + U approach was used. The chosen value of $U_{eff} = U - J$ was 3.0 eV and also magnetism was included with magnetic moments that could freely relax to their ground state orientation.

No symmetry breaking was observed.

Relaxation with LDA + U + SOC : In this case we implemented the input files by including the SOC effect. The chosen value of $U_{eff} = U - J$ was 3.0 eV and also magnetism was included with magnetic moments constrained along the suggested experimental direction (see Figure 3.4 (b)).

We find in this case a local symmetry breaking, with the a, b, c Na-O bonds having different lengths (see Table 4.1), but keeping the symmetry with respect to the Na atom. This local point symmetry is consistent with Model A with compression.

¹The flags used in VASP can be found in Appendix B under the note: Relaxation

δ_a	δ_b	δ_c
-1.6 %	-0.9 %	-1.0 %

Table 4.1: **Bondlength distortions of BNOO (1)** The $\delta_a, \delta_b, \delta_c$ are the relative distortions of the a, b, c bonds compared to the experimental value of 2.274 Å.

Constrained relaxation of model A with LDA + U + SOC : The approach used in this case was the same of the previous point, but a more precise strategy for probing uniform compressions and distortions was obtained by fixing the length of the Na-O c bond and allowing the other oxygens in the (a, b) plane to relax freely. The c bondlength was then changed in steps of 0.01 Å from $c = 2.14$ Å to $c = 2.40$ Å and then in steps of 0.001 Å near the minima.

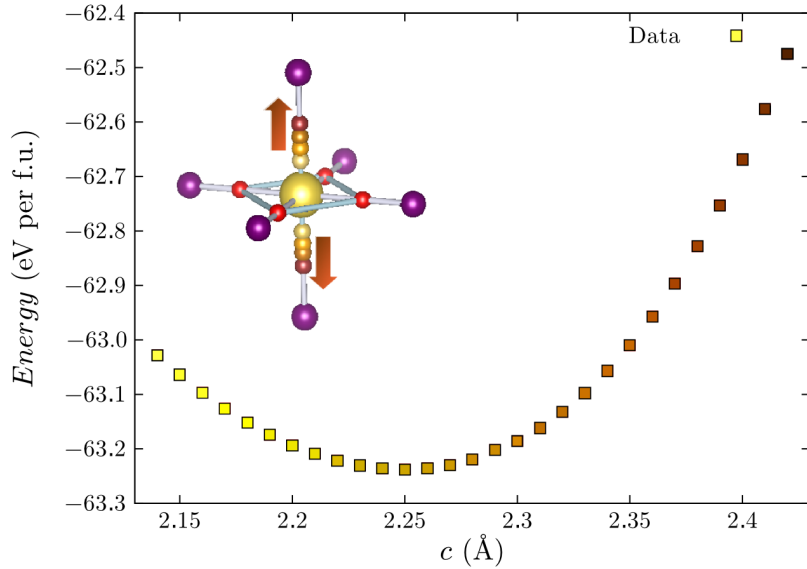


Figure 4.1: Energy dependence of BNOO on Na-O c bondlength.

In the inset there is a graphical representation of the steps made for this ionic relaxation. The shaded brown spheres are the fixed oxygen atoms, while the red shares are the free oxygens. Every shade of brown is referred to a separate calculation.

The *induced* local symmetry breaking shows only one minima with the bonds in the (a, b) plane that agree with the symmetry proposed in model A. The minima is found at $c = 2.250$ Å and reveals a tendency of the Na octahedra to compress (see Figure 4.1 and Table 4.2). With this method it was possible also to investigate the dependence of the other bondlengths from the c one (see Appendix C).

δ_a	δ_b	δ_c
-1.6 %	-0.9 %	-1.0 %

Table 4.2: **Bondlengths distortions of BNOO (2)** The $\delta_a, \delta_b, \delta_c$ are the relative distortions of the a, b, c bonds compared to the experimental value of 2.274 Å.

Constrained relaxation of model E with LDA + U + SOC : The method used in this case is the same as the previous one, but a more precise strategy for probing rotational distortion together with the tilting angle, i.e. Model E, was obtained by fixing the positions of the O atoms in slightly tilted configurations (see Figure 4.2), while allowing the other oxygens to move. The tilting angle θ was then changed manually in steps of 3° from $\theta = 3^\circ$ to $\theta = 15^\circ$. The Na-O c bondlength was set as the experimental one.

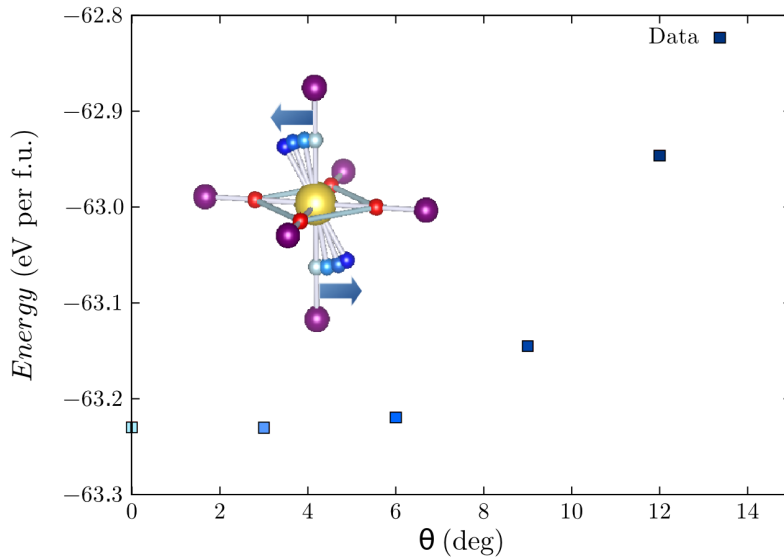


Figure 4.2: Energy dependence of BNOO on θ tilting angle. In the inset there is a graphical representation of the steps made for this ionic relaxation. The shaded blue spheres are the fixed oxygen atoms, while the red spheres are the free oxygens. Every shade of blue is referred to a separate calculation.

The *induced* local symmetry breaking leads to a different structure, with the Na octahedra that are rigidly tilted with the constrained values of θ and $\phi = 0$. This is exactly like the model F in [56] and does not coincide with the expected model. Furthermore, the energy decreases quadratically (in absolute value) as the angle

increases (see Figure 4.2) and its minimum is in correspondence of $\theta = 0^\circ$, which is exactly the undistorted structure with experimental c bondlength.

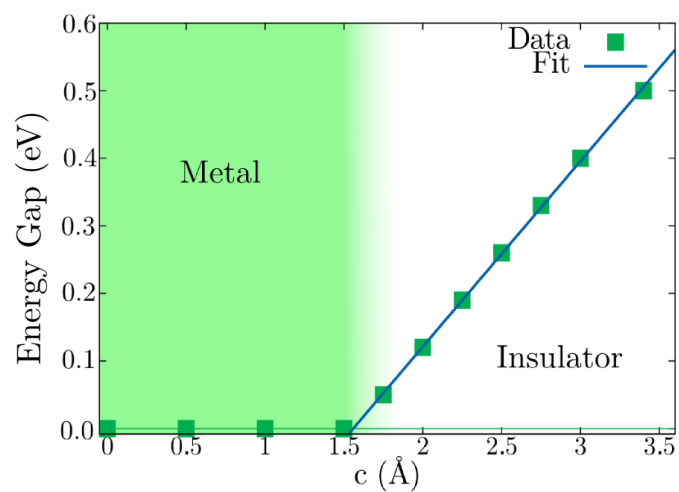
4.2 Bandstructure, DOS and effective U for BNOO

The bandstructure and the Density of States (DOS) were calculated within the LDA, LDA + U and the fully relativistic LDA + U + SOC method with canted magnetic moments. The investigation of the differences between such approaches is important for discerning the origin of the insulating state of BNOO.

What we find is that in both LDA and LDA + U calculations BNOO is a metal (see Figure 4.4 (a), (b)), even though the influence of U is evident from the fact that it almost splits the bands in correspondence of the Fermi energy². Only when SOC is included, BNOO becomes insulator, with an energy gap of ~ 0.5 eV when $U - J = U_{eff} = 3.4$ eV (see Figure 4.5 (a)). This proves the Dirac Mott insulating nature of BNOO, i.e. the strong importance of SOC for the metal insulator transition typical of Mott materials. The metal-insulator transition was investigated from first principles by tuning the U_{eff} parameter in the input file in the range of $[0, 3.4]$ eV within the LDA + U + SOC scheme with constrained magnetic moments and by measuring the energy gap for each value. The result is the phase diagram of Figure 4.3 where is shown (in green) the region where BNOO is a metal, i.e. when U_{eff} is too low for localizing the Os electronic wavefunctions in a way that the insulating state can be reached. The gap begins to open when $U_{eff} \sim 1.5$ eV and its value increases linearly as can be seen from the fit.

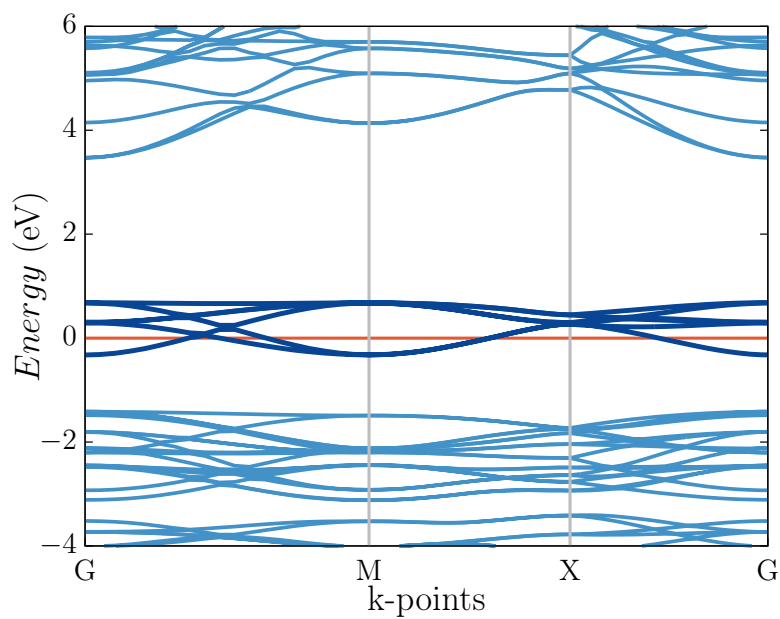
The on site Hubbard U, or, more precisely, the U-J value, will be very significant also for stabilizing a certain magnetic configuration; therefore it was further studied with a method implemented in VASP that is based on the Random Phase Approximation and is called *constrained Random Phase Approximation* (cRPA) [36, 37]. The cRPA calculation allows to do a Wannier projection of some selected bands in order to calculate the polarizability and, in the end, the Hubbard U for those selected bands. Attention must be paid on the fact that this type of calculation is done within the LDA approach, i.e. when the system is metallic. The selected bands are the blue ones of Figure 4.4 (a), i.e. the t_{2g} ones. The result obtained is $U_{eff} \approx 2.8$ eV. This result is, however, in contrast with our subsequent calculations and estimations of the U_{eff} parameter and this is addressed mainly to the strong hybridization of the osmium d bands with the oxygen p ones (see Figure C.2 in Appendix C) which is strong enough to prevent from a correct Wannierization of the t_{2g} states. This problem could be solved by considering, in the Wannier projection, also the low lying states but it is a very demanding task and further studies are needed.

²The plots of the DOS are in Appendix C.

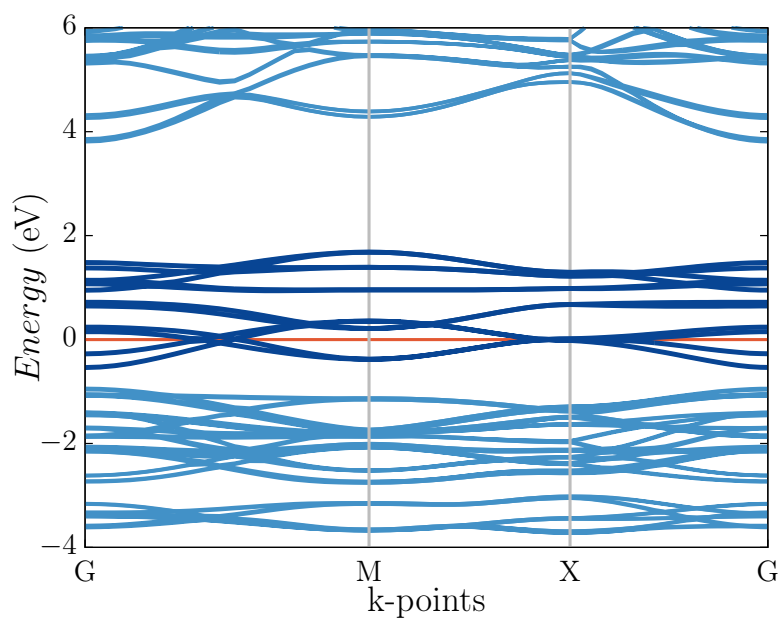


(a)

Figure 4.3: Dependence of the energy gap from U (BNOO). The metal-insulator phase diagram of BNOO is shown as studied from first principles calculations. The green part shows the metallic state and the purple line is the curve obtained with a linear fit.

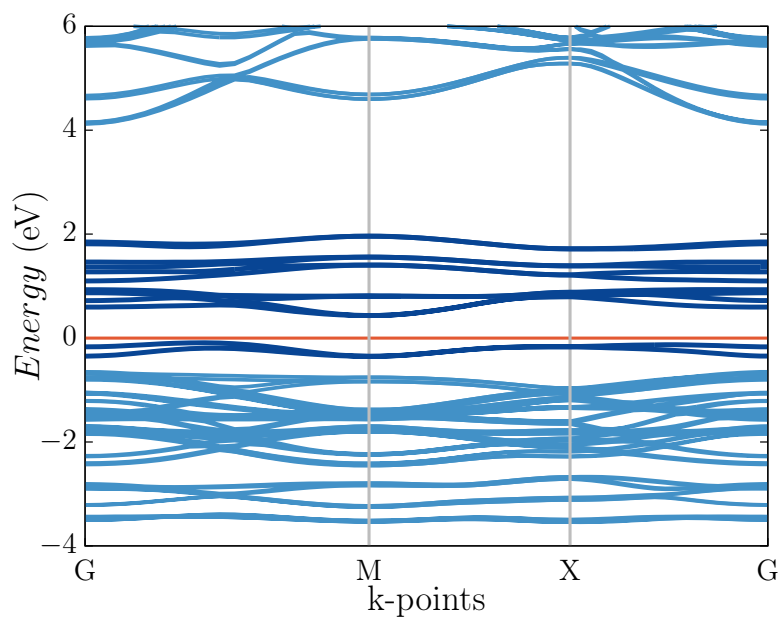


(a)

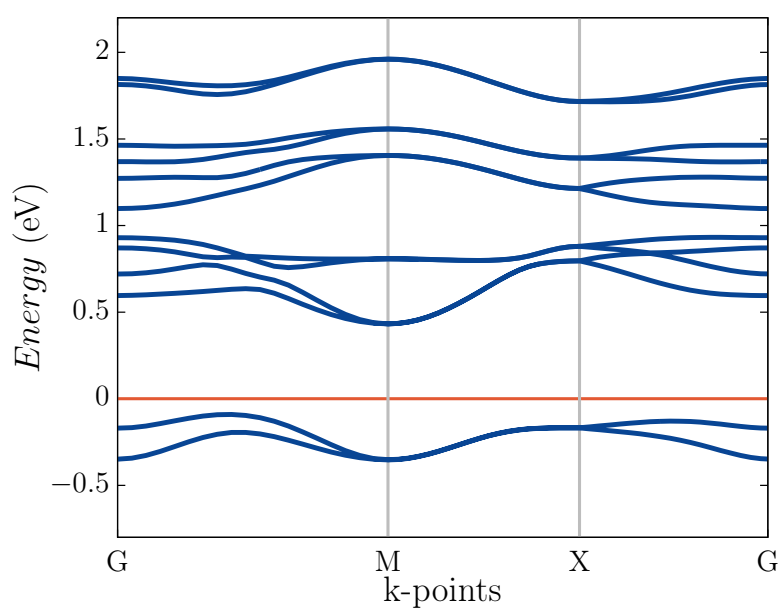


(b)

Figure 4.4: Bandstructure of BNOO with LDA and LDA + U. (a) Bandstructure of BNOO obtained within the LDA scheme. (b) Bandstructure of BNOO obtained with the LDA + U scheme with $U_{eff} = 3.4$ eV.



(a)



(b)

Figure 4.5: Bandstructure of BNOO with LDA + U + SOC. (a) Bandstructure of BNOO calculated within the LDA + U + SOC approach with $U_{eff} = 3.4$ eV. (b) Zoom of the bands near the Fermi energy.

4.3 Magnetic ground state of BNOO

The calculations of the magnetic ground state were computationally very demanding. The unit cell used was the same as before, but with bondlengths optimized with the VASP relaxation scheme.

The sequence that will be used for presenting the results follows the theoretical procedure used. It has the advantage of allowing the storyline to cover more problems together with their solutions. As first step, the nearest neighbour exchange coupling was calculated. This was done because the simplest model Hamiltonian that can be used for magnetic materials is a Heisenberg like Hamiltonian. Very often such model is sufficient for the estimation of magnetic interactions and is enough for a complete description of magnetic materials.

The exchange coupling constant for nearest neighbour could be derived by single calculations with different magnetic configurations. The configurations chosen were an AFM 110 and FM 110 with differences in energies in Table 4.3.

	Energy per f.u. (eV)
FM	- 63.23656
AFM	- 63.23581

Table 4.3: Energy of FM 110 and AFM 110 configurations for BNOO

By writing a simple Heisenberg Hamiltonian:

$$\mathcal{H} = E_0 + J \sum_{\langle ij \rangle} \mathbf{S}_i \cdot \mathbf{S}_j \quad (4.1)$$

for the two configurations, the respective energies in terms of the constants E_0 and J are:

$$E_{AFM} = E_0 - 4JS^2 \quad (4.2)$$

$$E_{FM} = E_0 + 12JS^2 \quad (4.3)$$

from which $JS^2 = (E_{FM} - E_{AFM})/16 \sim 0.5$ meV.

But the suggested magnetic ground state is a canted antiferromagnetic phase. In order to investigate such configuration, we did an LDA + U + SOC calculation with $U_{eff} = 3.0$ eV and with constrained magnetic moments which were constrained along different directions in a sequence of calculations. More specifically, we started from a FM 110 configuration ($\phi = 0$ in Figure 3.4 (b)) and then we slightly changed the canting

angle in steps of 2.5° ending in the AFM 110 phase. This can be done in VASP by using flags like `L_CONSTRAINED_M`, `RWIGS` and `LAMBDA` (see Appendix A), the last one being the λ parameter already described in Section 2.4.4. The calculation was set with a very high precision of 10^{-8} eV.

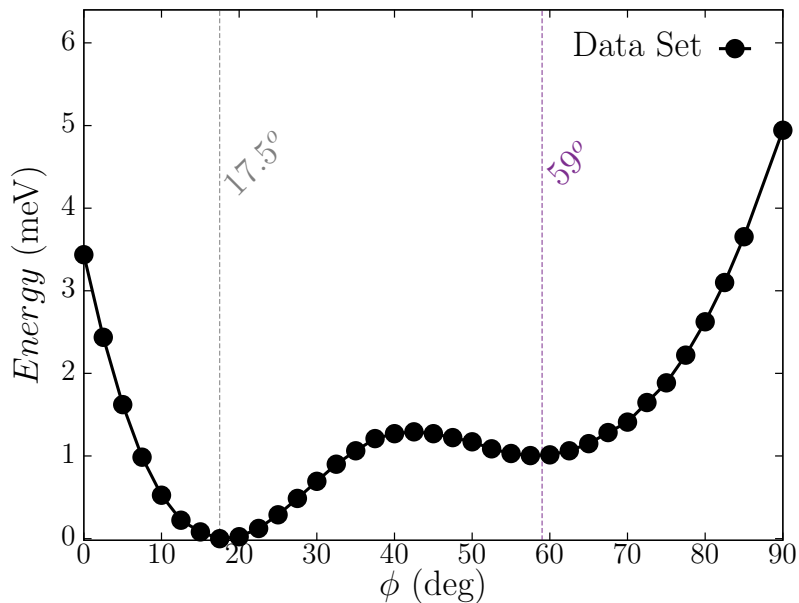


Figure 4.6: Energy as a function of ϕ for BNOO. The circle points represent the computational values of the energy as calculated with the LDA + U + SOC approach with $U_{eff} = 3.0$ eV. The grey dotted line identifies the minimum at 17.5° , while the purple dotted one identifies the minimum at 59° .

The result is the curve in Figure 4.6. It shows the appearance of two minima. The first is at $\phi = \phi_1 \sim 17.5^\circ$ and is a global minimum, while the second is at $\phi = \phi_2 \sim 59^\circ$. From the integration over the Wigner Size radius of the Osmium atom, the total magnetization could be evaluated together with the magnetic moment of the Osmium atom (see Table 4.4). It is worth noticing that the global minimum is not compatible with the experimental one, and it leads to a canted *ferromagnetic* phase, i.e. to a system that is strongly ferromagnetic. Regarding this topic the nomenclature in literature is not univoque, so we will refer to a *canted antiferromagnetic* phase if the angle ϕ is grater than 45° , i.e. when the system is more antiferromagnetic and we will use the term *canted ferromagnetic* if ϕ is lower than 45° .

The result obtained already vanishes the idea of using an Heisenberg Hamiltonian for modelling the magnetic ground state since it cannot account for non collinear systems.

Minima	Magnetization [110]	Os mag mom
ϕ_1	$\sim 0.95 \mu_B$	$\sim 0.8 \mu_B$
ϕ_2	$\sim 0.35 \mu_B$	$\sim 0.7 \mu_B$

Table 4.4: Magnetization and Os magnetic moment in BNOO with $U_{eff} = 3.0$ eV

A Spin Hamiltonian approach was tried and will be discussed in more detail in the following Section, but it also fails to reproduce correctly the results. The origin of the canted magnetic system can be found only in higher order interactions of four and six spins, which can be modelled through a multipolar Hamiltonian (see Section 2.2.6).

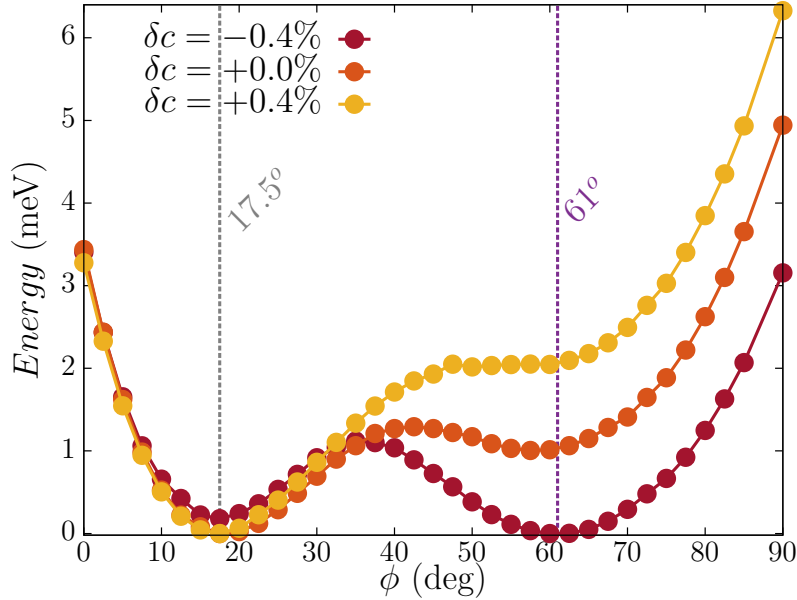


Figure 4.7: Energy as a function of ϕ with distortions for BNOO.

The circle points represent the computational values of the energy as calculated with the LDA + U + SOC approach with $U_{eff} = 3.0$ eV. The three curves are for distortions of the c bondlength $\delta_c = 0, \pm 0.4\%$ and the energies are arbitrarily shifted in order to have the 0 of the energy in correspondence of the global minimum. The grey dotted line identifies the minimum at 17.5° , while the purple dotted one identifies the minimum at 61° .

A natural question that one can ask regarding BNOO is if the local point symmetry can play a role in the formation of the canted ferromagnetism. The answer could be found by repeating the calculation of the energy curve as a function of the canting angle

for two different structures with slightly larger and lower values of the c bondlength with respect to the optimal value obtained within the constrained Model A approach and the LDA + U + SOC scheme. The values of the c bondlength chosen are $c = 2.240 \text{ \AA}$ ($\delta c = -0.4\%$) and $c = 2.260 \text{ \AA}$ ($\delta c = +0.4\%$). The curve was calculated within the LDA + U + SOC scheme with $U_{eff} = 3.0 \text{ eV}$ and the result is in Figure 4.7.

What is found is remarkable since it shows that the energy of the minima depend on the displacement of the atoms in a non trivial way. An expansion tends to vanish the local minimum ϕ_2 while a further compression leads to the overcome of the same minimum over the one at ϕ_1 . It is also very important because ϕ_2 is in good agreement with the experiment and therefore it is thought to be the true minimum and the true magnetic state, especially if further calculations can somehow prove that what was found here is not a mere quantum fluctuation.

Two more considerations can be made on this part. The first regards the value of ϕ_2 that is slightly different when the further-compressed octahedra is considered; in particular it changes from $\phi_2 \approx 59^\circ$ to $\phi_2 \approx 61^\circ$. The second consideration is about the total energy values of the "canting curves". In fact, since the value of the U_{eff} chosen is constant, the total energies are comparable even though the "canting curves" in Figure 4.7 were arbitrarily rescaled. It turns out that the ones calculated with $\delta c = \pm 0.4 \%$ have a global minimum that is higher in energy with respect to the one with $\delta c = 0 \%$ (see Table 4.5).

c bondlength (\AA)	δc (%)	ΔE (meV)
2.240	- 0.4	+ 4.62
2.250	0.0	0
2.260	+ 0.4	+ 3.02

Table 4.5: Magnetization of BNOO with $U = 3.0 \text{ eV}$

The dependence of the magnetic phase on the distance between atoms can be thought as a result of a different potential felt by the electrons responsible of the superexchange coupling. But, as it was shown in Section 2.2.3, the superexchange coupling can be modelled through an Hubbard Hamiltonian in which, apart from the hopping term, also an on site Coulomb interaction is present. Therefore it is reasonable to think that also the electrostatic interaction can play a significant role. It was possible to validate such hypothesis by repeating the calculation of the energy curve as a function of the canting angle with different values of the U_{eff} : $U_{eff} = 2.4, 2.8, 3.2, 3.4 \text{ eV}$. As always, the fully relativistic LDA + U + SOC scheme was used with the unit cell optimized as previously ($\delta c = 0 \%$).

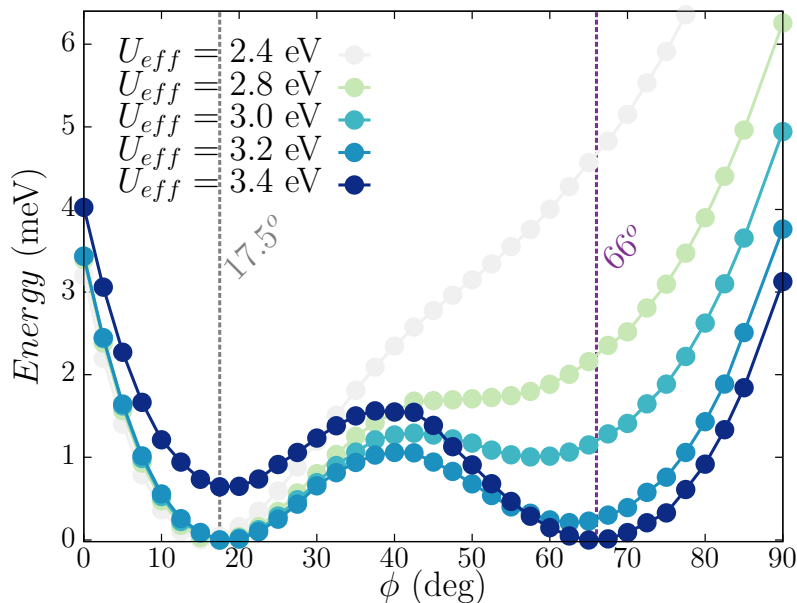


Figure 4.8: Energy as a function of θ_c with different U_{eff} for BNOO.

The various curves are calculated with U_{eff} in the interval from 2.4 eV to 3.4 eV and they are all arbitrarily scaled in order to have their minimum energy in correspondence of 0 eV. The red dotted line identifies the $\phi_1 \sim 24^\circ$ minimum, while the yellow dotted line the $\phi_2 \sim 72^\circ$

The result is very intriguing (see Figure 4.8). It shows that there is a very strong dependence of the magnetic ground state on the electron correlation that, as well as for the distorted cases, can enhance one minimum and lead to two different magnetic configurations, one that is canted antiferromagnetic and one canted ferromagnetic. The "phase transition" appears at $U_{eff} \approx 3.3$ eV which brings, for greater values, to a minimum at $\phi = \phi_2 \approx 66^\circ$ that is compatible with the experiments. In Table 4.6 the difference in energy between the two minima $\Delta E = E_{\phi_1} - E_{\phi_2}$ is shown for three different cases. We believe that the ΔE value for $U_{eff} = 3.4$ eV can be interesting in order to have an experimental proof of the veracity of this result, if, somehow, a phase transition can be induced via the application of a magnetic field along the [110] direction.

Last but not least, we remind that all these calculations were made with fixed structure optimized with $U_{eff} = 3.0$ eV. One could point out that such results are not affordable because the structure can locally change with different values of U_{eff} and that it should be optimized in each case. However the changes of the on site Coulomb energy are enough small to not perturb in a significant way the structure. Furthermore, even though they are not reported in detail here, these calculations were repeated with optimized unit cells and they substantially coincide.

U_{eff} (eV)	$\Delta E_{\phi_1, \phi_2}$ (meV)
3.0	+ 1.0
3.2	+ 0.2
3.4	- 0.6

Table 4.6: **Energy difference between minima for different U_{eff} . $\Delta E = E_{\phi_1} - E_{\phi_2}$.**

4.4 Origin of canted magnetism

As anticipated, the first attempt made for analyzing the energy curve as a function of the canting angle, was to map the total energies onto a Spin Hamiltonian of the form

$$\mathcal{H}_{ij} = \frac{J}{2} \sum_{\langle ij \rangle} (\mathbf{S}_i \cdot \mathbf{S}_j) + \frac{1}{2} \sum_{\langle ij \rangle} \mathbf{D}_{ij} \cdot (\mathbf{S}_i \times \mathbf{S}_j) + K \sum_i H_{SIA}(\mathbf{S}_i), \quad (4.4)$$

where only nearest neighbor exchange interaction is considered. Since our unit cell has only two inequivalent magnetic sites on parallel planes, with different canting angles, the total Spin Hamiltonian can be rewritten as

$$\mathcal{H} = 2JS^2(1 + 2\cos(2\phi)) - 4D_z S^2 \sin(2\phi) + 2K \cos(4\phi). \quad (4.5)$$

If one tries to fit the energy curve with a fitting function $E(\phi)$ in the form of

$$E(\phi) = A_0 + A_1 \cos(2\phi) + A_2 \cos(4\phi) + A_3 \sin(2\phi) \quad (4.6)$$

the resulting fitting curve is the dotted green line of Figure 4.10.

The fit is not in agreement with the computational curve found from ab initio calculations and cannot predict the correct position of the minima. Despite the SH formalism was able, in several cases, to predict the ground state magnetic phase even for TMOs with relevant SOC interactions, this time it is not sufficient. This discrepancy is due to the poor description of the SOC in the weak SOC regime, i.e. its strength is strong enough to not allow to treat it as a small perturbation.

The SOC effect must be considered from the beginning as the driving effect of the canted state and every spin operator must be changed into a Pseudo Spin operator, i.e. a semiclassical vector referred to the total angular momentum operator. This is described in more detail in the following lines.

We moved to the Pseudo Spin Hamiltonian (PSH) formalism, i.e. we considered the limit of strong SOC interaction. Within this limit, already mentioned in Section 2.2.6,

the coupling between the Spin and the Orbital angular momentum is strong enough to completely entangle the two operators in a way that the SOC interaction cannot be considered as a small perturbation. As a consequence, the total angular momentum eigenvalue J is a good quantum number. We approached the PSH from a mean field level and the theoretical procedure for deriving the final form is schematically described here. It was practically done via a Mathematica program (See Appendix ??).

0) In analogy to the SH formalism, we assume that the Hilbert space of our system can be reduced to a subset of states that are low lying in energy and contain all the physical properties of interest. Such states are the states with total angular momentum eigenvalue $J = 3/2$. This can be done through a unitary transformation of the total Hamiltonian [43]. The low lying states will be described by spin like operators, this time referred to Pseudo Spins of the system.

1) We write the pseudospin matrices for $J = 3/2$: $\mathbf{j} = (j^x, j^y, j^z)$ as

$$j^x = \begin{pmatrix} 0 & \sqrt{3}/2 & 0 & 0 \\ \sqrt{3}/2 & 0 & 1 & 0 \\ 0 & 1 & 0 & \sqrt{3}/2 \\ 0 & 0 & \sqrt{3}/2 & 0 \end{pmatrix} \quad (4.7)$$

$$j^y = \begin{pmatrix} 0 & -i\sqrt{3}/2 & 0 & 0 \\ i\sqrt{3}/2 & 0 & -i & 0 \\ 0 & i & 0 & -i\sqrt{3}/2 \\ 0 & 0 & i\sqrt{3}/2 & 0 \end{pmatrix} \quad (4.8)$$

$$j^z = \begin{pmatrix} 3/2 & 0 & 0 & 0 \\ 0 & 1/2 & 0 & 0 \\ 0 & 0 & -1/2 & 0 \\ 0 & 0 & 0 & -3/2 \end{pmatrix} \quad (4.9)$$

2) We project those operators onto the direction of the two non collinear magnetic moments. The reference frame used in the Spin Hamiltonian was the one with the x,y axis parallel to the [100] and [010] crystallographic axis and the angle ϕ constructed by considering the space in between the magnetic moments and the [110] axis. Here we consider a new angular reference frame: $\alpha = 45^\circ - \phi$. By looking at Figure 4.9 is easy to see that if α is the angle between the spin and the two axis, the green and yellow unitary vectors can be written as

$$\hat{\mathbf{n}}_1 = (\cos(\alpha), \sin(\alpha), 0) \quad \hat{\mathbf{n}}_2 = (\sin(\alpha), \cos(\alpha), 0) \quad (4.10)$$

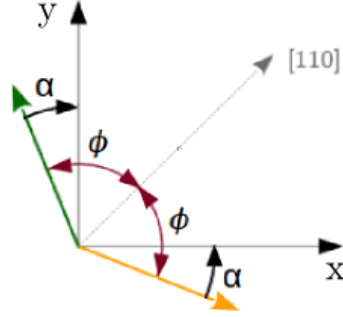


Figure 4.9: New reference frame for the Pseudo Spins.

with $\alpha \in [-45^\circ, 45^\circ]$. Therefore the operators are rewritten along the 1,2 directions as

$$\mathbf{j}_1 = \mathbf{j} \cdot \hat{\mathbf{n}}_1 \quad \mathbf{j}_2 = \mathbf{j} \cdot \hat{\mathbf{n}}_2 \quad (4.11)$$

3) The eigenvectors and eigenfunctions are calculated for those projected spins and the eigenvector with highest eigenvalue ($3/2$) is chosen as the spinor part of the wavefunction $|\Psi_1\rangle$ or $|\Psi_2\rangle$ where 1 and 2 are referred to the two non equivalent interacting spins. This is a common assumption when the mean field analysis is applied [41].

4) The PSH is calculated from a Multipolar Tensor expansion of the exchange interactions. The most general form of such Hamiltonian is given by [68]

$$H = \frac{1}{2} \sum_{i,j} \sum_{K,Q} J_{K_i, K_j}^{Q_i, Q_j}(i, j) T_{K_i}^{Q_i}(J) T_{K_j}^{Q_j}(J) , \quad (4.12)$$

where $K \leq 2J + 1$, $Q = s, x, y, z$, and T_K^Q are the cubic harmonic superbasis or *multipolar tensor operators* whose rank is given by K . When $K = 1$ we talk about *dipole*, $K = 2$ identifies a *quadrupole* and $K = 3$ the *octupole* [64]. The definition of the multipolar tensor operators can be found in several textbooks and is

$$T_{KQ}(J) = \sum_{MM'} (-1)^{J-M} (2K+1)^{1/2} \times \begin{pmatrix} J & J & K \\ M' & -M & Q \end{pmatrix} |JM\rangle \langle JM'| \quad (4.13)$$

In particular, for $J = 3/2$ and in a cubic environment, the multipolar tensor operators can be written as in Table 4.7.

5) The Hamiltonian contains terms that are referred to the two non equivalent spin sites, and therefore one should construct a total wavefunction, function of the two spinors. This, however, can be avoided on a mean field level since the mean field approach, that

Moment	Symmetry	Operator
Dipole	Γ_4	j^x j^y j^z
Quadrupole	Γ_3	$O^{3z^2} = [3(j^z)^2 - \mathbf{j}^2]/\sqrt{3}$ $O^{x^2-y^2} = (j^x)^2 - (j^y)^2$
	Γ_5	$O^{xy} = \overline{j^x j^y}/2$ $O^{yz} = \overline{j^y j^z}/2$ $O^{xz} = \overline{j^z j^x}/2$
Octupole	Γ_2	$T_{xyz} = \sqrt{15}/6 \overline{j^x j^y j^z}$
	Γ_4	$T_\alpha^x = (j^x)^3 - [\overline{j^x(j^y)^2} + \overline{(j^z)^2 j^x}]/2$ $T_\alpha^y = (j^y)^3 - [\overline{j^y(j^z)^2} + \overline{(j^x)^2 j^y}]/2$ $T_\alpha^z = (j^z)^3 - [\overline{j^z(j^x)^2} + \overline{(j^y)^2 j^z}]/2$
	Γ_5	$T_\beta^x = \sqrt{15}[\overline{j^x(j^y)^2} - \overline{(j^z)^2 j^x}]/6$ $T_\beta^y = \sqrt{15}[\overline{j^y(j^z)^2} - \overline{(j^x)^2 j^y}]/6$ $T_\beta^z = \sqrt{15}[\overline{j^z(j^x)^2} - \overline{(j^y)^2 j^z}]/6$

Table 4.7: **Multipolar tensor operators for a cubic magnetic environment.** The Multipole moments are considered within a cubic Γ_8 quartet. Bars over symbols correspond to permutations of dipole operators, e.g. $\overline{j^x(j^y)^2} = j^x j^y j^y + j^y j^x j^y + j^y j^y j^x$.

can be summarized by equation $O(1)O(2) \Rightarrow \langle O(1) \rangle O(2) + O(1) \langle O(2) \rangle - \langle O(1) \rangle \langle O(2) \rangle$, allows to calculate the mean value of the Hamiltonian as

$$\langle H \rangle = \langle \Psi_1 | \otimes \langle \Psi_2 | H | \Psi_1 \rangle \otimes | \Psi_2 \rangle = \langle \Psi_1 | H(1) | \Psi_1 \rangle \langle \Psi_2 | H(2) | \Psi_2 \rangle \quad (4.14)$$

where $H(1)$ and $H(2)$ are the parts in the Hamiltonian that act on the Hilbert space of the 1st or 2nd spin respectively.

The result is

$$\langle H \rangle = \frac{1}{2} \sum_{i,j} \sum_{K,Q} J_{K_i,K_j}^{Q_i,Q_j}(i,j) \langle T_{K_i}^{Q_i}(J) \rangle \langle T_{K_j}^{Q_j}(J) \rangle . \quad (4.15)$$

6) The calculation of the multipolar tensor operators is done as bra ket products in the form of

$$\langle T_{K_i}^{Q_i} \rangle = \langle \Psi_i | T_{K_i}^{Q_i} | \Psi_i \rangle . \quad (4.16)$$

where $|i\rangle$ is the eigenvector of the i -th Pseudo Spin Operator. All the mean values are computed and the products are taken in order to consider only dipole-dipole, quadrupole-quadrupole and octupole-octupole products (i.e. 2nd order, 4th order and 6th order interactions) and then the results are converted in order to return to the old reference frame with ϕ as canting angle.

The choice of even powers of exchange interactions is due to the time reversal symmetry.

It is worth noticing that every tensor contains powers of j^x , j^y and j^z (see Table 4.7). As a consequence, since the spins are rotated in the xy plane, no z component of the total angular momentum operator \mathbf{j} is present. As an example we consider the mean value of a Dipole operator acting on the 1st spin. It can be evaluated as

$$\langle j_1^x \rangle = \langle \Psi_1 | j^x | \Psi_1 \rangle \equiv S_1^x , \quad (4.17)$$

where the nomenclature used is similar to the one adopted in the Spin Hamiltonian case with the difference that now it is referred to a Pseudo Spin semiclassical vector. The

Hamiltonian, in practice becomes

$$H = A_0 + H_1 + H_2 + H_3 + H_4 \quad (4.18)$$

where

$$H_1 = J_x S_1^x S_2^x + J_y S_1^y S_2^y \quad (4.19)$$

is the *Exchange* (Ex) term,

$$H_2 = K[(S_1^x)^2 - (S_2^y)^2] \quad (4.20)$$

is the *Anisotropy* (An),

$$H_3 = q_3 O_1^{xy} O_2^{xy} + q_4 O_1^{x^2-y^2} O_2^{x^2-y^2} \quad (4.21)$$

is the *Quadrupolar* (QP) interaction and

$$H_4 = \sum_{\eta,l} C^{\eta,l} T_{1,\eta}^l T_{2,\eta}^l \quad (4.22)$$

groups all the 16 *octupolar* (OCP) interactions; where $l = x,y$, $\eta = \alpha, \beta$. The angular symetry of the two non equivalent magnetic moments leads to few angular terms.

More specifically

$$\langle H \rangle - \langle H_4 \rangle \propto \cos(2\phi) + \sin(2\phi) + \cos(4\phi) \quad (4.23)$$

and

$$\langle H_4 \rangle \propto \sum_{n=1}^3 \cos(2n\phi) + \sum_{m=1}^3 \sin(2m\phi) . \quad (4.24)$$

In equation 4.23 all the exchange interactions are taken into account apart from the octupolar ones. The expression is analogue to the one already obtained within the Spin Hamiltonian formalism that we already know is not enough for fitting the energy curve. It is important to underline that the octupolar term gives 6 contributions in terms of cosines and sines, with some of them are already present in the $\langle H \rangle - \langle H_4 \rangle$ term. This does not mean that the octupolar interactions are the only ones present, especially because they are sixth order spin interactions, but they are somehow entangled to other angular contributions. This disentanglement problem is theoretically demanding and more studies are needed.

However the number of fitting parameters can be reduced to 5 since the term $\propto \sin(6\phi)$ is at least one order of magnitude lower than the others and it is of the order of 1/100 meV. The function used for fitting the energy curve is therefore

$$E(\phi) = A_0 + \sum_{n=1}^3 A_n \cos(2n\phi) + \sum_{m=1}^2 B_m \sin(2m\phi) . \quad (4.25)$$

The fitting curves obtained are plotted in Figure 4.10, where, the two models, with and without OCP contribution are compared. The dotted green line, already found within the Spin Hamiltonian approach, is obtained with the A1, A3 and B1 coupling constants and is not in agreement with the computational curve. The full model with the coupling constants A1, A2, A3, B1 and B2 is the red line in Figure 4.10 and is in optimal agreement with the computed data, the values of the fitting parameters are in Table 4.8.

The data clearly show that the inclusion of distinct OCP is essential for obtaining an accurate fit with the first principles energies, in particular for a correct description of the global minimum: without OCP terms the minimum is found at $\approx 72^\circ$, whereas

with OCP terms it is shifted down to $\approx 66^\circ$, in much better agreement with experiment ($\phi \approx 67^\circ$).

In the following lines we will analyze the competition between the two minima ϕ_1 and ϕ_2 in terms of the magnetic coupling constants, in order to acquire more informations on the driving forces which stabilise the correct state.

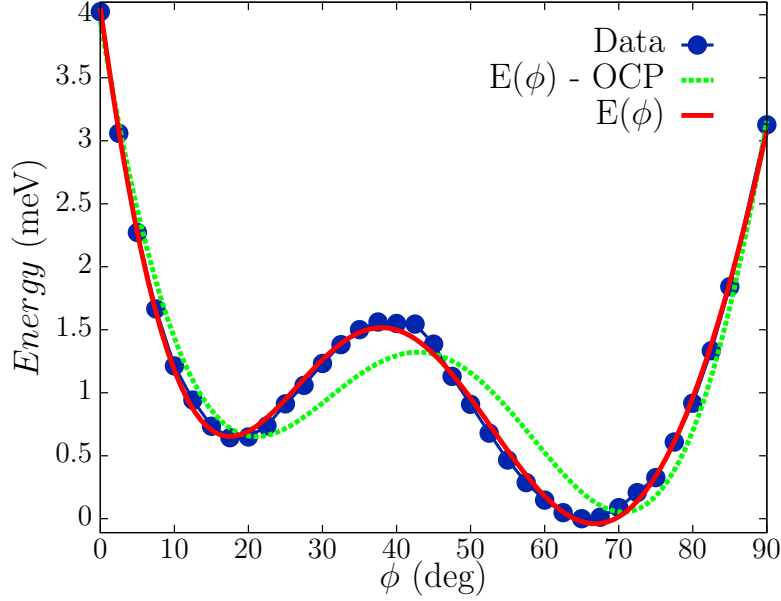


Figure 4.10: Fit of the energy curve as a function of the canting angle ϕ for $U-J = 3.4$ eV.

Parameters	A_1	A_2	A_3	B_1	B_2
Meaning	Ex + OCP	QP + OCP	OCP	An + OCP	OCP
Angular Dependence	$\cos(2\alpha)$	$\cos(4\alpha)$	$\cos(6\alpha)$	$\sin(2\alpha)$	$\sin(4\alpha)$
Value (meV)	1.34	-3.83	-0.85	-9.93	-1.13

Table 4.8: Values of the fitting parameters for BNOO.

So we ignored the contributions that are symmetric with respect to $\phi = 45^\circ$ since they do not change the relative weights of the two minima. These terms are QP + OCP (A_2) and the An + OCP one (B_1).

The remaining terms are plotted in Figure 4.11 as a function of the canting angle. The curves clearly underline the importance of the Exchange interaction (orange dotted line)

together with the octupolar one (green dotted line). The sum of these two contributions, given by the blue line of Figure 4.11, has a strong global minimum close to $\phi \approx 66^\circ$ and a global maximum at $\phi \approx 26^\circ$ which goes against the other octupolar term given by B_2 .

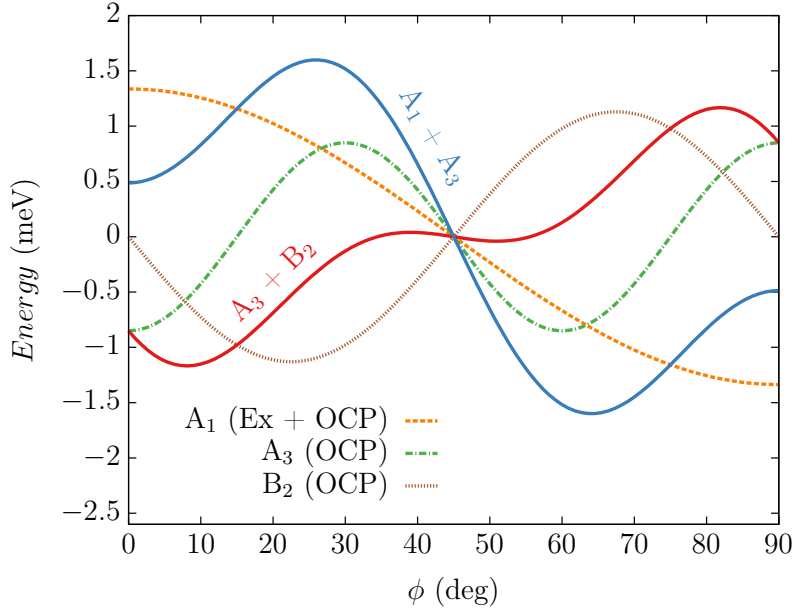


Figure 4.11: Plot of the asymmetric contributions with respect to $\phi = 45^\circ$.

The goal was then to try to see more in detail which are the terms in the fitting function that truly influence the magnetic state. This was done by repeating the fitting procedure for the other curves calculated with different values of U_{eff} . The results are plotted in Figure 4.13, 4.14 together with the different contributions coming from the non-symmetric terms of the Hamiltonian.

In the graphs is clear that Ex + OCP term (A_1) plays a very significant role since it literally changes the equilibrium in the different situations. We address such term to be the one that gives the strongest contribution in the overcome of $\phi_2 \approx 66^\circ$ as demonstrated also by plotting the strength of the asymmetric terms, i.e. their proportionality constants as a function of U_{eff} (see Figure 4.12). The Ex + OCP proportionality constant A_1 (see Equation 4.25) increases considerably with a net $\Delta E \approx 3.62$ meV. The other octupolar parameters A_3 and B_2 are almost constant. Only the former tends to decrease with a net change of the value between the two estrema that is $\Delta E \approx -0.12$ meV. Also the symmetric contributions tend to decrease with a $\Delta E \approx -0.8$ meV for A_2 and $\Delta E \approx -1.0$ meV for B_1 .

However, if the A_1 term is connected to the two different magnetic configurations,

the role of the OCP interactions is still non negligible since only by adding it the fit agrees with the computational data.

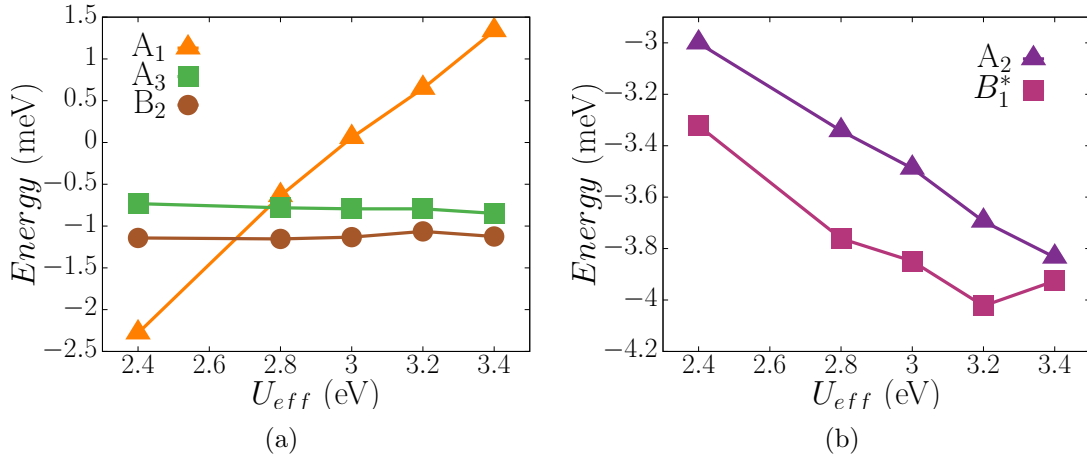


Figure 4.12: (a) It is the plot of the dependence of the asymmetric fitting terms on U_{eff} , where A_1 is Ex + OCP, A_3 is OCP and B_2 is OCP. (b) It is the plot of the dependence of the symmetric contributions on U_{eff} . The parameter B_1^* is $B_1 - 6$ meV and is the An + OCP, while A_2 is the QP + OCP.

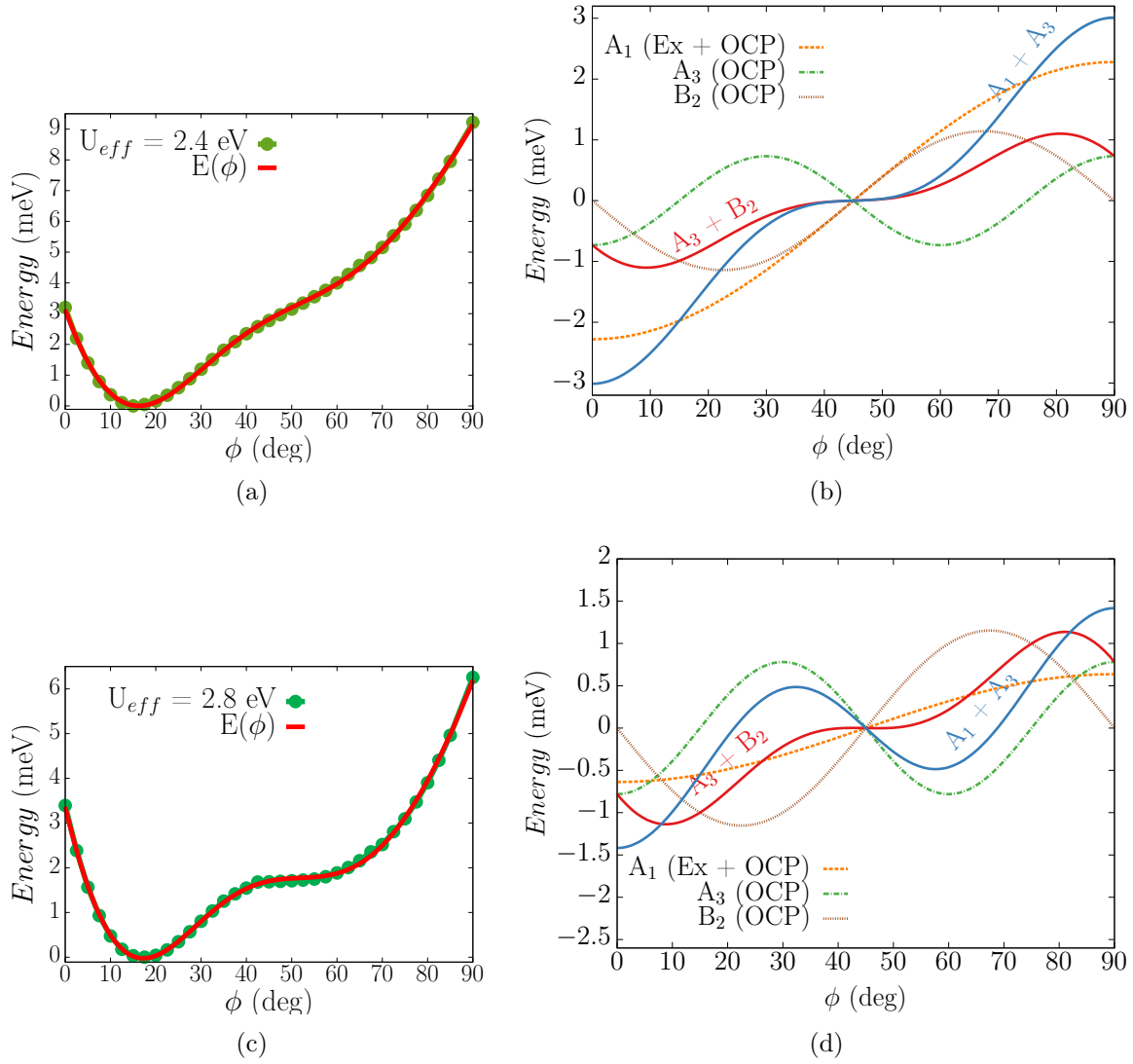


Figure 4.13: Fitting curve (Left Figure) and asymmetric contributions (Right Figure) for energy curve as function of the canting angle ϕ with $U-J = 2.4$ eV.

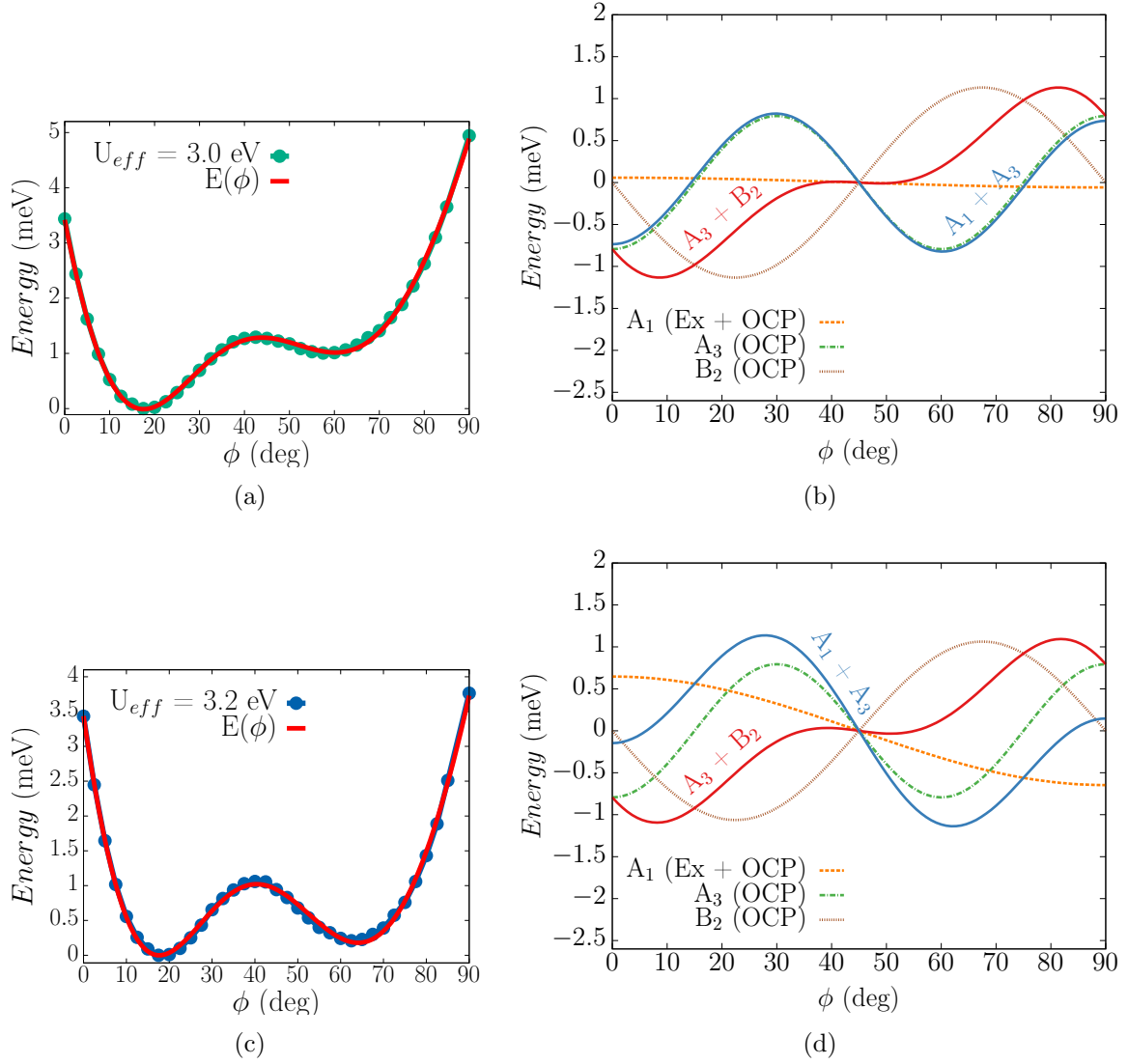


Figure 4.14: Fitting curve (Left Figure) and asymmetric contributions (Right Figure) for energy curve as function of the canting angle ϕ with $U-J = 3.2$ eV.

4.5 Preliminary results on BCOO

We studied the structural, electronic and magnetic properties of BCOO fully ab initio within the LDA + U + SOC scheme. The most intriguing and challenging aspect of BCOO is its magnetic ground state, since several phases compete depending on the strength of internal parameters. Although this may seem counterintuitive, we started studying this material directly by probing its magnetic properties. Our choice is justified here by the strong correlation between electronic, structural and magnetic degrees of freedom in relativistic Osmates that was indeed demonstrated for BNOO. Furthermore we decided to split the calculations in two sets: with and without local ionic relaxation.

The reasons can be found again in the results obtained for BNOO which highlight the importance of local distortions on the magnetic ground state. We chose to probe also the magnetic properties of the undistorted BCOO since no experimental study on local distortions is found at the state of the art.

For both sets of preliminary calculations we used the fully relativistic LDA + U + SOC scheme with $U_{eff} = 3.0$ eV together with a high convergence precision of $\sim 10^{-8}$ eV and an $E_{cutoff} = 600$ eV. The unit cell chosen is a larger unit cell of dimensions $a\sqrt{2} \times a\sqrt{2} \times a$ with $a = 8.3462$ Å being the experimental value; it has four inequivalent magnetic ionic sites that allow to characterize more frustrated magnetic geometries. The corresponding \mathbf{k} -mesh used was $4 \times 4 \times 4$.

As already anticipated, the main difference resides in the ionic relaxation that is applied, in one case, locally and only for the oxygen atoms. The quasi-Newton (or variable metric) algorithm was used as in the BNOO case with magnetic moments initialized according to the specific task. The oxygens are therefore freely to move to their optimal position without any constraint.

Geometrical frustration, as well as exotic quantum phases, are predicted theoretically and it was mandatory to study them. In particular, the magnetic configurations analysed are:

AFM Out of Plane It is an AFM state with spins aligned antiferromagnetically in the (a,b) plane and ferromagnetically in the (a,c) plane (see as an example Figure 4.15 (a)). We chose 3 different directions of the spins: 100, 110 and 111 but, for simplicity, we plotted only the AFM 100 direction (see Figure 4.15 (a)).

AFM In Plane It is an AFM state with spins aligned antiferromagnetically in the (a,c) plane and ferromagnetically in the (a,b) one (see as an example Figure 4.15 (b)). Again we chose as possible directions of the spins the 100, 110 and 111, but we plotted only the AFM 100 (see Figure 4.15 (b)) and AFM 110 (see Figure 4.15 (d)).

FM It is a complete ferromagnetic state with spins aligned along the 100 (see Figure 4.15 (c)), 110 (see Figure 4.15 (e)) and 111 (see Figure 4.15 (f)).

AFM 4 sub The acronym *4 sub* means 4 sublattice. We probed 5 different 4 sublattice structures. Three of them are built starting from an AFM configuration along 100, 110 or 111 in the first (a,b) plane. The second plane is constructed by rotating the spins by 90° and then the third one is again the former AFM phase. As an example in Figure 4.15 (h) there is a 110 AFM 4 sublattice structure.

Another 4 sublattice that we tried consists in a chiral structure (see Figure 4.15 (g)) done by constraining the direction of the spins alternatively along the 4 different 111 directions in order to have an overall AFM state.

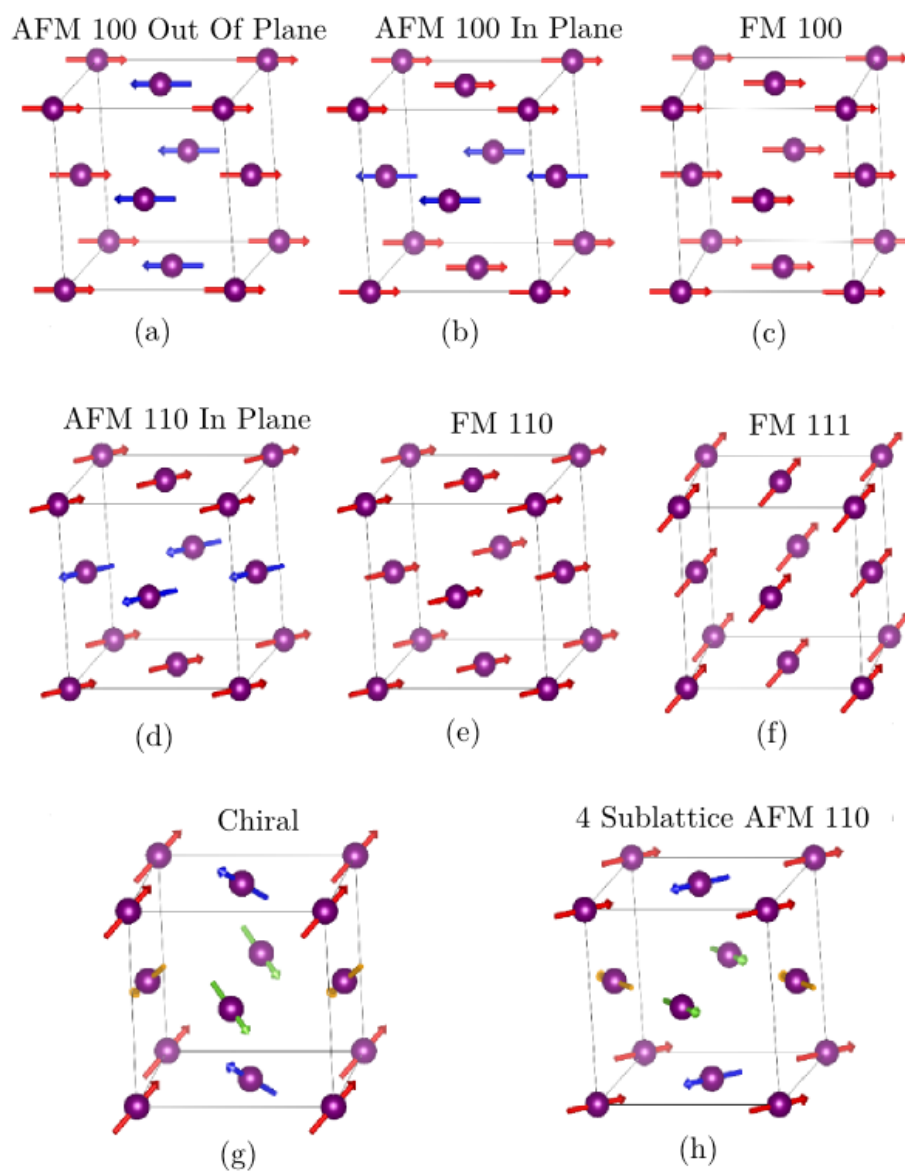


Figure 4.15: Some of the magnetic phases probed via *ab initio* calculations for BCOO. in Figure (a) the AFM 100 out of plane phase, in (b) the AFM 100 in plane phase, in (c) the FM 100 phase. In Figure (d) the AFM 110 in plane phase, in (e) and (f) the FM 110 and 111 configurations respectively. In Figure (g) the chiral AFM phase and in (h) the 4 sublattice AFM 110 phase.

4.6 Frustration without ionic relaxation

The results found without ionic relaxation are listed in Table 4.9. The energies are compared in the ΔE column with respect to the lowest one, i.e. the AFM 110 configuration. So far these calculations can allow for the evaluation of the first and second nearest neighbour exchange couplings, but this is not yet done and further analysis are required.

Magnetic Phase		ΔE
	Detail	(meV)
AFM100	Out of plane	5.95
	In plane	5.95
AFM110	Out of plane	5.37
	In plane	0
AFM111	Out of plane	1.49
	In plane	4.40
AFM4sub	100	10.17
	110	14.19
	111	4.16
	Chiral	7.94
FM100		21.04
FM110		21.05
FM111		Non converged

Table 4.9: **Energy for different magnetic configurations for BCOO without ionic relaxation.**
The energies are shifted with respect to the configuration with the lowest one.

4.7 Frustration with ionic relaxation

We repeated the calculations above but with ionic relaxation, i.e. by allowing the oxygens to move freely and relax to their optimal position while constraining the direction of the magnetic moments. These calculations were very challenging because of the larger unit cell used and because they combine three expensive tasks: SOC, ionic relaxation and magnetism. The result is remarkable. It shows that again there is, for every magnetic configuration, a local symmetry breaking that can be thought as a Model A with

compression (see Section 3.1). In Table 4.10 the relative displacements are tabulated for each magnetic configuration. The ones in bold font are the ones of the magnetic configuration that is lower in energy (see Table 4.11) i.e. they are relative to the AFM 110 In Plane phase.

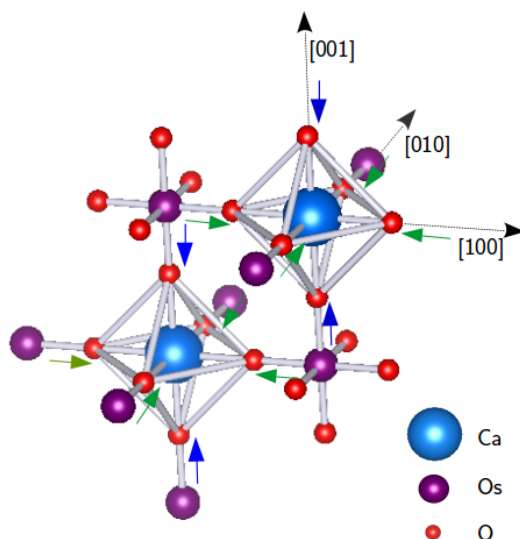


Figure 4.16: Local distortions for the AFM 110 in plane magnetic configuration of BCOO.

Two considerations are necessary to this point. The first is that every local displacement of the oxygens is different depending on the magnetic configuration. This further demonstrates the strong correlation between local symmetry and magnetism in relativistic osmates. Furthermore the relative displacements are in general one order of magnitude lower than the ones encountered in BNOO. It is probably due to the new electronic configuration of the Os atom, which is now in a d^2 state. The second consideration regards the specific symmetry of the AFM 110 In Plane that is the one of Figure 4.16, where is clear that the compressions in the (a,b) plane are all the same, while they differ from the c ones that are slightly larger.

We did not investigate any further the local symmetry of this d^2 double perovskite since no experimental measurements are available. We are however confident, on what was already found also in BNOO, that such compression and magnetic ground state can be validated by experiments. In analogy with BNOO, we studied the electronic properties of BCOO and repeated the canting procedure, as it will be described in more detail in the following Sections. Finally, it is worth noticing that, in general, the total energies of the relaxed structures is lower than the respective fixed ones as it is shown in Table 4.11 in correspondence of $\Delta E_D = E_{undistorted} - E_{distorted}$.

Magnetic Phase		δa	δb	δc
	Detail	(%)	(%)	(%)
AFM100	Out of plane	-0.09	-0.98	-0.89
	In plane	-0.09	-0.89	-0.98
AFM110	Out of plane	-0.46	-0.72	-0.80
	In plane	-0.52	-0.52	-0.94
AFM111	Out of plane	-0.66	-0.83	-0.49
	In plane	-0.64	-0.64	-0.71
AFM4sub	100	-1.26	-0.05	-0.68
	110	-0.54	-0.54	-0.88
	111	-0.77	-0.70	-0.50
	Chiral			

Table 4.10: **Relative displacements of the Ca-O bondlengths in BCOO for different magnetic configurations.**

Magnetic Phase		Energy per f.u.	ΔE	ΔE_D
	Detail	(eV)	(meV)	(meV)
AFM100	Out of plane	-67.142446	3.06	-29.55
	In plane	-67.142446	3.06	-26.66
AFM110	Out of plane	-67.139709	5.80	-26.23
	In plane	-67.145505	0	-29.55
AFM111	Out of plane	-67.143455	2.05	-26.10
	In plane	-67.140189	5.32	-25.74
AFM4sub	100	-67.140994	4.51	-32.32
	110	-67.130975	14.53	-26.32
	111	-67.140695	4.81	-26.01
	Chiral	-67.136689	8.82	-25.66

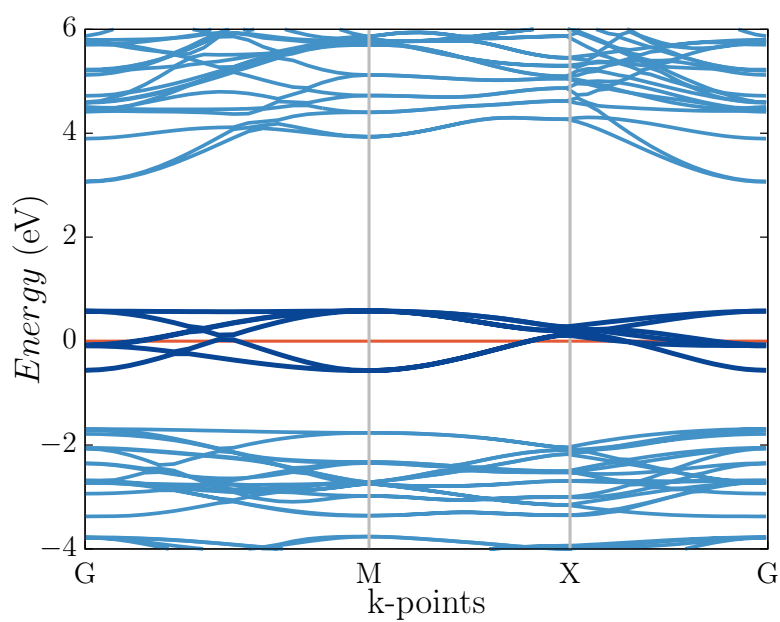
Table 4.11: **Energy for different magnetic configurations for BCOO with ionic relaxation.**

4.8 Electronic Bandstructure

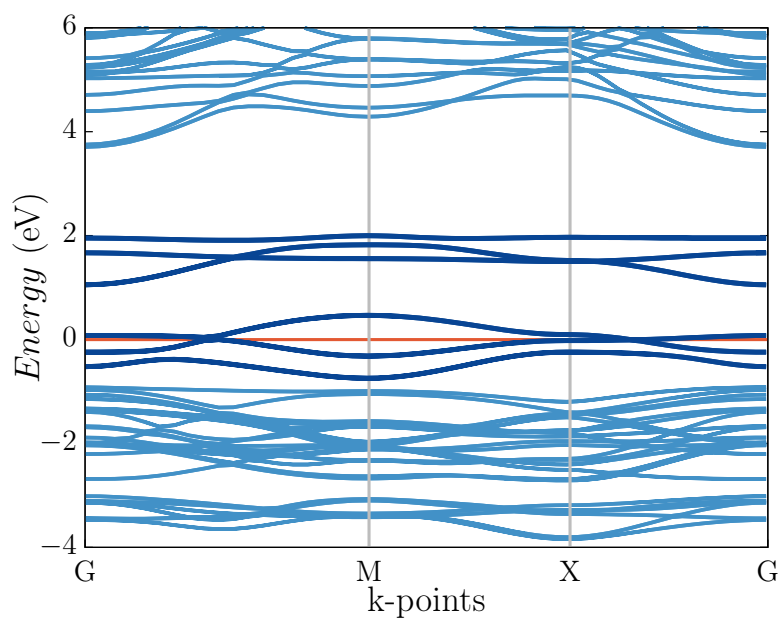
The electronic structure was calculated ab initio for the AFM 110 In Plane magnetic configuration with the distorted structure by using both LDA, LDA + U and LDA + U + SOC with $U_{eff} = 3.0$ eV. The result is remarkable because it shows that BCOO is a Dirac-Mott insulator, in fact, the LDA scheme leads to a metallic state that is not broken with the application of the on site Hubbard U (see Figure 4.17). Only by including SOC the system undergoes a metal-insulator transition and the gap can be opened (see Figure 4.18 (a)) with a value of ~ 0.558 eV. If the structure used is, instead, the experimental one, the energy gap is ~ 0.552 eV.

No cRPA calculations were run for this material, but we believe that, as well as for BNOO, its value can be strongly underestimated, since the strong hybridization of the oxygen p orbitals with the osmium d ones is found here too (see Appendix D).

We did not investigate the dependence of the electronic properties as a function of the electron correlation, we therefore do not know if this bandstructure is somehow dependent. The energy gap is, in this case, slightly larger than the correspondent one of BNOO by a value of ~ 0.1 eV. This is again addressed by the fact that Os has a different electronic configuration in BCOO, which changes the overall interactions with the effect of reducing the U_{eff} as well as the entanglement of the lattice and spin degrees of freedom.

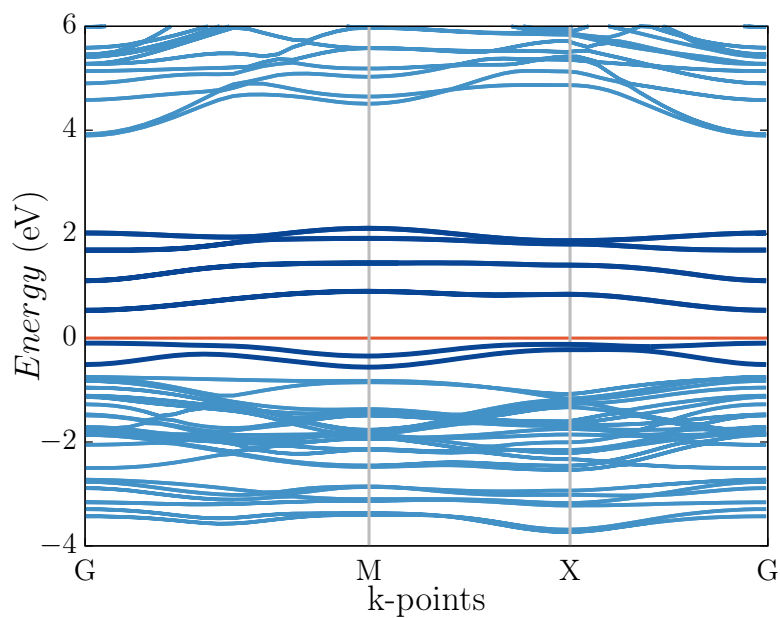


(a)

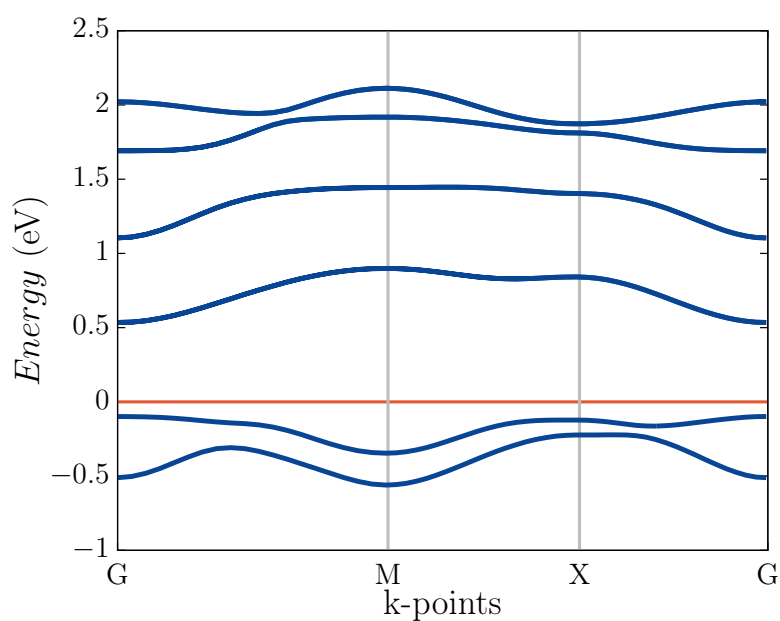


(b)

Figure 4.17: Bandstructure of BCOO with LDA and LDA + U. (a) Bandstructure of BCOO obtained within the LDA scheme. (b) Bandstructure of BCOO obtained with the LDA + U scheme with $U_{eff} = 3.0$ eV.



(a)



(b)

Figure 4.18: Bandstructure of BCOO with LDA + U + SOC. (a) Bandstructure of BCOO obtained within the LDA + U + SOC scheme with $U_{eff} = 3.0$ eV. (b) Zoom of the bands near the Fermi energy.

4.9 Canting angles in BCOO

The canted ferromagnetic phase found in BNOO led us think that a similar configuration could be found in BCOO. Then we calculated the total energy of BCOO as a function of the canting angle by following the same procedure of BNOO and with a setup that is also analogous to the one already used for BNOO, apart from the structure used as we will discuss in the following lines. First of all it is important to underline that the magnetic configuration with lower energy is the AFM 110 In Plane, in fact it is basically a two sublattice antiferromagnetic phase with $\phi = 90^\circ$ in the reference frame of BNOO. This allowed to restrict the unit cell to a $a/\sqrt{2} \times a/\sqrt{2} \times a$ unit cell.

Then we actually repeated the canting procedure done with BNOO, this time with two different structures:

Experimental : For this one we calculated the canting curve with three different values of U_{eff} (see Figure 4.19 (a)).

The result is that the AFM 110 In Plane configuration is indeed the more stable also when the electron correlation is tuned.

Relaxed : In this case we relaxed the local structure step by step. It means that, while changing the canting angles, we relaxed the position of the oxygens according to that magnetic configuration. Since we found for the experimental structure that no significant change in the canting curve is present with different values of U_{eff} , we decided to calculate everything with $U_{eff} = 3.0$ eV. This was probably the most computational-demanding task done.

The result is in agreement with what was found previously, i.e. the AFM 110 In Plane configuration is the ground state magnetic configuration (see Figure 4.19 (b)). We believe that further experiments can clarify the correctness of this result.

No theoretical analysis and fit of this curves is done yet, and further studies are needed.

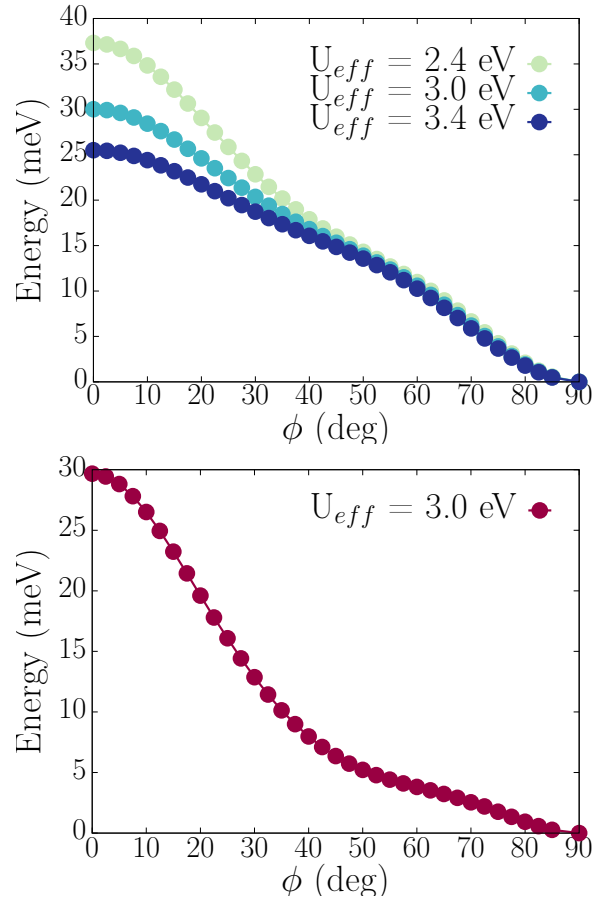


Figure 4.19: Energy as a function of ϕ with different U_{eff} for BCOO.

In Figure (a) the various curves are calculated with U_{eff} in the interval from 2.4 eV to 3.4 eV and they are all arbitrarily scaled in order to have their minimum energy in correspondence of 0 eV. This calculations are done with fixed structure. In Figure (b) the energy is calculated as a function of the canting angle with structure locally relaxed in every step, i.e. at every point of the graph. Only the oxygens are allowed to move.

Chapter 5

Conclusions

*For this dissertation I studied the physical properties of $\text{Ba}_2\text{NaOsO}_6$ and $\text{Ba}_2\text{CaOsO}_6$ via *ab initio* calculations. The use of the DFT implementation provided by the University of Vienna with the VASP code allowed to characterize, on a computational level, as well as on a theoretical one, the main aspects of such materials. The period that I spent in the University of Vienna gave me the opportunity to acquire a good knowledge of *ab initio* codes and on how to use the VASP program for calculating structural, electronic and magnetic properties of bulk systems with DFT, DFT + U and the fully relativistic DFT + U +SOC . Furthermore, I could study several theoretical models for describing magnetic materials, like the Hubbard Model, the Spin Hamiltonian and the Multipolar Tensor formalism of Exchange interactions in strong spin-orbit coupled systems.*

Both $\text{Ba}_2\text{NaOsO}_6$ and $\text{Ba}_2\text{CaOsO}_6$ are challenging materials because of the interplay between several interactions, like Spin Orbit Coupling, Electron Correlation and hopping. For the former there is a wider range of publications that have built a good background for the comparison of the computational results with the experimental ones. Several NMR, μsR and powder diffraction experiments revealed that $\text{Ba}_2\text{NaOsO}_6$ does not undergo a structural phase transition when the sample is cooled, even though NMR measurements underlined a local structural distortion of the NaO octahedra. The main question regarding this material concerned the magnetic phase, since it was found to have a small magnetic moment of $\sim 0.2 \mu_B$ along the [110] direction, even though the isovalent materials show an antiferromagnetic phase and the Curie-Weiss temperature is negative. Some suggestions were made by both theoretical and experimental studies about the possibility of a canted magnetic configuration. Furthermore, previous computational calculations showed that BNOO is a Dirac-Mott insulator with a non negligible SOC effect, justified also by the heaviness of the Os atom itself.

The calculations that we made showed that BNOO is indeed a Dirac-Mott insulator,

with the insulating phase that is present for values of U_{eff} greater than 1.5 eV. Furthermore, we found that there is indeed a local structural distortion that corresponds to a non isotropic compression of the NaO octahedra along the principal axis driven by electron correlation and SOC. The low ferromagnetic moment is due to a two sublattice canted antiferromagnetic phase with canting angle $\phi \approx 66^\circ$ that is, however, not the only magnetic phase achievable. In fact, the global minima of the energy curve as a function of the canting angle is found to be $\phi \approx 17^\circ$ for values of U_{eff} lower than 3.4 eV, while, when $U_{eff} = 3.4$ eV a phase transition leads to the other minima, in agreement with the experiments. The competition between the two minima was observed also when changing the bondlengths of the NaO in the double perovskite and we showed that further compressions of the bonds along the z axis can lead to a global minima of $\approx 61^\circ$ when a U_{eff} of 3.0 eV is set.

From a theoretical point of view, this competition between the two phases can be justified only by considering a strong Spin Orbit Coupling regime, i.e. in the limit where the orbital angular momentum and the spin momentum are no more good quantum numbers and the Spin Hamiltonian formalism is no longer a good approximation. It was therefore necessary to switch to a multipolar tensor representation of the exchange interactions. This method, although very complicated, could be solved more easily thanks to a mean field analysis within a Pseudo Spin Hamiltonian approach i.e. by considering Pseudo Spins as quasi classical objects. This allowed us to write an explicit expression of the Hamiltonian with angular dependencies of the canted magnetic moments, with which we could fit the energy curve as a function of the canting angle. The fit is in agreement with the computational data and underlines the importance of high order spin interactions that are commonly not considered, like quadrupolar and octupolar. The latter are extremely important for the formation of the observed canting angle, even though they are not the driving force in the overcome of one minima over the other, which is, instead, found in the Exchange + Octupolar term. The Exchange + Octupolar terms are the ones that allow BNOO to undergo the phase transition from a canted ferromagnetic to a canted antiferromagnetic phase. It is obvious that, such terms, have implicitly a dependence over the Hubbard U or other implicit variables, but we could not reveal such dependence since we were not able, with a simple fit, to disentangle the different dipolar, quadrupolar and octupolar parameters.

The role of the multipolar interactions is still under investigation and, in this field, further studies are needed in order to reduce the fitting parameters according to symmetry properties or to exchange paths and hidden symmetries.

Regarding $\text{Ba}_2\text{CaOsO}_6$, very few literature is available and the only experiments done seem to reveal a possible antiferromagnetic phase. Theoretical studies, on the other hand, propose an enormous variety of possible magnetic phases that we tried to probe with ab initio calculations. We found that this material is also a Dirac-Mott Insulator, and that it also tends to distort locally with a similar local symmetry as the one found for BNOO, i.e. with CaO octahedra slightly compressed along the principal axis. The compression

is however smaller and it is probably due to the different electronic configuration that weakens Coulomb and Exchange interactions between nearest neighbors. An extensive and challenging study on the possible magnetic phases was done, revealing that the antiferromagnetic phase with magnetic moments aligned along the [110] direction is the ground state configuration. A canting procedure was tried again, this time with and without ionic relaxation in parallel, and the result is that the antiferromagnetic [110] arrangement of the magnetic moments is always the optimal one.

At the state of the art, we have not investigate yet, on a theoretical level, the origin of such properties and how much they are related to the Strong Spin Orbit Coupling regime or electron correlation, even though we have proven that, the latter, is not as relevant as is BNOO. Further calculations are also required in order to better probe the role of the electron occupancy of the Os electrons on the electronic structure and to see how, all these properties, are related to each other and can change when the materials are doped.

Appendix A

VASP files

In this Appendix the VASP files used for the *bondlength relaxation* and for the *Energy curve as a function of the canting angle* are introduced. No explanation of the various flags used is given since it can be found on the VASP Wiki website (https://cms.mpi.univie.ac.at/wiki/index.php/The_VASP_Manual)

A.1 Bondlength Relaxation

```
poscar_5.vesta
1.0
5.8597940000 0.0000000000 0.0000000000
0.0000000000 5.8597940000 0.0000000000
0.0000000000 0.0000000000 8.2870000000
Na Os Ba O
2 2 4 12
Selective

Direct
0.0000000000 0.0000000000 0.0000000000 F F F !Na
0.5000000000 0.5000000000 0.5000000000 F F F !Na
0.5000000000 0.5000000000 0.0000000000 F F F !Os
0.0000000000 0.0000000000 0.5000000000 F F F !Os
0.5000000000 0.0000000000 0.7500000000 F F F !Ba
0.0000000000 0.5000000000 0.7500000000 F F F !Ba
0.5000000000 0.0000000000 0.2500000000 F F F !Ba
0.0000000000 0.5000000000 0.2500000000 F F F !Ba
0.2744000000 0.2744000000 0.0000000000 T T T !O
0.7256000000 0.7256000000 0.0000000000 T T T !O
0.7256000000 0.2744000000 0.0000000000 T T T !O
```

```

0.274400000 0.725600000 0.000000000 T T T !0
0.225600000 0.225600000 0.500000000 T T T !0
0.774400000 0.774400000 0.500000000 T T T !0
0.774400000 0.225600000 0.500000000 T T T !0
0.225600000 0.774400000 0.500000000 T T T !0
0.000000000 0.000000000 0.741760000 F F F !0
0.000000000 0.000000000 0.258240000 F F F !0
0.500000000 0.500000000 0.758240000 F F F !0
0.500000000 0.500000000 0.241760000 F F F !0

```

The coordinates coloured in cyan are the ones of the oxygens along the z axis that are kept fixed and are changed manually.

KPOINTS

```

k-points
0
Gamma
6 6 6
0 0 0

```

INCAR

```

Electronic
ISTART = 0
ISMEAR = -5
EDIFF = 1E-6
NCORE = 4
LREAL = Auto
NELMIN = 5
ENCUT = 600
ISYM = -1 ! No symmetry is considered, as mandatory when SOC is included.

```

Magnetism

```

LNONCOLLINEAR = .TRUE.
MAGMOM = 6*0 6*0 2 * cos(23°) 2 * sin(23°) 0 2 * cos(23°) -2 * sin(23°) 0 48*0
VOSKOWN = 1
LORBIT = 11
I_CONSTRAINED_M = 1
RWIGS = 1.757 1.413 1.979 0.820

```

```
LAMBDA = 10
M_CONSTR = 6*0 6*0 2 * cos( $\phi$ ) 2 * sin( $\phi$ ) 0 2 * cos( $\phi$ ) -2 * sin( $\phi$ ) 0 48*0
AMIX = 0.1
BMIX = 0.00001
AMIX_MAG = 0.2
BMIX_MAG = 0.00001
```

On site interaction

```
LMAXMIX = 4
LDAU = .TRUE.
LDAUTYPE = 2
LDAUL = -1 2 -1 -1
LDAUU = 0 4.0 0 0
LDAUJ = 0 0.6 0 0 ! In this case U - J = 3.4 eV
LDAUPRINT = 1
```

Relaxation

```
ALGO = Fast
NSW = 40
IBRION = 1
POTIM = 0.5
ISIF = 1
EDIFFG = -0.01
```

Spin orbit coupling

```
LSORBIT = .TRUE.
LORBMOM = .TRUE.
GGA_COMPAT = .FALSE.
SAXIS = 0 0 1
```

A.2 Energy curve as a function of the canting angle

POSCAR

```

Poscar BN00
1.0000000000000000
5.8597939999999999 0.0000000000000000 0.0000000000000000
0.0000000000000000 5.8597939999999999 0.0000000000000000
0.0000000000000000 0.0000000000000000 8.2870000000000008
Na Os Ba O
2 2 4 12
Direct
0.0000000000000000 0.0000000000000000 0.0000000000000000
0.5000000000000000 0.5000000000000000 0.5000000000000000
0.5000000000000000 0.5000000000000000 0.0000000000000000
0.0000000000000000 0.0000000000000000 0.5000000000000000
0.5000000000000000 0.0000000000000000 0.7500000000000000
0.0000000000000000 0.5000000000000000 0.7500000000000000
0.5000000000000000 0.0000000000000000 0.2500000000000000
0.0000000000000000 0.5000000000000000 0.2500000000000000
0.2710209143261416 0.2687800860598489 -0.0000030054371949
0.7289791181542323 0.7312198963110810 0.0000030123777638
0.7269434753601111 0.2709415873710140 0.0000045647716994
0.2730574068705890 0.7290592515510516 -0.0000045717794096
0.2269474989373637 0.2290565245861210 0.5000038876258635
0.7730535278305852 0.7709426130298560 0.4999961107809585
0.7710215257392790 0.2312209905802058 0.4999982571162111
0.2289787398200336 0.7687792418362958 0.5000017280502946
0.0000000000000000 0.0000000000000000 0.7284900000000007
0.0000000000000000 0.0000000000000000 0.2715099999999993
0.5000000000000000 0.5000000000000000 0.7715099999999993
0.5000000000000000 0.5000000000000000 0.2284900000000007

```

The POSCAR is taken from the CONTCAR of the *Bondlength Relaxation*

KPOINTS

```

k-points
0
Gamma

```

```
6 6 6
0 0 0
```

INCAR

Electronic

```
ISTART = 1 ! The canting is done after a pre converged calculation.
ICHARG = 1 ! The CHGCAR file is taken from the pre converged calculation
ISMEAR = -5
EDIFF = 1E-8
NCORE = 4
LREAL = Auto
NELMIN = 5
ENCUT = 600
ISYM = -1 ! No symmetry is considered, as mandatory when SOC is included.
```

Magnetism

```
LNONCOLLINEAR = .TRUE.
MAGMOM = 6*0 2*cos( $\phi$ ) 2*sin( $\phi$ ) 0 2*cos( $\phi$ ) -2*sin( $\phi$ ) 0 48*0
VOSKOWN = 1
LORBIT = 11
I_CONSTRAINED_M = 1
RWIGS = 1.757 1.413 1.979 0.820
LAMBDA = 10
M_CONSTR = 6*0 2*cos( $\phi$ ) 2*sin( $\phi$ ) 0 2*cos( $\phi$ ) -2*sin( $\phi$ ) 0 48*0
AMIX = 0.1
BMIX = 0.00001
AMIX_MAG = 0.2
BMIX_MAG = 0.00001
```

On site interaction

```
LMAXMIX = 4
LDAU = .TRUE.
LDAUTYPE = 2
LDAUL = -1 2 -1 -1
LDAUU = 0 4.0 0 0
LDAUJ = 0 0.6 0 0 ! In this case U - J = 3.4 eV
LDAUPRINT = 1
```

Spin orbit coupling

```
LSORBIT = .TRUE.  
LORBOMOM = .TRUE.  
GGA_COMPAT = .FALSE.  
SAXIS = 0 0 1
```

DOS

```
EMIN = -15  
EMAX = 15  
NEDOS = 5001
```

The choice of initializing the magnetic moments as $2 * \cos(\phi)$ is due to the fact that $\cos(\phi) \in [-1 : 1]$ and therefore its value is in general quite small. In order to give more strength to the magnetic moments and be sure that VASP correctly "understand" their direction, their absolute value is doubled. In principle the results should be the same since the direction is the only thing that matters.

Appendix B

Spin

In this Appendix the mathematical formalism of spin operators is described.

B.1 Algebra of Spins

The spin \mathbf{S} whose eigenvalue is $S = 1/2$ is described through the Pauli matrices $\boldsymbol{\sigma}$ as $\mathbf{S} = \frac{\hbar}{2}\boldsymbol{\sigma}$, where

$$\sigma_x = \begin{pmatrix} 0 & 1 \\ 1 & 0 \end{pmatrix} \quad \sigma_y = \begin{pmatrix} 0 & -i \\ i & 0 \end{pmatrix} \quad \sigma_z = \begin{pmatrix} 1 & 0 \\ 0 & -1 \end{pmatrix} \quad (\text{B.1})$$

The spin algebra is very similar to the one of the angular momentum operator \mathbf{L} , in particular the following relation is valid

$$[S_i, S_j] = i\hbar\varepsilon_{ijk}S_k \quad (\text{B.2})$$

where i, j, k are the x, y, z components and ε_{ijk} is the Levi-Civita tensor. Equation B.2 shows that the spin components do not commute if $i \neq j$, as it is the case of the angular momentum components. Furthermore the spin operator squared commutes with all the spin components

$$[\mathbf{S}^2, S_i] = 0 . \quad (\text{B.3})$$

It is possible to define two operators known as *ladder* operators

$$S_{\pm} = S_x \pm iS_y , \quad (\text{B.4})$$

and they satisfy the following commutation relations

$$[S_z, S_{\pm}] = \pm\hbar S_{\pm} \quad [S_+, S_-] = 2\hbar S_z . \quad (\text{B.5})$$

The operators defined so far act on an Hilbert space of two components (two-dimensional space) that can be fully represented by a basis of eigenstates $|s, m_s\rangle$ labelled with the eigenvalues of the \mathbf{S}^2 and S_z operators respectively: $|1/2, 1/2\rangle \equiv |\uparrow\rangle$, $|1/2, -1/2\rangle \equiv |\downarrow\rangle$. These states are eigenstates of the Pauli matrix σ_z .

B.2 Coupling of two spins

Let's consider two spin $S = 1/2$ that are coupled by an interaction of the form

$$\mathcal{H} = \lambda \mathbf{S}_1 \cdot \mathbf{S}_2 \quad (\text{B.6})$$

where 1,2 are referred to the two particles. It is easy to see that

$$[\mathcal{H}, S_i] \neq 0 \quad (\text{B.7})$$

where $i = 1, 2$.

This problem can however be solved, i.e. it is possible to express the eigenvalues of \mathcal{H} as a function of the ones given by the single spin operators by defining a *total spin momentum* $\mathbf{S}_{tot} = \mathbf{S}_1 + \mathbf{S}_2$. Then

$$\mathbf{S}_{tot}^2 = \mathbf{S}_1^2 + \mathbf{S}_2^2 + 2\mathbf{S}_1 \cdot \mathbf{S}_2 . \quad (\text{B.8})$$

and

$$\mathcal{H} = \frac{\lambda}{2} (\mathbf{S}_{tot}^2 - \mathbf{S}_1^2 - \mathbf{S}_2^2) . \quad (\text{B.9})$$

According to the summation rules for spins, the eigenvalues of \mathbf{S}_{tot}^2 is $s(s+1)$ where

$$s = |s_2 - s_1|, |s_2 - s_1| + 1, \dots, (s_1 + s_2) - 1, (s_1 + s_2) , \quad (\text{B.10})$$

and s_1 and s_2 are the eigenvalues of \mathbf{S}_1 and \mathbf{S}_2 respectively. Therefore for the specific case of two spin 1/2 the total spin momentum eigenvalues s can be 0 or 1 and the Hamiltonian has two energy levels given by

$$\begin{cases} \frac{\lambda}{4} & \text{if } s = 1 \\ -\frac{3\lambda}{4} & \text{if } s = 0 \end{cases} \quad (\text{B.11})$$

As usual each state can have a degeneracy that is given by $(2s + 1)$ and therefore the state with $s = 0$ is a singlet while the state $s = 1$ is a triplet.

Appendix C

Additional results for BNOO

In the following Sections additional results and figures are introduced, but they are not discussed in detail.

C.1 Bondlengths and DOS

When we applied the *Constrained relaxation of Model A*, the c bondlength was kept fixed, while the other Na-O bondlengths were allowed to relax freely to their optimal value. The result, already outlined in the thesis, is that the Na-O octahedra tend to distort with a non uniform compression of the a , b and c bonds along the principal axis. The dependence of the a and b bonds over the c one could be easily analyzed by looking, step by step, at the values obtained when the c bond was changed. The result is plotted in Figure C.1, where also the Computational and the Experimental values of the c bondlength are outlined. Here "Experimental" means the undistorted structure observed via X-Ray analysis [76].

The DOS of BNOO with DFT is plotted in Figure C.2, while the ones obtained with DFT + U and DFT + U + SOC are plotted in Figures C.3 (a) and (b). The value of U_{eff} set is 3.4 eV, the structure is the optimized one and the direction of the magnetic moments is constrained with $\phi = 60^\circ$.

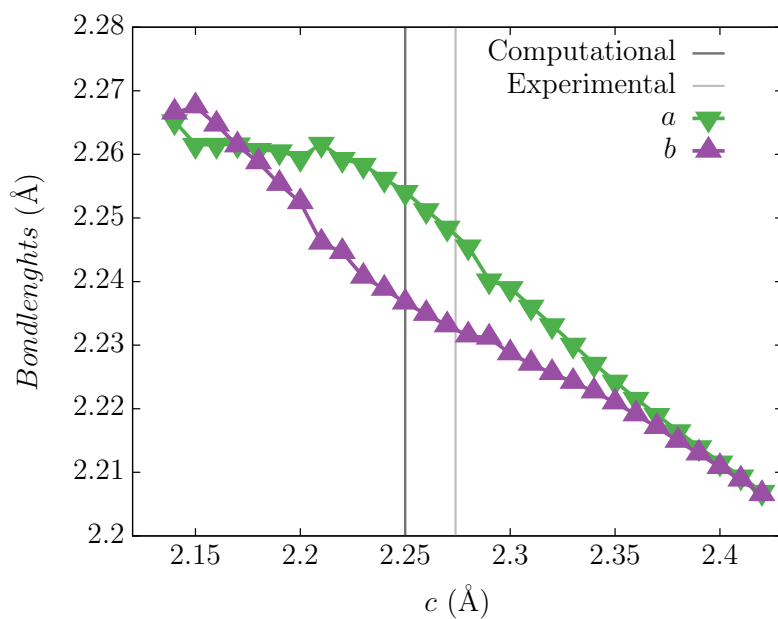


Figure C.1: Bondlength dependence for BNOO

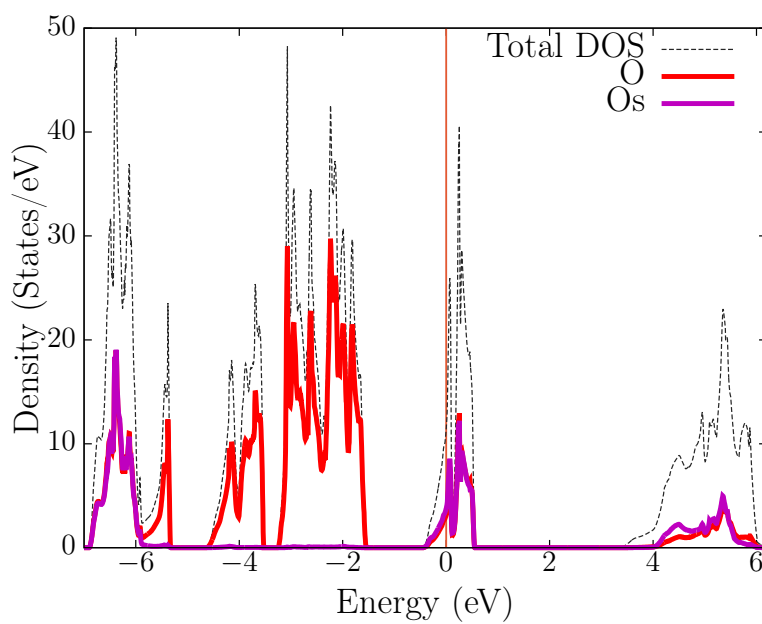
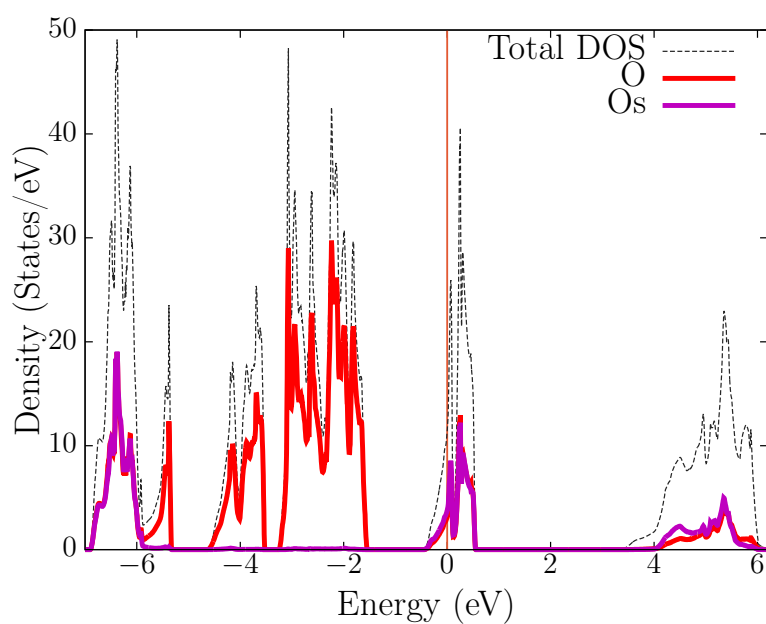
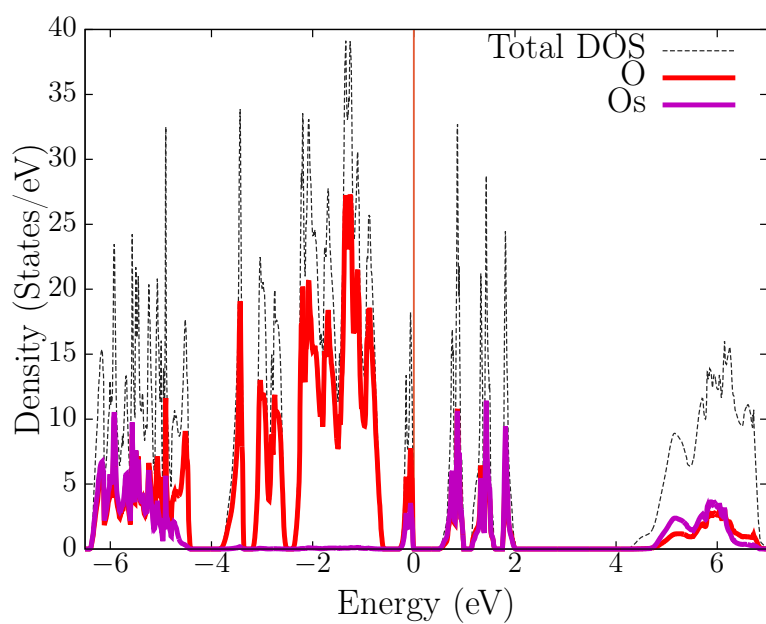


Figure C.2: DOS of BNOO with LDA.



(a)



(b)

Figure C.3: DOS of BNOO with LDA + U and LDA + U + SOC.
(a) LDA + U with optimized structure and $U_{eff} = 3.4$ eV. (b) LDA + U + SOC with optimized structure and $U_{eff} = 3.4$ eV.

C.2 Phase Diagram

Local symmetry and distortions are, as showed, strongly related to the magnetic nature of BNOO as well as the electron correlation. So we decided to further investigate this dependence by deriving a phase diagram that could relate both.

The calculations were set as follows: for every value of U_{eff} (2.8, 3.0, 3.2 and 3.4 eV) we relaxed the local structure via the *Constrained relaxation of model A with LDA + U + SOC* approach. Then we selected the optimal structure and the ones with a slightly compressed and elongated c bondlength ($\pm 0.4\%$). For each structure a complete energy curve with respect to the canting angle was calculated within the DFT + U + SOC scheme. Attention was made in using the same U_{eff} chosen every time for optimizing the local structure.

The result is the Figure below. It shows a set of points that are *empty red diamonds* if the global energy minima is found at $\phi \approx 17.5^\circ$ and no energy minima is observed at $\phi \approx 65^\circ$, *full red diamonds* if the global minima is at $\phi \approx 17.5^\circ$ and also the minima at $\phi \approx 65^\circ$ is found, and *blue squares* if the global minima is at $\phi \approx 65^\circ$.

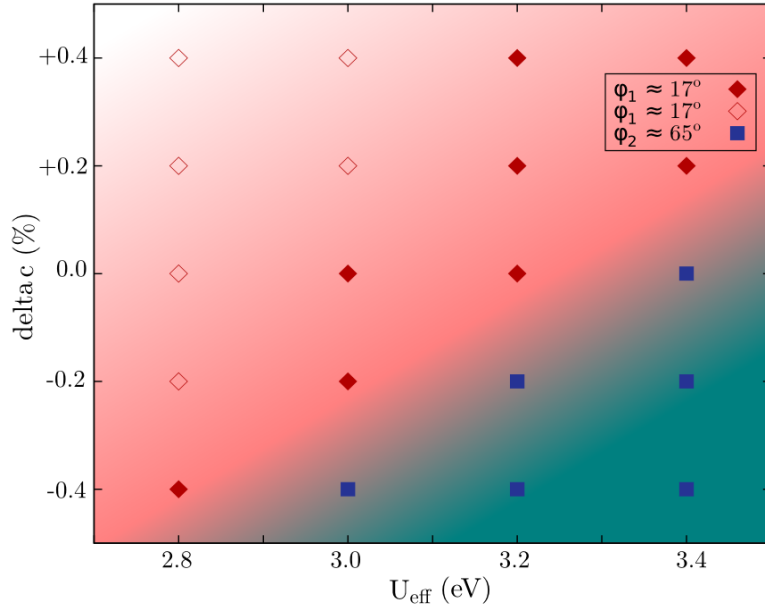


Figure C.4: Phase Diagram of BNOO Phase diagram of local distortion vs U_{eff} for BNOO. The shaded red part of the plot represent the area in which the global minima is $\phi \approx 17.5^\circ$ while the shaded blue one is when the global minima is $\phi \approx 65^\circ$.

Appendix D

Other results for BCOO

The DOS of BCOO with DFT, DFT + U and DFT + U + SOC are plotted below. The value of U_{eff} set is 3.0 eV, the structure is the optimized one and the direction of the magnetic moments is constrained with $\phi = 60^\circ$.

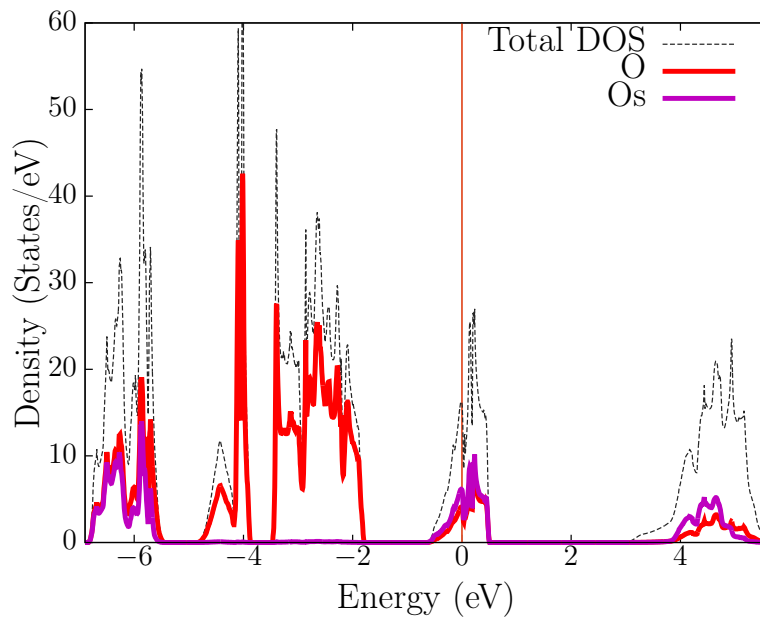
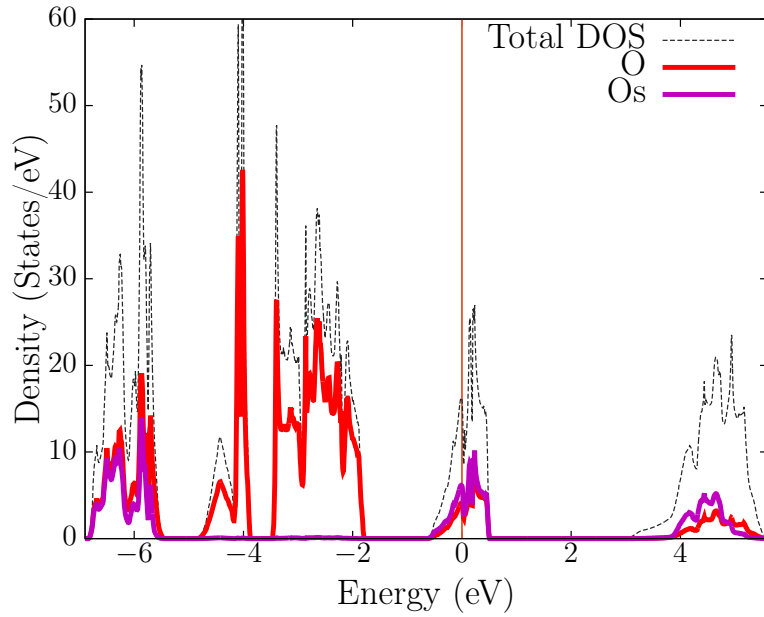
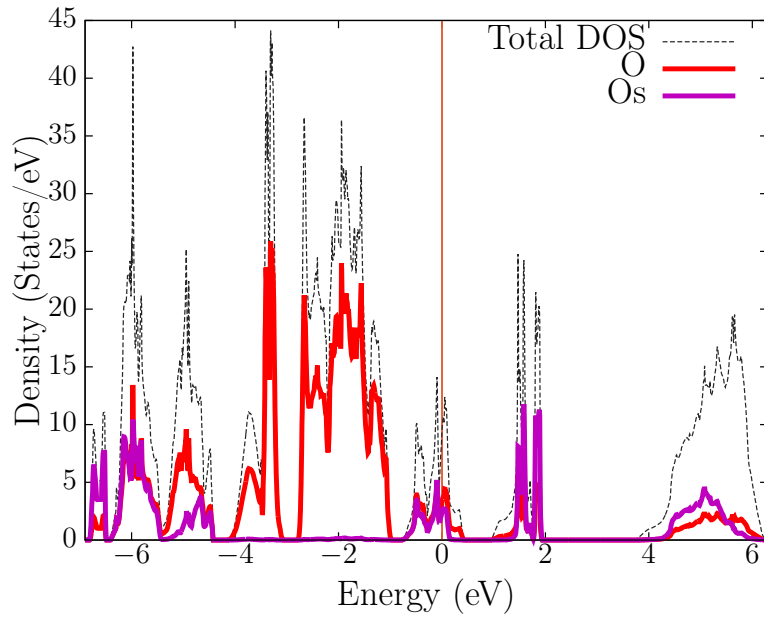


Figure D.1: DOS of BCOO with LDA.



(a)



(b)

Figure D.2: DOS of BCOO with LDA + U and LDA + U + SOC.
 (a) LDA + U with optimized structure and $U_{eff} = 3.0$ eV. (b) LDA + U + SOC with optimized structure and $U_{eff} = 3.0$ eV.

Bibliography

- [1] Milton Abramowitz. *Handbook of Mathematical Functions, With Formulas, Graphs, and Mathematical Tables*. Dover Publications, Inc., New York, NY, USA, 1974.
- [2] Amikam Aharoni. *Introduction to the Theory of Ferromagnetism*. Oxford University Press, 2001.
- [3] B. Amadon. DFT+DMFT versus DFT+U description of Mott insulators: DMFT restores spin and orbital symmetry and removes metastable states. In *APS Meeting Abstracts*, page A35.002, February 2012.
- [4] O. Krogh Andersen. Linear methods in band theory. *Phys. Rev. B*, 12:3060–3083, Oct 1975.
- [5] V. I. Anisimov and A. I. Lichtenstein. *LDA+U Method: Screened Coulomb Interaction in the Mean-field Approximation*, chapter 2, pages 97–101. Anisimov, Gordon and Breach Science Publishers, 2000.
- [6] Vladimir I Anisimov, F Aryasetiawan, and A I Lichtenstein. First-principles calculations of the electronic structure and spectra of strongly correlated systems: the lda + u method. *Journal of Physics: Condensed Matter*, 9(4):767, 1997.
- [7] N.W. Ashcroft and N.D. Mermin. *Solid State Physics*. Saunders College, Philadelphia, 1976.
- [8] Kim B., Khmelevskiy S., Mazin I. I., Agterberg D.F., and Franchini C. Anisotropy of magnetic interactions and symmetry of the order parameter in unconventional superconductor Sr_2RuO_4 . *npj Quantum Materials*, 2:37, 2017.
- [9] Sayantika Bhowal and I. Dasgupta. Covalency and spin-orbit coupling driven magnetism in the double-perovskite iridates Sr_2MIR_6 ($M = \text{Ca}, \text{Mg}$). *Phys. Rev. B*, 97:024406, Jan 2018.
- [10] James Bjorken and Sidney David Drell. *Relativistic Quantum Mechanics*. Mc Graw-Hill, 1964.

-
- [11] P. E. Blöchl. Projector augmented-wave method. *Phys. Rev. B*, 50:17953–17979, Dec 1994.
- [12] Stephen Blundell. *Magnetism in Condensed Matter*. Oxford University Press, 2001.
- [13] Georgi Bodurov, Tatyana Ivanova, and Kostadinka Gesheva. Technology and application of transition metal oxide of w-v-o as functional layers and nio thin films as counter electrode material in electrochromic smart windows. *Physics Procedia*, 46:149 – 158, 2013. EUROCVTD 19Nineteenth European Conference on Chemical Vapor Deposition.
- [14] M. Born and Oppenheimer R. Zur quantentheorie der molekeln. *Annalen der Physik*, 389(20):457–484, 1927.
- [15] Mark Buchanan. Mind the pseudogap. *Nature*, 409, Jan 2001.
- [16] G. Cao, T. F. Qi, L. Li, J. Terzic, S. J. Yuan, L. E. DeLong, G. Murthy, and R. K. Kaul. Novel magnetism of $\text{Ir}^{5+}(5d^4)$ ions in the double perovskite Sr_2YIrO_6 . *Phys. Rev. Lett.*, 112:056402, Feb 2014.
- [17] Klaus Capelle. A bird’s eye view of density functional theory.
- [18] D. M. Ceperley and B. J. Alder. Ground state of the electron gas by a stochastic method. *Phys. Rev. Lett.*, 45:566–569, Aug 1980.
- [19] Gang Chen and Leon Balents. Spin-orbit coupling in d^2 ordered double perovskites. *Phys. Rev. B*, 84:094420(13), Sep 2011.
- [20] Gang Chen, Rodrigo Pereira, and Leon Balents. Exotic phases induced by strong spin-orbit coupling in ordered double perovskites. *Phys. Rev. B*, 82:174440(25), Nov 2010.
- [21] B. Dui Claude Cohen-Tannoudji and Franck Laloe. *Quantum Mechanics, Vol. 1*. Vch Pub, 1977.
- [22] R. M. Dreizler and E.K.U. Gross. *Density Functional Theory*. Springer, 1990.
- [23] I. Dzyaloshinsky. A thermodynamic theory of weak ferromagnetism of antiferromagnetics. *Journal of Physics and Chemistry of Solids*, 4(4):241 – 255, 1958.
- [24] J. van den Brink E. Pavarini, E. Koch and G. Sawatzky. *Quantum Materials: Experiments and Theory*, volume 6, chapter Modeling and Simulation. Forschungszentrum Julic, 2016.
- [25] T. Engel and P. Reid. *Physical Chemistry*. Pearson Benjamin-Cummings, 2013.

-
- [26] A. S. Erickson, S. Misra, G. J. Miller, R. R. Gupta, Z. Schlesinger, W. A. Harrison, J. M. Kim, and I. R. Fisher. Ferromagnetism in the Mott Insulator Ba_2NaOsO_6 . *Phys. Rev. Lett.*, 99:016404(4), Jul 2007.
- [27] H. Eschrig. *The Fundamentals of Density Functional Theory*. Teubner Leipzig, 1996.
- [28] Dionys Baeriswyl et al. *The Hubbard Model: Its Physics and Mathematical Physics*. NATO ASI series, Series B, Physics v. 343, 1995.
- [29] Shruba Gangopadhyay and Warren E. Pickett. Interplay between spin-orbit coupling and strong correlation effects: Comparison of the three osmate double perovskites Ba_2AOsO_6 ($A = Na, Ca, Y$). *Phys. Rev. B*, 93:115126(10), Apr 2016.
- [30] T. L. Gilbert. Hohenberg-Kohn theorem for nonlocal external potentials. *Phys. Rev. B*, 12:2111, 1975.
- [31] John B. Goodenough. Theory of the role of covalence in the perovskite-type manganites $[La, m(II)]MnO_3$. *Phys. Rev.*, 100:564–573, Oct 1955.
- [32] John B. Goodenough. An interpretation of the magnetic properties of the perovskite-type mixed crystals $La_1-xSr_xCoO_3$. *Journal of Physics and Chemistry of Solids*, 6(2):287 – 297, 1958.
- [33] J. E. Greedan, D. B. Willson, and T. E. Haas. Metallic nature of osmium dioxide. *Inorganic Chemistry*, 7(11):2461–2463, 1968.
- [34] O. Gritsenko and E.J. Baerends. The spin-unrestricted molecular KohnSham solution and the analogue of Koopmans theorem for open-shell molecules. *J. Chem. Phys.*, 120:8364, 2004.
- [35] D. R. Hamann. Optimized norm-conserving vanderbilt pseudopotentials. *Phys. Rev. B*, 88:085117, Aug 2013.
- [36] Judith Harl and Georg Kresse. Cohesive energy curves for noble gas solids calculated by adiabatic connection fluctuation-dissipation theory. *Phys. Rev. B*, 77:045136, Jan 2008.
- [37] Judith Harl, Laurids Schimka, and Georg Kresse. Assessing the quality of the random phase approximation for lattice constants and atomization energies of solids. *Phys. Rev. B*, 81:115126, Mar 2010.
- [38] John E. Harriman. Orthonormal orbitals for the representation of an arbitrary density. *Phys. Rev. A*, 24:680, 1981.

-
- [39] D. R. Hartree. The wave mechanics of an atom with a non-coulomb central field. part iii. term values and intensities in series in optical spectra. *Mathematical Proceedings of the Cambridge Philosophical Society*, 24(3):426437, 1928.
- [40] H. Hellmann. A new approximation method in the problem of many electrons. *The Journal of Chemical Physics*, 3(1):61–61, 1935.
- [41] Christopher L. Henley. *Spin Hamiltonian and Exchange Interactions*, pages 1 – 13. Laboratory of Atomic and Solid State Physics, Cornell University, Ithaca, NY, 2007.
- [42] Victor E. Henrich and P.A. Cox. *The surface science of metal oxides*. Cambridge University Press, 1994.
- [43] Naoya Iwahara and Liviu F. Chibotaru. Exchange interaction between j multiplets. *Phys. Rev. B*, 91:174438, May 2015.
- [44] H. A. Jahn and E. Teller. Stability of Polyatomic Molecules in Degenerate Electronic States. I. Orbital Degeneracy. *Proceedings of the Royal Society of London Series A*, 161:220–235, July 1937.
- [45] Junjiro Kanamori. Superexchange interaction and symmetry properties of electron orbitals. *Journal of Physics and Chemistry of Solids*, 10(2):87 – 98, 1959.
- [46] Brendan J. Kennedy, Maxim Avdeev, Hai L. Feng, and Kazunari Yamaura. Phase transitions in strontium perovskites. studies of SrOsO₃ compared to other 4d and 5d perovskites. *Journal of Solid State Chemistry*, 237:27 – 31, 2016.
- [47] B. J. Kim, Hosub Jin, S. J. Moon, J.-Y. Kim, B.-G. Park, C. S. Leem, Jaejun Yu, T. W. Noh, C. Kim, S.-J. Oh, J.-H. Park, V. Durairaj, G. Cao, and E. Rotenberg. Novel $J_{\text{eff}} = 1/2$ mott state induced by relativistic spin-orbit coupling in sr₂iro₄. *Phys. Rev. Lett.*, 101:076402, Aug 2008.
- [48] Erich Koch. Lecture notes of the autumn school correlated electrons. In *Exchange Mechanisms*. German Research School for Simulation Science GmbH, 2012.
- [49] D D Koelling and G O Arbman. Use of energy derivative of the radial solution in an augmented plane wave method: application to copper. *Journal of Physics F: Metal Physics*, 5(11):2041, 1975.
- [50] H.A Kramers. L’interaction entre les atomes magntognes dans un cristal paramagnétique. *Physica*, 1(1):182 – 192, 1934.
- [51] G Kresse and J Hafner. Norm-conserving and ultrasoft pseudopotentials for first-row and transition elements. *Journal of Physics: Condensed Matter*, 6(40):8245, 1994.

-
- [52] G. Kresse and D. Joubert. From ultrasoft pseudopotentials to the projector augmented-wave method. *Phys. Rev. B*, 59:1758–1775, Jan 1999.
- [53] M. Levy. Universal variational functionals of electron densities, first order density matrices, and natural spin orbitals and solution of the v-representability problem. *Proc. Natl. Acad. Sci USA*, 76:6062, 1979.
- [54] Yonghui Li and C. A. Ullrich. Time-dependent v-representability on lattice systems. *The Journal of Chemical Physics*, 129(4):044105, 2008.
- [55] Peitao Liu, Sergii Khmelevskiy, Bongjae Kim, Martijn Marsman, Dianzhong Li, Xing-Qiu Chen, D. D. Sarma, Georg Kresse, and Cesare Franchini. Anisotropic magnetic couplings and structure-driven canted to collinear transitions in Sr_2IrO_4 by magnetically constrained noncollinear dft. *Phys. Rev. B*, 92:054428, Aug 2015.
- [56] W. Liu, R. Cong, A.P. Reyes, I. R. Fisher, and V.F. Mitrovic. Nature of lattice distortions in cubic double perovskite $\text{Ba}_2\text{NaOsO}_6$. *Phys. Rev. B*, 97:224103(14), June 2018.
- [57] L. Lu, M. Song, W. Liu, A.P. Reyes, P. Kuhns, H.O. Lee, I.R. Fisher, and V.F. Mitrovic. Magnetism and local symmetry breaking in a Mott insulator with strong spin orbit interactions. *Nature Communications*, 8:14407, Feb 2017.
- [58] O. Nganba Meetei, William S. Cole, Mohit Randeria, and Nandini Trivedi. Novel magnetic state in d^4 mott insulators. *Phys. Rev. B*, 91:054412, Feb 2015.
- [59] Xing Ming, Xiangang Wan, Carmine Autieri, Jianfeng Wen, and Xiaojun Zheng. Spin-orbit coupling driven insulating state in hexagonal iridates Sr_3mIrO_6 ($m = \text{Sr, Na, Li}$). *Phys. Rev. B*, 98:245123, Dec 2018.
- [60] Hendrik J. Monkhorst and James D. Pack. Special points for brillouin-zone integrations. *Phys. Rev. B*, 13:5188–5192, Jun 1976.
- [61] Tôru Moriya. Anisotropic superexchange interaction and weak ferromagnetism. *Phys. Rev.*, 120:91–98, Oct 1960.
- [62] Eva Pavarini, Erich Koch, and Ulrich Schollwock. Lecture notes of the autumn school correlated electrons. In *Emergent Phenomena in Correlated Matter*. German Research School for Simulation Science GmbH, 2013.
- [63] John P. Perdew and Mel Levy. Extrema of the density functional for the energy: Excited states from the ground-state theory. *Phys. Rev. B*, 31:6264–6272, May 1985.

-
- [64] Shu-Ting Pi, Ravindra Nanguneri, and Sergey Savrasov. Anisotropic multipolar exchange interactions in systems with strong spin-orbit coupling. *Phys. Rev. B*, 90:045148(9), Jul 2014.
- [65] B. Ramachandra, Jung Sik Choi, Keun-Soo Kim, Ko-Yeon Choo, Jae-Suk Sung, and Tae-Hwan Kim. Movw-mixed oxide as a partial oxidation catalyst for methanol to formaldehyde. In Hyun-Ku Rhee, In-Sik Nam, and Jong Moon Park, editors, *New Developments and Application in Chemical Reaction Engineering*, volume 159 of *Studies in Surface Science and Catalysis*, pages 273 – 276. Elsevier, 2006.
- [66] Michele Reticcioli, Martin Setvin, Michael Schmid, Ulrike Diebold, and Cesare Franchini. Formation and dynamics of small polarons on the rutile TiO₂(110) surface. *Phys. Rev. B*, 98:045306, Jul 2018.
- [67] R.G.Parr and W. Yang. *Density Functional Theory of Atoms and Molecules*. Oxford University Press, 1989.
- [68] Paolo Santini, Stefano Carretta, Giuseppe Amoretti, Roberto Caciuffo, Nicola Magnani, and Gerard H. Lander. Multipolar interactions in *f*-electron systems: The paradigm of actinide dioxides. *Rev. Mod. Phys.*, 81:807–863, Jun 2009.
- [69] Franz Schwabl. *Second Quantization*, pages 3–32. Springer Berlin Heidelberg, Berlin, Heidelberg, 2008.
- [70] Z. Z. Sheng and A. M. Hermann. Bulk superconductivity at 120 k in the TlCa/BaCuO system. *Nature*, 332, Oct 1988.
- [71] Youguo Shi, Yanfeng Guo, Yuichi Shirako, Wei Yi, Xia Wang, Alexei A. Belik, Yoshitaka Matsushita, Hai Luke Feng, Yoshihiro Tsujimoto, Masao Arai, Nanlin Wang, Masaki Akaogi, and Kazunari Yamaura. High-pressure synthesis of 5d cubic perovskite BaOsO₃ at 17 gpa: Ferromagnetic evolution over 3d to 5d series. *Journal of the American Chemical Society*, 135(44):16507–16516, 2013. PMID: 24090137.
- [72] C. M. Srivastava. Theory of colossal magnetoresistance. *Journal of Physics, Condensed Matter*, 11, 1989.
- [73] Georgios L. Stamokostas and Gregory A. Fiete. Mixing of $t_{2g} - e_g$ orbitals in 4d and 5d transition metal oxides. *Phys. Rev. B*, 97:085150, Feb 2018.
- [74] Andrew J. Steele, Peter J. Baker, Tom Lancaster, Francis L. Pratt, Isabel Franke, Saman Ghannadzadeh, Paul A. Goddard, William Hayes, D. Prabhakaran, and Stephen J. Blundell. Low-moment magnetism in the double perovskites Ba₂MOsO₆ ($m = \text{Li, Na}$). *Phys. Rev. B*, 84:144416, Oct 2011.

-
- [75] Katharine E. Stitzer, Ahmed El Abed, Mark D. Smith, Matthew J. Davis, Seung-Joo Kim, Jacques Darriet, and Hans-Conrad zur Loye. Crystal growth of novel osmium-containing triple perovskites. *Inorganic Chemistry*, 42(4):947–949, 2003. PMID: 12588124.
- [76] Katharine E. Stitzer, Mark D. Smith, and Hans-Conrad zur Loye. Crystal growth of Ba_2MOsO_6 ($M = Li, Na$) from reactive hydroxide fluxes. *Solid State Sciences*, 4:311–316, 2002.
- [77] Levente Szasz. *Pseudopotential Theory of Atoms and Molecules. I. A New Method for the Calculation of Correlated Pair Functions*. *J. Chem. Phys.* 49, 679, 1968.
- [78] A. K. Theophilou. The energy density functional formalism for excited states. *J. Phys C*, 12:5419, 1979.
- [79] C.M. Thompson, J.P. Carlo, R. Flacau, T. Aharen, I.A. Leahy, J.R. Pollicemi, T.J.S. Munsie, T. Medina, G.M. Luke, J. Munevar, S. Cheung, T. Goko, Y. J. Uemura, and J. E. Greedan. Long-range magnetic order in the $5d^2$ double perovskite Ba_2CaOsO_6 : comparison with spin-disordered Ba_2YReO_6 . *Journal of Physics: Condensed Matter*, 26, Jul 2014.
- [80] C. A. Ullrich and W. Kohn. Degeneracy in density functional theory: Topology in the v and n spaces. *Phys. Rev. Lett.*, 89:156401, Sep 2002.
- [81] Frank Ghhmann Vladimir Korepin, Fabian H. L. Essler, Holger Frahm, and A. Klumper. *The One-Dimensional Hubbard Model*. Fabian H. L. Essler, 2005.
- [82] Robert M. White. *Quantum Theory of Magnetism. Springer Series in Solid-State Sciences, S*, volume 32, chapter The Magnetic Hamiltonian, pages 33 – 77. Springer, Berlin ,Heidelberg, 1983.
- [83] H.J. Xiang and M.-H. Whangbo. Cooperative effect of electron correlation and spin-orbit coupling on the electronic and magnetic properties of Ba_2NaOsO_6 . *Phys. Rev. B*, 75:052407(4), Feb 2007.
- [84] Kazuhiro Yamamura, Makoto Wakeshima, and Yukio Hinatsu. Structural phase transition and magnetic properties of double perovskites Ba_2CaMO_6 ($M = W, Re, Os$). *Journal of solid state chemistry*, 179:605–612, Jan 2005.
- [85] T Yanagisawa. Physics of the hubbard model and high temperature superconductivity. *Journal of Physics: Conference Series*, 108(1):012010, 2008.